The University of Nottingham

ON THE DETECTION OF DYNAMICALLY SCREENED SCALAR FIELDS USING ATOM INTERFEROMETRY

JAMES A. STEVENSON

Thesis submitted to the University of Nottingham for the degree of Doctor of Philosophy

August 2017

ABSTRACT: Dynamically screened scalar field theories form an attractive collection of models that were introduced to drive the late-time expansion of our universe. A common consequence of these theories is a screening mechanism which leads to the suppression of the fifth-forces mediated by the scalar field in sufficiently dense environments. This enables the models within this class of theories to avoid conflict with the stringent results from local tests of gravity, without the need for any fine tuning. The prototypical example of a dynamically screened scalar field is the chameleon model, for which screening arises due to the mass of the scalar responding to the local density. It has been recently demonstrated that atom interferometry is a powerful technique for constraining such scalars, with near future experiments capable of probing a large portion of the model parameter space. The nature of screening however means that closing in on what remains of the chameleon parameter space is going to become increasingly more difficult. This work aims to address this issue by examining the intricacies of how the chameleon field responds to the configuration of an atom interferometry experiment, where it is found that the non-linearities governing the theory can ultimately be harnessed in order to improve the prospects of detection.

Contents

Chapter 1

Introduction

Almost two decades ago, observations of type Ia supernovae [1][2] uncovered perhaps one of the must puzzling features of our universe, the accelerating cosmic expansion. The implications of this were quite clear: there was something missing from the existing theory of gravity, something pervading space on cosmic scales and capable of driving the repulsion of our universe. This missing ingredient became to be known as Dark Energy. In fact, the markers for this unknown contribution to the energy density of the universe had actually began to appear some years before, through growing tension between the predictions of inflationary cosmology and a series of cosmological observations. The first of these arrived in the 1990s with the influx of new large scale galaxy clustering clustering data [3, 4]. It was found that fitting this data to the spectrum of density perturbations of the spatially flat universe predicted by inflation required the inclusion of a new dark energy component to compensate for the relatively low observed energy density of matter. Shortly to follow, entered the discovery of the temperature anisotropies within the cosmic microwave background [5] which brought substance to this implication by providing the first observational evidence in support of a spatially flat universe. The notion of a dark energy component then continued to gain traction in the build-up to the breakthrough observation of cosmic acceleration, playing a key part in resolving conflict between the measured expansion age of the universe and that predicted by the accepted model at the time: a matter-only universe of vanishing spatial curvature [6, 7]. Since its revolutionary discovery, the studies that provided the the first indications of cosmic acceleration have continued to support the claim as they have advanced into newer generations of technology. As a result, recent probes of large scale structure [8, 9] and the cosmic microwave background [10–13] are recognised as powerful techniques for constraining the accelerating universe in a way that is complementary to supernovae data.

Incorporating the cosmological effect of dark energy into the framework of General Relativity is remarkably simple, resting only on the inclusion of a small cosmological constant term Λ. This led to a new paradigm, the standard cosmological model known as Λ-CDM, which pictures a universe containing a cosmological constant as its dark energy together with the gravitating yet evasive cold dark matter. The elegance of the Λ-CDM model comes in part from its ability to harmonise with all known observational data using only a small number of free parameters [14]. However, despite surviving every observational test within an era of precision cosmology, Λ-CDM (otherwise known as the Concordance model) is not

without its problems. In fact, the cosmological constant itself has a history that pre-dates any thoughts of accelerating expansion. It made its first appearance just two years after the arrival of General Relativity, where Einstein introduced his first cosmological model of a static universe [16]. Although this was subsequently revoked following Hubble's discovery of an expanding universe [17], it was noted by Zel'dovich [18] some decades later that a cosmological constant term should be identified as the vacuum energy free space, something not to be overlooked. Unfortunately any attempts to reconcile the measured value of the cosmological constant with the calculated energy density of the quantum vacuum fail spectacularly, with the two in conflict by at least sixty orders of magnitude. This disagreement came to be what is known today as the cosmological constant problem. As a result, any support gained by embracing the cosmological constant as a vacuum energy density quickly evaporated, leaving the puzzle of its true physical nature as a problem unsolved.

At the present time, the standard cosmological model divides the energy budget of the universe into approximately seventy percent dark energy and thirty percent matter, with an almost negligible radiation contribution of one part in a thousand [19]. Due to the very different scaling behaviours of their respective energy densities throughout the evolution of the universe, having both matter and dark energy present at the same order of magnitude indicates a special point in cosmic time. In fact, it would require highly tuned initial conditions which, in this case, ensured that the accelerated expansion triggered late enough in the history of the universe to allow for the formation of stars [20]. This presented a second issue for the theory built invoking a cosmological constant, the "Cosmological Coincidence Problem".

In being accompanied by two incredibly alarming flaws, the cosmological constant represents one of the most severe fine tuning problems in physics. Failing to arrive at a satisfactory solution over the years has placed emphasis on an alternative way of thinking, which is that General Relativity in its canonical form falls inadequate at cosmological scales and instead a more complete theory of gravity is required. In the years to follow there was a huge surge of interest in the field of dark energy and modified gravity, with a host of new theories aiming to explain the cosmic expansion through the introduction of new dynamical degrees of freedom, see Reference [21] for a review. One of the most popular candidates is to attribute expansion to the presence of a scalar field lying within its equilibrium configuration. Generically, additional scalar degrees of freedom have been found to emerge from string theory and brane world scenarios [21, 22]. Thus, these theories, known as scalar-tensor theories, have the potential to link two seemingly detached scales by relieving the tension on GR in both the infrared and ultraviolet regimes simultaneously. Of course, from a high energy perspective, searches for a quantum theory of gravity has been long under-way and thus departures also entering at large distances opens up the possibility of exciting phenomenology bridging between the two scales [23].

However, the introduction of an extra field coupled to matter entails the existence of a fifth force which could threaten the compatibility with local tests. The option is therefore to either design a theory which is inherently weaker than gravity, or to allow for the presence of some screening mechanism, suppressing the force in our local vicinity thus allowing for

the model to successfully evade terrestrial constraints. Tuning the force to be weaker than gravity would require setting the theory at above the Planck scale making it impossible to be described as a quantum field theory, therefore offering no real resolution to the problem. On the other hand, a number of attractive scalar theories admitting screening behaviour have been constructed to date. Amongst the more common of these are the Chameleon, Dilaton and the Symmetron Models where non-linearities in the interaction potential feed into an environmental dependence of the field solutions. Accordingly, the forces are suppressed in regions of higher density making them, in principle, compatible with stringent terrestrial constraints. A benefit of these theories is that they offer testable predictions at fairly accessible length scales. The environmental suppression unlocks the possibility to test any departures from General Relativity in the lab vacuum, where densities can be made sufficiently low to circumvent the screening process. In a regime where screening is absent, the force sourced by an additional scalar degree of freedom could in principle significantly exceed the gravitational interaction with little consequence at larger length scales. The trademark non-linearities of these theories suggest that fifth-force interactions could begin to resurface within the regime of lab based vacuum experiments.

Indeed, means to probe scalar extensions of gravity in the lab have received considerable focus in recent years. Perhaps due to its relative simplicity, the chameleon model has received the most attention, with a wealth of experiments being formulated or appropriated to its detection. In attempting to explore what remains of the parameter space, the challenge is going to become increasingly more difficult as the exact screening behaviour that allows for the evasion of terrestrial constraints begins to resurface at these scales. Thus, remarkable levels of precision are going to be required to fully map out the model parameter space. To date, the most powerful experimental technique has been atom interferometry [28] which exploits the quantum mechanical properties of matter to directly probe the chameleon force exerted by a source object within a vacuum chamber. Analysis of the chameleon field around a spherical source demonstrates some interesting phenomenology when moving into the screened regime: the development of a special internal field structure which acts to mask any fifth-force contributions arising from the matter deep within the object. As a result, only a thin-shell near the surface of source contributes to the external forth. This is the primary mechanism behind chameleon screening and became to be known as the thin-shell effect. An awareness of the mechanism behind screening raised two important questions: Firstly, how does this internal field structure respond to the geometry of the source? Secondly, can any shape dependence be harnessed such as to enhance the chameleon force? If so, it may be possible to exploit any shape dependence arising to further tighten the bounds placed on the model parameter space.

The scope of this thesis is to examine whether alternatives to a spherical source object could be used to heighten the detectability of a fifth force arising from a dynamically screened scalar field. Although the question has been left quite general, analysis will be restricted exclusively to the chameleon model. However, previous work has shown that the three candidate models: the Dilaton, the Symmetron, and the Chameleon, all exhibit similar phenomenologies for a spherical source. Therefore, the idea is that any deductions made for the chameleon model will, at least at a qualitative level, extend to the other two models.

The subject will be approached by first outlining the key theoretical developments taking one from a gravitational theory built to include a cosmological constant, to a dynamically screened scalar field theory of dark energy. Arriving at the chameleon model, the relevant groundwork will then be laid out to study the theory within the context of atom interferometry. This will conclude the introductory chapter. The subsequent chapters will then be devoted to presenting original research. Chapter 2 will focus on analysis of the chameleon field profile around an ellipsoidal source. Chapter 3 extends on these results through the implementation of a numerical finite element scheme, in order to constrain the chameleon theory using more general sources. Chapter 4 then presents a novel parallel plate configuration to be used within an atom interferometry set-up.

1.1 Conventions

Unless noted otherwise, the material presented in this thesis will adopt a natural unit convention obtained by setting $\hbar = c = 1$. As a result, all dimensionful quantities will be denominated in either GeV or GeV^{-1}, describing energy and length scales respectively. M_{PL} will be used to denote the reduced Planck mass $M_{\text{PL}} = 1/\sqrt{8\pi G}$, where G is Newton's constant of gravitation. The space-time metric $g_{\mu\nu}$ will be assigned the negative signature $(-,+,+,+)$.

1.2 An Accelerating Universe

Prior to the discovery of the accelerated expansion of the universe, the future of the cosmos seemed relatively easy to picture. Out of the four fundamental forces of nature, gravity is the dominant interaction at long distance scales. As a universally attractive force, our intuition would tell us that the expansion a universe filled by matter and radiation interacting via gravity would inevitably slow down over time. The theory of General Relativity in its standard form agrees with this statement: either the universe would initially come to collapse under its own gravitational attraction, or the rate of expansion would be sufficiently high to make the universe gravitationally unbound, allowing expansion to continue indefinitely but gradually slowing down. A state of accelerated expansion can be achieved by slightly modifying the Einstein-Hilbert action to contain an additional free parameter Λ such that

$$S = \frac{M_{\text{PL}}}{2} \int \mathrm{d}^4x \, \sqrt{-g} \, \left(R - 2\Lambda\right) + S_m \left(g_{\mu\nu}, \psi\right) \, , \tag{1.1}$$

where $g_{\mu\nu}$ is the space-time metric, g is its determinant, R is the Ricci scalar, and Λ is identified as the cosmological constant. The term $S_m \left(g_{\mu\nu}, \psi\right)$ corresponds to the action of the matter sector, with ψ collectively describing the matter fields. The equations of motion for this system are found following the usual prescription, by solving the Euler-Lagrange equation for the single dynamical degree of freedom, the metric $g_{\mu\nu}$ to give

$$R_{\mu\nu} - \frac{1}{2} g_{\mu\nu} R + \Lambda g_{\mu\nu} = 8\pi G T_{\mu\nu} \, , \tag{1.2}$$

with $T_{\mu\nu}$ corresponding to the stress-energy tensor. The Einstein equations above (Equation (1.2)) describe the intricate link between geometry of space-time (collected on the left-hand side) and the distribution of matter (on the right-hand side). In modelling the matter sources within the universe to form a perfect fluid with energy density ρ and pressure p, the stress-energy tensor is given by

$$T_{\mu\nu} = (\rho + p)\, U_\mu U_\nu + p g_{\mu\nu} \ , \tag{1.3}$$

where U_μ is the four-velocity of the fluid. In accordance with the Cosmological Principle, the expanding universe is assumed to be homogeneous and isotropic which calls for a metric of the Friedmann-Robertson-Walker (FLRW) form:

$$\mathrm{d}s^2 = -\mathrm{d}t^2 + a^2(t) \left[\frac{\mathrm{d}r^2}{1 - kr^2} + r^2 \mathrm{d}\theta^2 + r^2 \sin^2(\theta)\, \mathrm{d}\phi^2 \right] \ , \tag{1.4}$$

where $a(t)$ is the scale factor describing an expanding universe and the curvature parameter k takes the values of $0, +1, -1$ for spatially flat, positively curved and negatively curved geometries respectively. Observations to date [12, 13] are consistent with the universe being spatially flat, so hereinafter the curvature parameter will be taken to be zero. Incorporating the FLRW metric (Equation (1.4)) into the field equations of Equation (1.2) then leads to the Friedmann equations for a spatially flat universe:

$$\left(\frac{\dot{a}}{a} \right)^2 = \frac{8\pi G}{3} \rho + \frac{\Lambda}{3} \ , \tag{1.5a}$$

$$\frac{\ddot{a}}{a} = -\frac{4\pi G}{3} (\rho + 3p) + \frac{\Lambda}{3} \ , \tag{1.5b}$$

where $\dot{a}(t)$ and $\ddot{a}(t)$ represent the first and second order time derivatives of the scale factor respectively. It is useful to then definite an energy density for the cosmological constant through the relation $\rho_\Lambda = 8\pi G \Lambda / 3$. The combined matter and radiation components have an equation of state parameter defined by $\rho = wp$ subject to the bound $0 \leq w \leq 1/3$ [29], dependent on the the relative contributions from each. This follows from the fact that non-relativistic matter has an equation of state parameter $w_m = 0$, setting the lower bound, whereas radiation satisfies an equation of state such that $w_r = 1/3$, which provides the upper bound. Working now with the vacuum energy density ρ_Λ and utilising the equation of state for ρ, the above Equations (1.5a) and (1.5b) can be re-expressed as

$$\left(\frac{\dot{a}}{a} \right)^2 = \frac{8\pi G}{3} (\rho + \rho_\Lambda) \ , \tag{1.6a}$$

$$\frac{\ddot{a}}{a} = -\frac{4\pi G}{3} \{ \rho(1 + 3w) - 2\rho_\Lambda \} \ . \tag{1.6b}$$

Thus, it can be seen from Equation (1.6b) that it is impossible to source an acceleration for a universe a comprised of cold dark-matter and radiation alone ($w \geq 0$), requiring a

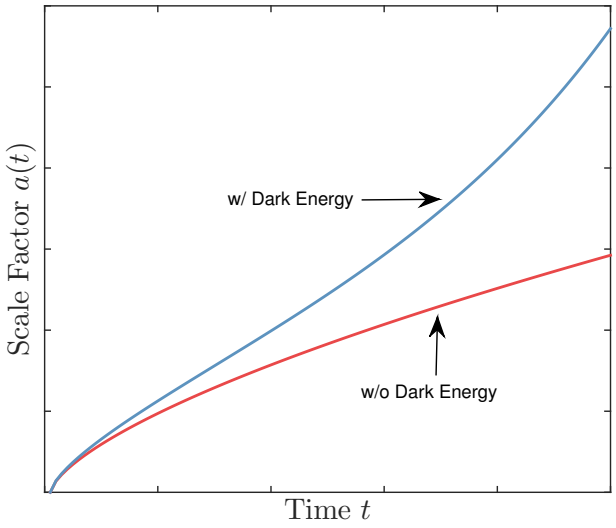

Figure 1.1: Figure displaying the evolution of the scale factor for universes with and without dark energy. In the model without dark energy, the scale factor evolves according to a matter dominated universe with $a(t) \sim t^{2/3}$ whereas the line inclusive of a cosmological constant includes a de-Sitter contribution of the form $a(t) \sim e^{Ht}$, with H as the Hubble parameter given by $\dot{a}(t)/a(t)$.

sufficiently large energy contribution from the cosmological constant ρ_Λ to make the acceleration term $\ddot{a}(t)$ greater than zero. Furthermore, by drawing comparisons between the two density contributions of Equation (1.6b), it also follows that the cosmological constant can be modelled as a fluid with an effective equation of state parameter $w_\Lambda = -1$.

1.2.1 The Cosmological Constant Problem

The cosmological constant problem arises when trying to match the observational inferences of this model to the values predicted by quantum field theory. One can break down the various contributions towards an effective cosmological constant into three. The first of these, can be considered as the bare cosmological constant term, to be included when constructing a general covariant theory of gravity. The second and third of these contributions relate to vacuum energies sourced within the matter sector, this can be due to the potential energy of a scalar field arising after a symmetry breaking phase, or due to the zero-point energies (associated with vacuum fluctuations) of a free field. A basic argument can be made [30] that for the standard model of particle physics, the primary source of the vacuum energy of space comes from the zero-point energy of a free field. This vacuum energy contribution can be represented by a collection of harmonic oscillators in momentum space, whose energies extend up to the cut-off energy of the theory, that is, the energy scale up to which the theory can be trusted. If the ultra-violet cut-off point of a theory is denoted E_{max}, then it follows

that the vacuum energy density $\rho_\Lambda^{(\mathrm{V})}$ goes as

$$\rho_\Lambda^{(\mathrm{V})} \sim E_{\mathrm{max}}^4 \,, \tag{1.7}$$

such that the vacuum energy density grows with cut-off energy to the fourth power. Therefore, the belief that quantum field theory can be trusted all the way up to the Planck scale implies a vacuum energy of the order

$$\rho_\Lambda^{(\mathrm{V})} \sim (10^{18}\,\mathrm{GeV})^4 \,. \tag{1.8}$$

Collectively then, the effective cosmological constant energy density will look like

$$\rho_\Lambda = \rho_\Lambda^{(0)} + \rho_\Lambda^{(\mathrm{V})} \,, \tag{1.9}$$

with $\rho_\Lambda^{(0)}$ signifying the energy density contribution from the bare cosmological constant term. Comparing the observed value of $\rho_\Lambda^{(\mathrm{obs})} \sim (10^{-12}\,\mathrm{GeV})^4$ to the vacuum contribution $\rho_\Lambda^{(\mathrm{obs})}$ reveals a discrepancy of over 120 orders of magnitude. Thus, in order to reconcile the left and right-hand sides of Equation (1.9), the energy density of the bare cosmological constant $\rho_\Lambda^{(0)}$ must be incredibly finely tuned to generate the required cancellations. Theories of super-symmetry (SUSY) can go some way in relieving this tension by bringing the vacuum energy expectation down to the symmetry breaking scale $M_{\mathrm{SUSY}} > 10^3\,\mathrm{GeV}$. However, this leaves a conflict of at least sixty orders of magnitude so still presents a huge issue of fine tuning if choosing to accept a model containing a cosmological constant.

The issues surrounding a cosmological constant make it natural to seek an alternative explanation for accelerated expansion. In fact, the literature surrounding such theories is extensive, falling under the umbrella term of theories of dark energy and modified gravity. Generally, it is quite difficult to draw a complete distinction between the various options when constructing an alternative to the Λ-CDM model, as it is possible to switch between formulations through the appropriate field redefinitions [23, 31, 32]. Either way, they all possess the common feature of introducing additional dynamical degrees of freedom to source accelerated cosmological expansion. To follow, I will begin with the simplest alternative, dynamical dark energy, which will then lead naturally onto a discussion of screened scalar-field theories. There are however, other viable options of interest, and for completeness, a brief account of these will be provided in Section 1.2.4.

1.2.2 Dynamical Dark Energy

Dark energy exists at a very low energy scale $\Lambda \sim 10^{-12}\,\mathrm{GeV}$ which suggests that additional models can be formulated within the frame work of effective field theory [33]. The simplest alternative, invokes a single new degree of freedom, a scalar field ϕ coupled minimally to the metric, which essentially replicates the behaviour of a cosmological constant through the potential energy of the field. Then, the theory must come equipped with some mechanism to drive the energy contribution of the scalar low enough to reproduce the observed cosmic

acceleration. These models generally fall under the umbrella term 'quintessence' models, being described by the action

$$S = \int \mathrm{d}^4x \, \sqrt{-g} \left\{ \frac{M_{\mathrm{PL}}^2}{2} R - \frac{1}{2} \partial_\mu \phi \partial^\mu \phi - V(\phi) \right\} \, . \tag{1.10}$$

A common choice for the potential is the Ratra-Peebles [34] potential given by

$$V(\phi) = \frac{M^{4+n}}{\phi^n} \, , \tag{1.11}$$

which allows the quintessence field to track energy density of matter and radiation in earlier points of cosmic history but come to dominate at late times [35, 36]. This form of quintessence is popular as it goes some way in alleviating the issues of fine tuning faced by the cosmological constant. This is a result of the equations of motion exhibiting an attractor-like solution, allowing the field to converge on the same evolutionary track for a wide-range of initial conditions [37]. Applying the model to an FLRW background and assuming a homogeneous profile such that $\phi \equiv \phi(t)$, it then follows that the scalar field is characterised by the equation of state parameter w_ϕ:

$$w_\phi = \frac{\frac{1}{2}\dot{\phi}^2 - V(\phi)}{\frac{1}{2}\dot{\phi}^2 + V(\phi)} \, . \tag{1.12}$$

It can be seen therefore that replicating the behaviour of a cosmological constant i.e $w_\phi \simeq -1$ can be achieved by a slowly rolling scalar field $\dot{\phi}^2 \ll V(\phi)$. The issue with quintessence fields arises when considering the bounds placed on the field mass in order to influence cosmological expansion. In particular, assuming an approximately static configuration for the scalar field at late times implies that the mass of the field m_ϕ is subject to the bound

$$m_\phi^2 \gtrsim H_0^2 \, , \tag{1.13}$$

where H_0 corresponds to the present day value of the Hubble parameter. As detailed in Reference [35], introducing a minimally coupled scalar-field entails a fifth-force between the matter fields of the standard model with an interaction range going as $\sim m_\phi^{-1}$. In the absence of any symmetries protecting the theory from loop corrections, a quintessence field would inevitably mediate a long range fifth force subject to tight constraints from local tests of gravity.

The central message of the previous discussion is that, when constructing a dynamical theory of a dark energy by introducing a scalar field, equivalence principle violating interactions within the matter sector are inevitable. Fortunately, the tantalising prospect of reproducing the cosmological expansion using a single scalar field does not need to be abandoned just yet. The salvation comes from introducing a conformal coupling to the system, such that the matter fields are coupled minimally to a conformally rescaled metric. Making no assumptions about the form of the scalar field, such a construction falls into a class of models known as scalar-tensor theories of gravity. This class of theories has seen a resurgence in more recent years, particularly since the discovery of screening mechanisms. Simply put, the presence of a screening mechanism leads to a suppression of scalar-matter interactions over short distances, allowing the associated model to comfortably evade terrestrial constraints whilst having the potential to demonstrate rich phenomenology at large scales.

1.2.3 Screened Modified Gravity

Generally speaking, screened models of modified gravity follow the basic recipe of a scalar-tensor theory whilst being purposely designed to avoid any violations of the constraints placed by local tests of gravity. At the heart of these theories are non-linearities that enter into a density dependent effective potential. In general, scalar-tensor theories allow for non-canonical kinetic terms which include derivative self-interactions of the field. As a result, screening can enter through two channels: the first is through non-linearities in the kinetic terms of the theory, and the second is through non-linearities within the self-interaction potential. As will be briefly discussed in Section 1.2.4, the former of these options leads to what is known as Vainshtein screening. However, the departures from General Relativity in such theories only enter at very large distances (i.e cosmological scales) [38] and thus are inconsequential in local fifth-force experiments. Accordingly, the following discussion will be focused on the latter possibility: screening due to non-linearities in the self-interaction potential. Restricting the analysis to canonical scalar fields, a scalar-tensor theory can be written as

$$S = \int \mathrm{d}^4x \, \sqrt{-g} \left\{ \frac{M_{\mathrm{PL}}^2}{2} R - \frac{1}{2} \nabla_\mu \phi \nabla^\mu \phi - V(\phi) \right\} + \int \mathrm{d}^4x \, \mathcal{L}_m \left(\psi_m^{(i)}, \tilde{g}_{\mu\nu} \right) \ , \tag{1.14}$$

where $\mathcal{L}_m$ is the Lagrangian density describing the matter fields $\psi_m^{(i)}$. In contrast to the previous model of dark energy, matter now couples minimally to a conformally rescaled metric through the relation

$$\tilde{g}_{\mu\nu} = A^2(\phi) \, g_{\mu\nu} \ . \tag{1.15}$$

Generally, this coupling can be allowed to vary for different matter species [39] i.e. $A \to A_i$ but can be taken as universal for ease of calculation [33, 35, 40, 41]. This also ensures that the weak equivalence principle holds [42]. The conformal coupling to matter feeds directly into the equation of motion for the scalar through

$$\nabla_\mu \nabla^\mu \phi = \frac{\partial V}{\partial \phi} - A^3(\phi) \tilde{T}^\mu_\mu \frac{\partial A}{\partial \phi} \ , \tag{1.16}$$

where $\tilde{T}^\mu_\mu = \tilde{g}_{\mu\nu} \tilde{T}^{\mu\nu}$ is the trace of the energy momentum tensor defined in the Jordan frame. For most situations of interest it is sufficient to assume the matter distribution to be that of a non-relativistic perfect fluid. As a result, the trace of the stress-energy tensor $\tilde{T}^\mu_\mu = -\tilde{\rho}$ and Equation (1.16) becomes

$$\nabla_\mu \nabla^\mu \phi = \frac{\partial V}{\partial \phi} - A^3(\phi) \tilde{\rho} \, \frac{\partial A}{\partial \phi} \ . \tag{1.17}$$

Now from the principle of minimal coupling, matter fields coupling minimally to the metric implies that the Jordan frame stress energy tensor is covariantly conserved $\tilde{\nabla}_\mu \tilde{T}^{\mu\nu} = 0$. It can be shown [43] that this implies that on sufficiently small spatial scales $\tilde{\rho}$ satisfies the equation

$$\frac{\partial}{\partial t} \left(A^3(\phi) \tilde{\rho} \right) + \nabla \cdot \left(A^3(\phi) \tilde{\rho} \mathbf{v} \right) = 0 \ , \tag{1.18}$$

where $\mathbf{v}$ corresponds to the velocity vector of the matter fluid. The above corresponds to the fluid continuity equation, which implies a conserved density $\rho = A^3(\phi)\tilde{\rho}$ within the Einstein frame. This identifies the relevant Einstein frame matter density field, with such the scalar equation of motion reads

$$\nabla_\mu \nabla^\mu \phi = \frac{\partial V}{\partial \phi} - \rho \frac{\partial A}{\partial \phi} \equiv \frac{\partial V_{\rm EFF}}{\partial \phi} \ . \tag{1.19}$$

It can therefore be seen that introducing a conformal coupling to matter leads to the scalar field evolving according to a density dependent effective potential. It is the crucial interplay between the self-interaction potential $V(\phi)$ and the matter coupling term $\rho \partial A/\partial \phi$ that then allows for the emergence of a screening mechanism. The different choices for the potential and coupling terms generally come in three flavours, corresponding to three different classes of models: the chameleon, the symmetron and the dilaton.

- The Chameleon:

  For the case of the chameleon model [14], the coupling term A is often taken to be linear in the field ϕ and the self-interaction potential typically takes the run-away form.[1] This forces the mass of field fluctuations to respond to the ambient matter density, which by extension controls the interaction range of the field. The nature of chameleon screening means that in regions of relatively high density such as the Solar system, the field also acquires a large mass which severely limits the interaction range allowing it to comfortably bypass local tests of gravity.

- The Symmetron:

  The symmetron model [42] utilises a $\mathbb{Z}_2$ symmetry breaking potential in conjunction with a quadratic coupling to matter entering at $A \propto \phi^2$ to preserve the symmetry of the theory. As the density field increases, the coupling to matter progressively gets weaker until eventually deactivating entirely. At this point, the density field is sufficiently high to restore the spontaneously broken symmetry. In contrast to the chameleon model, screening manifests by diminishing the interaction strength directly as opposed to the interaction range.

- The Dilaton:

  In the low energy limit, string theory returns the classical theory of General Relativity accompanied by an additional scalar field, known as the Dilaton. It was noted that in the strong coupling regime, the Dilaton self-interacts through an exponentially decreasing potential, similar to those of quintessence. However, the Dilaton field also comes equipped with a coupling to matter fields which would entail strong violations of the weak-equivalence principle. Later, a mechanism was proposed by Damour and Polyakov [44] which specified a universal coupling to matter which allowed the Dilaton to circumvent this issue. However, this also implied that the Dilaton would be rendered almost entirely invisible throughout the history of the universe, leading to incredibly

[1] Technically, the coupling term is an exponential function of the field ϕ which gets expanded to linear scales in the low energy limit

small present day deviations from General Relativity. The Damour-Polyakov mechanism was then generalised [45] to trigger an environmentally dependant Dilaton field. In this case, screening behaviour arises as a result of the coupling function possessing some minimum:

$$A(\phi) = 1 + A_2 \left(\phi - \phi_d\right)^2 \ , \tag{1.20}$$

where A_2 is some dimensionless constant. As for the Symmetron, the coupling strength drops in regions of higher density, allowing the model to survive gravitational tests whilst offering observable consequences at large distance scales [40, 45].

The Force Law

A central component of screened scalar-field theories, or indeed scalar-tensor theories in general, is the conformal coupling to matter which leads to a fifth-force interaction. As the matter fields couple minimally to a conformally rescaled metric $\tilde{g}_{\mu\nu}$, it follows that the world-lines of free test particles are determined by the geodesic equation:

$$\ddot{x}^\alpha + \tilde{\Gamma}^\alpha_{\mu\nu} \dot{x}^\mu \dot{x}^\nu = 0, \qquad \alpha = 0, 1, 2, 3 \ , \tag{1.21}$$

where x^α corresponds to the α^{th} component of the test particles space-time co-ordinate four-vector and a dot denotes differentiation with respect to proper time τ. The Christoffel symbols $\tilde{\Gamma}^\rho_{\mu\nu}$ are described by the usual relation to the metric tensor:

$$\tilde{\Gamma}^\alpha_{\mu\nu} = \frac{1}{2} \tilde{g}^{\alpha\gamma} \Big(\partial_\nu \tilde{g}_{\gamma\nu} + \partial_\mu \tilde{g}_{\gamma\nu} - \partial_\gamma \tilde{g}_{\mu\nu} \Big) \ , \tag{1.22}$$

with ∂_μ signifying a partial derivative with respect to the space-time coordinate x^μ. By incorporating the relation between the Einstein and Jordan frame metrics $\tilde{g}_{\mu\nu} = A^2(\phi) g_{\mu\nu}$ it follows that the Christoffel symbols transform as

$$\tilde{\Gamma}^\alpha_{\mu\nu} = \Gamma^\alpha_{\mu\nu} + \frac{\partial \ln A(\phi)}{\partial \phi} \left(\partial_\mu \phi \delta^\alpha_\nu + \partial_\nu \phi \delta^\alpha_\mu - g^{\alpha\beta} \left(\partial_\beta \phi \right) g_{\mu\nu} \right) \ , \tag{1.23}$$

which leads to the following equation for the particle four-acceleration,

$$\ddot{x}^\alpha = - \left\{ \Gamma^\alpha_{\mu\nu} \dot{x}^\mu \dot{x}^\nu + \frac{\partial \ln A(\phi)}{\partial \phi} \left(2 \left(\partial_\mu \phi \right) \dot{x}^\mu \dot{x}^\alpha + g^{\alpha\beta} \left(\partial_\beta \phi \right) \right) \right\} \ . \tag{1.24}$$

The first piece in the above equation is the usual gravitational terms, with the second term corresponding to the correction to the test particle four-acceleration due to the coupling to a scalar field. In the non-relativistic limit relevant to any local fifth-force experiments, a test particle subject to a Newtonian gravitational Φ therefore experiences an acceleration $\vec{\mathbf{a}}$:

$$\vec{\mathbf{a}} = -\vec{\nabla} \left[\Phi + \phi \frac{\partial \ln A(\phi)}{\partial \phi} \right] \ . \tag{1.25}$$

Thus it can be seen that in a scalar-tensor theory of gravity with a conformal coupling such that $\tilde{g}_{\mu\nu} = A^2(\phi)\, g_{\mu\nu}$, a test particle moves under an additional scalar potential of the form $\partial \ln A(\phi) / \partial \phi$.

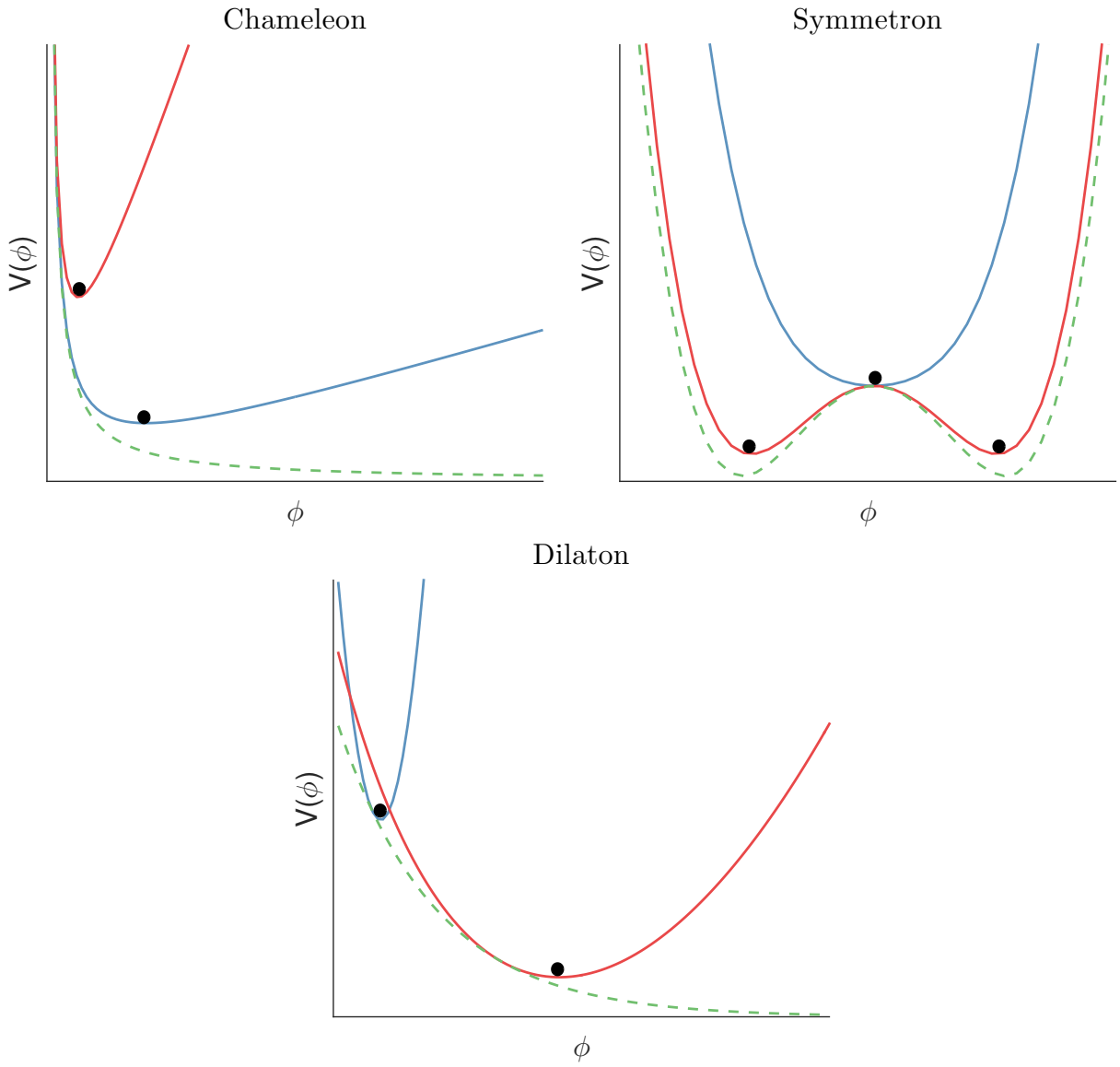

Figure 1.2: Figure capturing the general features of the screening mechanisms present in the chameleon, symmetron and dilaton Models. The red and blue lines represent the effective potentials for low and high densities respectively. The self-interaction potential in each case is pictured with the dashed green line.

1.2.4 Alternative Models

Dynamically screened scalar fields are unique modifications to gravity in the sense that they offer testable predictions across a host of local fifth-force experiments. There are however, a number of other attractive models aiming to address the tension between observations and the predictions of General Relativity at large scales. A very informative account of the various options is presented in Reference [32], I will briefly cover some of the alternative candidates below:

- Horndeski Theories:

  The three screened scalar field theories presented previously in Section 1.2.3 only comprise a fraction of the models built within the framework of a scalar-tensor theory. Many efforts have been made to construct the most general consistent theory of gravity described by a metric interacting with a scalar field. Consistency in this sense relies on avoiding the so-called Ostrogradski instabilities [46] which typically arise when dealing with equations of motion higher than second order in time. As such, much of the focus within scalar-tensor theories of gravity has been towards those leading to second-order equations of motion. The most general formulation of such a theory first appeared in work by Horndeski in 1974 [47], although it was largely overlooked until later appearing in 2011 [48]. Either way, the Lagrangian describing a system admitting second-order equations of motion was found to be

$$\begin{aligned}\mathcal{L} = & K(\phi, X) - G_3(\phi, X)\Box\phi \; + \; G_4(\phi, X)R \\ & + G_{4,X}(\phi, X)\left[(\Box\phi)^2 - (\nabla_\mu\nabla_\nu\phi)^2\right] \; + \; G_5(\phi, X)G_{\mu\nu}\nabla^\mu\nabla^\nu\phi \\ & - \frac{1}{6}G_{5,X}(\phi, X)\left[(\Box\phi)^3 - 3\,(\Box\phi)\,(\nabla_\mu\nabla_\nu)^2 + 2\nabla^\mu\nabla_\alpha\phi\nabla^\alpha\nabla_\beta\phi\nabla^\beta\nabla_\mu\phi\right] \; ,\end{aligned} \tag{1.26}$$

  where the d'Alembertian $\Box$ denotes the derivative operator $\nabla_\mu\nabla^\mu$. The theory contains four arbitrary functions K, G_3, G_4, G_5, with X linked to the scalar field via $X \equiv -\frac{1}{2\Lambda^4}\left(\partial_\mu\phi\partial^\mu\phi\right)$. Note that in this case, Λ is an energy scale of the theory not relating to the cosmological constant. In fact, broader generalisations than the above have been recovered by relaxing the limit to second-order equations of motion whilst managing to avoid any Ostrogradski instabilities, as demonstrated in Reference [49]. A well established subset of the class of theories contained by Equation (1.26) are the galileon models, which are arrived at in taking the limit of a flat space-time [50]. The cubic galileon is the simplest version:

$$\mathcal{L} = \frac{M_{\rm PL}^2 R}{2} - \frac{1}{2}\partial_\mu\phi\partial^\mu\phi - \frac{1}{\Lambda^3}\Box\phi\partial_\mu\phi\partial^\mu\phi \; , \tag{1.27}$$

  which has interesting phenomenological consequences due to the emergence of a Vainshtein screening mechanism. In this case, the cubic derivative-interaction term becomes important near matter sources, acting to suppress the gradient of the galileon field responsible for a fifth-force. At larger length scales, this interference between the kinetic non-linearities and the spatial gradient begins to fade, opening up the possibility to study galileon gravity within the context of large scale structure [51].

- Massive Gravity and DGP:

  A natural launch point into the discussion of massive gravity comes from the Yukawa potential describing the interactions of massive fields:

$$V(r) \sim \frac{e^{-mr}}{r} \ , \tag{1.28}$$

  which encapsulates the idea that forces mediated by a particle of non-zero mass suffer from an exponential suppression of the interaction range. Operating over short length scales, the exponential component would be sub-dominant leading to the familiar $1/r$ potential recovered in the Newtonian limit of General Relativity. At large distances however ($m^{-1} \sim H_0$), the story changes as the decaying exponential comes into play, severely throttling the interaction strength. This behaviour is remarkably reminiscent of the current cosmological picture, where the idea could be that the observed cosmic acceleration arises due to the weakening of gravity at large scales. The idea of introducing a graviton mass has been around for sometime, although it has suffered a turbulent history since its first appearance in work by Fierz and Pauli in 1939 [52] which described the action of a free graviton. The first interacting model of massive gravity to arrive considered a linear response to matter sources [53] but struggled to recover the predictions of GR in the massless limit in something known as the vDVZ discontinuity. A potential cure for this came with the first non-linear extensions of an interacting massive graviton, which surfaced in work by Vainshtein in the early seventies [54]. The key findings were that there is a new characteristic length scale describing gravity around a massive source, the Vainshetin radius r_V, below which the non-linearities present within the theory come to dominate. This historically marked the first indication of a Vainshtein screening mechanism. Unfortunately it very quickly came into fruition that generically, non-linear completions of massive gravity propagate a ghost-like degree of freedom. This complication was recently resolved in References [55] and [56] which sparked a renewed interest in massive gravity. At present, dGRT gravity, a model discussed in Reference [56], appears to be the best hope of realising a phenomenologically viable theory of massive gravity: capable of harmonising with the predictions of GR through an efficient local screening of the gravitational interaction via the Vainshtein mechanism.

  Another perspective is to view the effective mass of the graviton as a resonance arising in extra-dimensional setups, as in a brane-world scenario such as the DGP model [57]. The idea is that matter fields are confined to a 4-dimensional brane embedded within an infinite 5-dimensional bulk Minkowski space-time. Locally, gravitational physics appears the same from the perspective of a 4-dimensional observer. However, in moving up to infrared distance scales, the signatures of living higher-dimensional space become apparent as gravitons escape the brane, resulting in a weakening of the gravitational potential. Unfortunately, stable self-accelerating solutions have yet to be found within the brane-world paradigm [32], although the benchmark DGP model continues to inspire further research on the subject [58].

1.3 The Chameleon Model

In the case of the chameleon model, the desired screening behaviour is achieved through an appropriate choice in the self-interaction $V(\phi)$ such that the expectation value and the mass of the field respond to the ambient density. The conformal factor $A(\phi)$ connecting the matter fields to the chameleon is chosen to such that $\tilde{g}_{\mu\nu} = \exp(2\phi/M)g_{\mu\nu}$, which draws parallels with the conformal scalar coupling that emerges in the low energy limit of string theory [45]. Operating at the energies relevant to a lab setup ($\phi \ll M$) allows for the conformal factor to be linearised to first order as $A \simeq 1 + \frac{\phi}{M}$. This leads to the dynamics of a scalar field ϕ being governed by an effective potential:

$$V_{\rm EFF}(\phi) = V(\phi) + \frac{\rho\phi}{M} \, , \tag{1.29}$$

where $V(\phi)$ is the scalar field's self-interaction potential, ρ is the ambient matter density and M is the coupling strength to matter. First proposed by Koury and Weltman in References [39] and [60], it was shown that screening behaviour of chameleon type could be realized generically through using self-interaction potentials of the run-away form. That is, those satisfying the following conditions:

- $V(\phi)$ is monotonically decreasing.
- $\lim_{\phi\to 0} \mathrm{V}(\phi), \mathrm{V}_{,\phi}/\mathrm{V}, \mathrm{V}_{,\phi\phi}/\mathrm{V}_{,\phi} \to \infty$.
- $\lim_{\phi\to \infty} \mathrm{V}(\phi), \mathrm{V}_{,\phi}/\mathrm{V}, \mathrm{V}_{,\phi\phi}/\mathrm{V}_{,\phi} \to 0$.

As captured by Figure 1.3, the interplay between the bare-potential and the ambient density terms triggers a response of the chameleon field to the environment. This behaviour is general to any self-interaction potentials that conform with the above requirements. As demonstrated in References [39, 60] and [61], it follows that the characteristic behaviour of the chameleon field can be revealed without necessarily taking on an explicit form for the bare potential term. Nonetheless, the prototypical example of a potential satisfying the above is the Ratra-Peebles potential (Equation (1.11)) which is the most commonly adopted choice within the literature due to its connection with quintessence models [35, 62, 63] and is restated below for convenience:

$$V(\phi) = \frac{\Lambda^{4+n}}{\phi^n} \, . \tag{1.30}$$

Generally, meeting the three conditions imposed on the form of the potential would imply that the chameleon field exhibits a screening mechanism for $n \geq 1$. However, it is possible in this case to relax these conditions slightly as screening behaviour can also be realised for negative even values of n [28], for which the Ratra-Peebles potential simply becomes a polynomial. In fact, another popular example is the exponential potential which assumes the form

$$V(\phi) = \Lambda^4 \exp\left(\frac{\Lambda^{\rm n}}{\phi^{\rm n}}\right) \, . \tag{1.31}$$

The essential difference between the two arises in the limit of $\lim_{\phi\to\infty}$ for which the Ratra-Peebles potential vanishes whereas the exponential potential approaches Λ^4. However, at

length scales relevant to a local fifth force experiment such as atom interferometry, these two choices are dynamically equivalent. Hereinafter the $n = 1$ form will be adopted from the Ratra-Peebles potential. It should be noted that there is nothing particularly special in taking $n = 1$, and ultimately the decision was made only to establish consistency with the previous work on the chameleon field applied to an atom interferometry experiment [64]. For the purposes of lab-based fifth force experiments it is sufficient to search for steady state solutions of the chameleon field. By incorporating the chosen $n = 1$ inverse power-law potential into the non-relativistic form of Equation (1.19), it then follows that the behaviour of the chameleon field can described by the equation

$$\nabla^2\phi = -\frac{\Lambda^5}{\phi^2} + \frac{\rho}{M} \,, \tag{1.32}$$

which links the chameleon to an effective potential of the form

$$V_{\rm EFF} = \frac{\Lambda^5}{\phi} + \frac{\rho\phi}{M} \,. \tag{1.33}$$

Two important quantities to consider are then the equilibrium value for the field, and the mass of fluctuations of the field about this value. The equilibrium value for the chameleon, denoted $\phi_{\rm min}$, corresponds to the field value minimising the effective potential and is given by

$$\phi_{\rm min} = \left(\frac{M\Lambda^5}{\rho}\right)^{1/2} \,. \tag{1.34}$$

The mass of the field is arrived at in the usual way by evaluating the second derivative of the effective potential for fluctuations around the expectation state $\phi_{\rm min}$ to give

$$m_\phi^2 = 2\left(\frac{\rho^3}{M^3\Lambda^5}\right)^{1/2} \,, \tag{1.35}$$

where it is evident that in regions of high density, the field is not only suppressed but has a much shorter interaction range due to a larger mass and thus reduced Compton wavelength.

1.3.1 The Thin-Shell Mechanism

A trademark feature of the screened scalar field theories is the presence of a thin-shell mechanism which essentially acts to confine fifth-force contributions to a thin-shell lying at the surface of the source. This is most readily seen by considering solutions around a spherical source object, with a detailed account of all three models (chameleon, symmetron and the dilaton) presented in Reference [41]. For the case of the chameleon, the field equation (Equation (1.32)) around a spherically symmetric source becomes

$$\frac{1}{r^2}\frac{\mathrm{d}}{\mathrm{d}r}\left(r^2\frac{\mathrm{d}\phi}{\mathrm{d}r}\right) = -\frac{\Lambda^5}{\phi^2} + \frac{\rho}{M} \,, \tag{1.36}$$

with r being the radial value in spherical polar co-ordinates. The non-linear form of the above makes finding an exact solution a huge challenge, and as a result the established

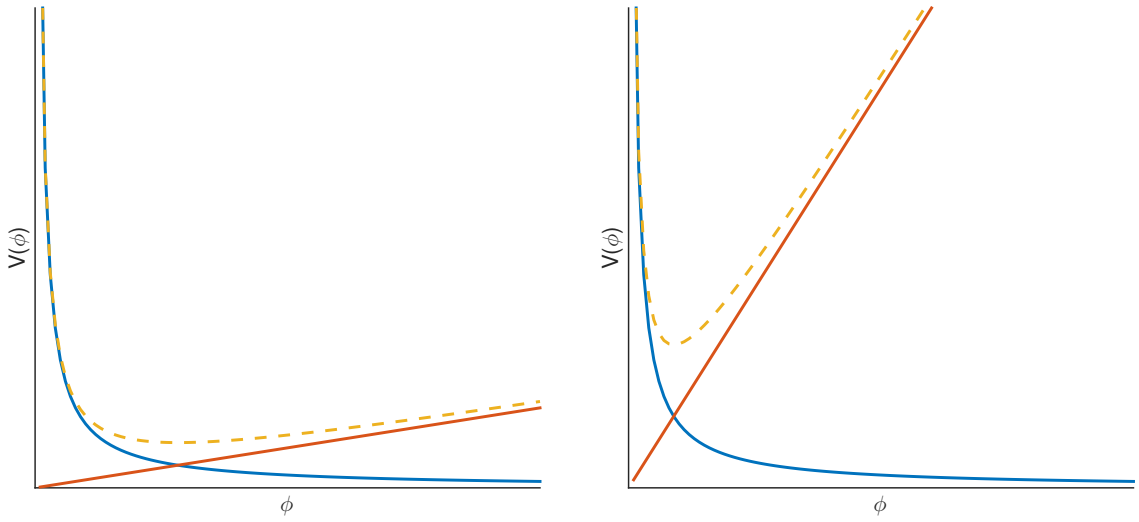

Figure 1.3: Figure depicting how the effective potential (dashed) responds to the ambient matter density. The linear density contribution corresponding to the orange line, and the bare potential of run-away form given by the blue line. Moving from left to right corresponds to an increase in the value of the ambient matter density ρ.

approach in the literature has been to construct the solution in a piecewise manner. The idea is to picture the effective potential as acting on a test particle rolling outwards from the source, as depicted Figure 1.4. In this sense, the particle begins within the proximity of the potential minima of the source before traversing a segment of the effective potential dominated by the density contribution. Upon escaping, the fictional particle will then fall into an approximately parabolic region of the effective potential describing the background. Schematically, this corresponds to compartmentalising field solution into three distinct regions, each described by a separate field equation: a core, within which the field lies within the proximity of the potential minima, a shell, where the effective potential grows linearly, and an exterior, where the field stays near the potential minima of the background.

Lying near the respective equilibrium values of the source and the background, the field equations pertaining to the core and exterior regions are best described through a parabolic approximation:

$$\nabla^2\phi \simeq m_\phi^2\left(\phi - \phi_{\rm min}\right) \ , \tag{1.37}$$

whereas the density driven shell region behaves according to

$$\nabla^2\phi \simeq \frac{\rho_{\rm obj}}{M} \ , \tag{1.38}$$

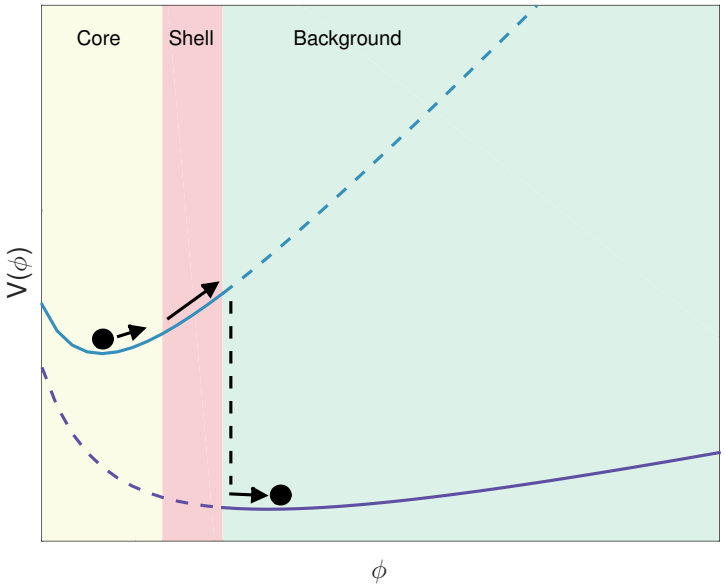

Figure 1.4: Visualisation of the 'rolling potential' experienced by a test particle. Beginning at the potential minimum within the source, traversing the linear density dominant contribution before falling into the proximity of the potential minima of the background. The blue line signifies the effective potential within the source and the purple line denotes that of the background. Regions where each effective potential becomes relevant are represented by the solid line, with the dashed lines simply being continuations of the functions for the purpose of illustration.

with $\rho_{\rm obj}$ denoting the density of the source. Collectively then, solving around a spherical source object reduces to the following boundary-value problem

$$\frac{1}{r^2}\frac{\mathrm{d}}{\mathrm{d}r}\left(r^2\frac{\mathrm{d}\phi}{\mathrm{d}r}\right) = m_{\rm obj}^2\left(\phi - \phi_{\rm min}^{\rm (obj)}\right), \qquad 0 \leq r \leq R_S\ , \tag{1.39a}$$

$$\frac{1}{r^2}\frac{\mathrm{d}}{\mathrm{d}r}\left(r^2\frac{\mathrm{d}\phi}{\mathrm{d}r}\right) = \frac{\rho_{\rm obj}}{M}, \qquad R_S \leq r \leq R\ , \tag{1.39b}$$

$$\frac{1}{r^2}\frac{\mathrm{d}}{\mathrm{d}r}\left(r^2\frac{\mathrm{d}\phi}{\mathrm{d}r}\right) = m_{\rm bg}^2\left(\phi - \phi_{\rm min}^{\rm (bg)}\right), \qquad R \leq r \leq \infty\ , \tag{1.39c}$$

where $m_{\rm obj}$, $\phi_{\rm min}^{\rm (obj)}$, $m_{\rm bg}$, and $\phi_{\rm min}^{\rm (bg)}$ are the masses and field expectation values of the source and background respectively. Partitioning the problem in this way introduces a new unknown constant to the problem R_S, corresponding to the position of the interface between the interior shell and core regions. This quantity is to be later identified when imposing boundary conditions on the above system of equations. The general solutions to Equations (1.39a)-(1.39c) are readily found to be

$$\phi(r) = \frac{A}{R}\sinh\left(m_{\rm obj}r\right) + \frac{B}{R}\cosh\left(m_{\rm obj}r\right) + \phi_{\rm min}^{\rm (obj)}, \qquad 0 \leq r \leq R_S\ , \tag{1.40a}$$

$$\phi(r) = \frac{1}{6}\frac{\rho_{\rm obj}}{M}r^2 + Cr + D, \qquad R_S \leq r \leq R\ , \tag{1.40b}$$

$$\phi(r) = \frac{E}{r}e^{m_{\rm bg}r} + \frac{F}{r}e^{-m_{\rm bg}r} + \phi_{\rm min}^{\rm (bg)}, \qquad R \leq r \leq \infty\ . \tag{1.40c}$$

Several of these constants can be eliminated immediately by considering the limiting forms of the solution. For example, as the core region is defined perturbatively around $\phi_{\rm min}^{\rm (obj)}$, it follows that $\phi \to \phi_{\rm min}^{\rm (obj)}$ as $r \to 0$ which implies that $B = 0$. Furthermore, requiring the exterior solution to acquire the background expectation value as $r \to \infty$ dictates that the constant E must also be set to zero. As noted in Reference [64], the leading anharmonic correction to the potential within the core region goes as $(\phi - \phi_{\rm min}^{\rm (obj)})^3/\phi_{\rm min}^{\rm (obj)}$ which implies that $(\phi - \phi_{\rm min}^{\rm (obj)}) \ll \phi_{\rm min}^{\rm (obj)}$ for the harmonic approximation to remain valid. Due to the hyperbolic nature of the $\sinh\left(m_{\rm obj}r\right)$ appearing in Equation (1.40a), the field can be thought to remain mostly frozen at the value $\phi_{\rm min}^{\rm (obj)}$. As soon the hyperbolic term begins to activate, the harmonic approximation essentially immediately breaks down and the field transitions into the shell regime of the effective potential.[2] A similar argument is presented in Reference [60]. Because of this, it follows that it is sufficient to describe the core region using the constant piece alone, that is $\phi = \phi_{\rm min}^{\rm (obj)}$. This leaves four unknown constants R_S, C, D, and F, to be obtained by imposing Dirichlet-Neumann boundary conditions across the two

[2] A more informal way of saying this would be: As soon as the hyperbolic sine term begins to contribute, it almost immediately becomes irrelevant.

interfaces R_S and R. Matching the field and its first derivatives across the two boundaries fully specifies the piecewise solution spanning the core, shell, and exterior to be

$$\phi(r) = \phi_{\rm min}^{\rm (obj)}, \qquad 0 \leq r \leq R_S \,, \tag{1.41a}$$

$$\phi(r) = \phi_{\rm min}^{\rm (obj)} + \frac{M_{\rm obj}}{M}\frac{1}{8\pi R^3}\left(\frac{r^3 - 3R_S^2 r + 2R_S^3}{rR_S^2}\right), \qquad R_S \leq r \leq R \,, \tag{1.41b}$$

$$\phi(r) = \phi_{\rm min}^{\rm (bg)} - \frac{1}{4\pi R}\frac{M_{\rm obj}}{M}\left\{1 - \left(\frac{R_S}{R}\right)^3\right\}\frac{R}{r}e^{-m_{\rm bg}r}, \qquad R \leq r \leq \infty \,, \tag{1.41c}$$

with $M_{\rm obj}$ denoting the mass of the source object and the position of the core-shell interface, R_S, is given by the expression

$$R_S = R\sqrt{1 - \frac{8\pi}{3}\frac{M}{M_{\rm obj}}R\phi_{\rm min}^{\rm (bg)}} \,. \tag{1.42}$$

It is beneficial in a discussion of chameleon screening to introduce the fractional contribution of the shell region $\Delta R/R$ which can be used to demonstrate how the intensity of the screening effect responds to the various theory and source parameters:

$$\frac{\Delta R}{R} = \frac{R - R_S}{R} = \frac{4\pi M R}{3M_{\rm obj}}\phi_{\rm min}^{\rm (bg)} \,. \tag{1.43}$$

As internal field variations are confined to the shell, the interpretation is that it is only the source mass within this region contributes to an external force. Therefore Equation (1.43) captures some very important features of the chameleon screening mechanism. Firstly, the presence of the background solution shows how the force profile will differ for the same source object immersed in different environments. In particular, the inverse density dependence of $\phi_{\rm min}^{\rm (bg)}$ causes a suppression of the force in higher density regions, and vice versa. Secondly, the explicit appearance of the source radius R shows how varying its size whilst preserving the mass will still feed into the screening effect. Finally, increasing the mass of the source will further magnify the screening effect. Ultimately, this is what allows the chameleon field to circumvent the tight constraints placed by tests of the weak equivalence principle: the Earth is sufficiently massive to drive the sourced chameleon field into the screened regime [39].

Equation (1.42) also shows that once a certain threshold is met, the radial position of the shell falls to zero at which point screening completely de-activates. This naturally divides the solution of the chameleon field around a spherical source into two regimes: screened and unscreened, which can be packaged together as seen below:

$$\phi(r) = \phi_{\rm min}^{\rm (bg)} - \kappa\frac{M_{\rm obj}}{M}\frac{e^{-m_{\rm bg}r}}{r}, \qquad \kappa = \begin{cases} 1 & \text{if} \quad M_{\rm obj}/R \leq 4\pi M\phi_{\rm min}^{\rm (bg)} \\ 4\pi R\phi_{\rm min}^{\rm (bg)}\frac{M}{M_{\rm obj}} & \text{if} \quad M_{\rm obj}/R > 4\pi M\phi_{\rm min}^{\rm (bg)} \end{cases} \,. \tag{1.44}$$

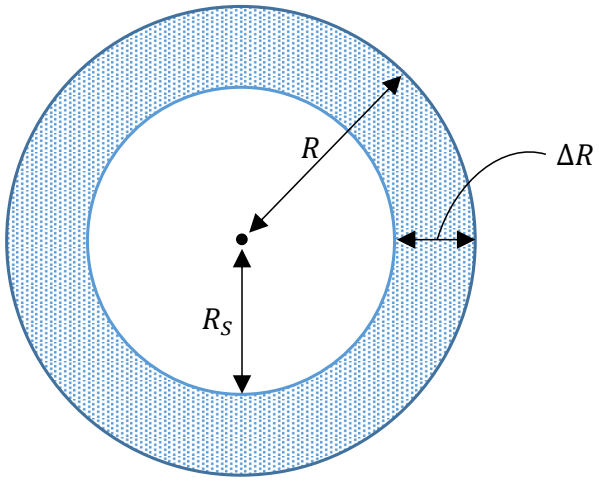

Figure 1.5: Figure showing an example of the thin-shell mechanism at play for a spherical source object. The interior structure of the field is decomposed into two distinct regions, a core, where the field gradient remains zero, and a shell (identified with blue shading) to which all of the field variations and thus force contributions are confined.

The force law for the chameleon field follows from incorporating the form of the conformal coupling into the acceleration equation (Equation (1.25)) previously derived, to give

$$\vec{\mathbf{a}} = -\vec{\nabla}\left\{\Phi + \frac{\phi}{M}\right\} \ . \tag{1.45}$$

The acceleration above was derived for a test particle and thus fails to take into account any screening effects manifesting due to the finite extent of an object moving through a chameleon potential. It was shown in Reference [64] through a complete covariant treatment of the theory, that extending the force law to describe extended bodies brings down an additional screening factor such that the equation of motion reads

$$\vec{\mathbf{a}} = -\vec{\nabla}\left\{\Phi + \kappa^{(E)}\frac{\phi}{M}\right\} \ , \tag{1.46}$$

where $\kappa^{(E)}$ takes the same form as κ previously defined for the source, in this case exchanging source object parameters for those describing the extended body. It is clear therefore that the chameleon force between two sufficiently large bodies suffers from a compounded suppression effect: now two screening parameters κ and $\kappa^{(E)}$ feed into the interaction strength.

1.3.2 Chameleon Cosmology

In order for chameleon gravity to remain a viable alternative to General Relativity, the parameters of the theory must be engineered such as allow the chameleon evade the stringent

local tests of gravity. As discussed in Reference [14], this imposes the condition that the chameleon interaction is screened within the milky-way, which translates directly to the mass bound

$$m_{\rm cosmo}^{-1} \gtrsim 10^{-3} H_0^{-1} \sim \text{Mpc} \ , \tag{1.47}$$

where H_0 is the Hubble constant. It follows from this that when considering linear perturbations, that the cosmological evolution of the density contrast is indistinguishable to Λ-CDM. Not only this, it is shown in Reference [35] that requirement for the Milky Way to be screened also implies that the late-time acceleration arising from the value of the scalar energy density is sourced purely from cosmological constant contribution, as both the kinetic and potential energies (absent of a constant term) of the scalar must be suppressed. The mass bound of Equation (1.47) suggests that the observable effects of the chameleon model will begin to surface at distance scales $\leq$ Mpc. Because of this, coming years should see a rise in constraints coming from probes of large scale structure such as EUCLID [65] and the Dark Energy Survey [66].

The main tension surrounding the cosmological viability of the chameleon comes from considerations of how the effective field theory description fits in the lead up to big bang nucleosynthesis (BBN). In particular, the conformal coupling $A(\phi)$ influences the masses of the matter fields ψ in the following way:

$$m_\psi = A(\phi) m_\psi^0 \ , \tag{1.48}$$

with m_ψ^0 corresponding to the mass of the matter field in the Jordan Frame. Large variations in the chameleon field will therefore connected to large variations in particle masses. It was demonstrated in Reference [62] that in order to satisfy the constraints on the time variations of the masses since BBN [24, 25], it is required that the chameleon field must hit the minima of its effective potential prior to the onset of BBN. This follows from the fact that in the radiation dominated epoch of the early universe, whenever a particle species becomes non-relativistic, there is a jump in the stress energy tensor, imparting energy to the chameleon field which acts as to kick it towards the minimum of its effective potential. Thus, during BBN where species like the electron decouple [33], if not already at its minima, the chameleon would experience a kick leading to a significant variation of particle masses, in conflict with observation.

The problem of avoiding variations in particle masses was initially dealt with by demonstrating that the minimum of the chameleon effective potential acts an attractor solution prior to the onset of BBN [62]. However, the approach detailed in Reference [62] also relied on a cascade of kicks arising from the decoupling of heavier particles. It was later shown in Reference [26] that the behaviour of these kicks is to accelerate the field to very high velocities which leads to rapid variations of the chameleon effective mass, and in turn, excites very energetic modes which invalidates any description of the chameleon as an effective field theory. The only way to circumvent these issues was found to be to drive the chameleon-matter coupling to sufficiently low values [26], which would undermine the purpose of lab based tests of the chameleon. Thus, for generic initial conditions, the true evolution of the chameleon field approaching BBN is unknown which casts doubt on the belief that the chameleon reaches

the minimum of its effective potential prior to the decoupling of the electron.

In light of this, there are a couple of stances one would take. The first is that the effective field theory describing the evolution of the chameleon is only valid after BBN. This makes sense, as many of the phenomenological implications of the chameleon arise from making use of the non-relativistic perfect fluid approximation, which only becomes valid at energies below the electron mass [33]. In this case, the cut off of the effective theory would lie around the MeV scale.[3] Alternatively, one could operate under the belief that a viable alternative to General Relativity must remain predictive as far back as BBN. In this case, recent work [27] has proposed an extension to the classical chameleon model within which a high energy modification of the theory can be used to dynamically renormalise the scalar-matter coupling. As a result, the scalar evolution is stabilised in the presence of kicks whilst at the same time, the classical late-time description of the theory remains intact.

1.4 Fifth Force Experiments

The rich phenomenology surrounding dynamically screened scalar field theories makes them a target for a wide range of experimental searches, ranging from lab based experiments through to studies of large scale structure formation. The catalogue of these searches turns out to be quite extensive, and so I will restrict any attention to the most competitive of these within the current generation: torsion balance experiments, precision atomic tests, and atom interferometry. A comprehensive account of the entire collection of experimental bounds was recently presented in Reference [28]. Moreover, the chameleon field will continue to be the focal point of discussion, as it remains the the most examined theory within the literature. The three methods to be outlined directly probe the fifth-force interaction with matter. However, there has also been a rise of bounds appearing from axion-type experiments which instead constrain the photon-chameleon coupling. Amongst these, are inspired generalisations of 'light shining through walls' experiments [67], where the signature of the chameleon field is studied through the hypothetical existence of some afterglow effect [68, 69]. In a nutshell, the magnetically induced conversion of chameleon particles to photons could lead to a regeneration of light to be explored by optical experiments. However, as noted in Reference [28], the photon-chameleon coupling isn't an integral component of the chameleon mechanism, with such interactions having to be put in by hand. As the bulk of this research was performed with an application to an atom interferometry experiment in mind, a significant portion of the subsequent discussion will be devoted to it. Before this however, I will provide a brief account of the two competing alternatives:

- Torsion-balance Experiments:

  Pre-dating the cosmological motivation for fifth-force searches, torsion-balance experiments were initially introduced in 1964 [70] as a means to test the principle of equiva-

[3] Introducing a cut off in this way is in some sense favoured when considering the radiative corrections to the chameleon mass due to matter interactions. As shown in [33], the effect of the neutrons when accounting for these correction is to shift value of the cosmological constant by a value compatible with observation.

lence. The weak equivalence principle (WEP) states that all bodies, regardless of their composition, follow the same trajectories in free fall. When translated into the language of Newtonian physics, the weak equivalence principle asserts that inertial mass and gravitational mass are indistinguishable [71]. Schematically, the torsion-balance experiment involves the balancing of two test bodies connected by a rigid frame that is suspended by a flexible fibre. External forces acting on these test bodies entail a torque about the fibre axis, causing the entire instrument to oscillate. If test bodies are selected to be of identical mass but different internal structure, torques arising from different moments of inertia can then be corrected for in the presence of a gravitational force given by the inverse square law. Accordingly, any subsequent oscillation can then be tied to departures from the WEP. It was later realized however, that WEP tests can be appropriated to the search for Yukawa type interactions [72], making the experiment the ideal probe for the chameleon field. The strongest constraints to date come from the torsion-balance experiment conducted by the Eot-Wash group [73] which was able to study chameleon physics down to sub-millimetre scales.

- Precision Atomic Tests:

  Precision spectroscopic measurements of atomic transition frequencies are paramount when it comes to testing our fundamental understanding of the laws of physics [74]. Quantum electrodynamics for example, builds a theoretical description of hydrogen energy levels using four parameters: the fine structure constant α, the electron-proton mass ratio m_e/m_p, the proton charge radius r_p and the Rydberg constant. Each of these, can be measured to remarkable precision by studying the spectral lines of atomic hydrogen. It was demonstrated in Reference [75], that a scalar-mediated force will introduce a perturbation in atomic energy levels which could be referenced against the known transition frequencies determined by high precision spectroscopy. In particular, it was shown in Reference [28] that electrons orbiting atomic hydrogen in the presence of a chameleon field will receive a correction term to their Hamiltonian of the form

$$\delta H = \frac{m_e}{M}\phi_{\rm nuc} \ , \tag{1.49}$$

  where m_e is the electron mass and $\phi_{\rm nuc}$ is the chameleon field profile surrounding the atomic nucleus. It follows that in modelling the hydrogen nucleus as an unscreened spherical source, the leading three energy levels of atomic hydrogen, $1s$, $2s$, and $2p$, are shifted according to

$$\delta E_{1s} = -\frac{m_p m_e}{4\pi M^2 a_0} \ , \tag{1.50a}$$

$$\delta E_{2s} = \delta E_{2p} = -\frac{m_p m_e}{16\pi M^2 a_0} \ , \tag{1.50b}$$

  which neglects any contributions arising due to a photon-chameleon coupling, where e is the electron charge, m_p is the proton mass and a_0 is the Böhr radius. Note that as the hydrogen nucleus is unscreened, the energy corrections appearing in the above are independent of the chameleon self-coupling strength Λ. The strongest spectroscopic

constraints come from the $1s - 2s$ transition which constrains the matter coupling strength M to be

$$M \gtrsim 10^4 \text{ GeV} . \tag{1.51}$$

1.4.1 Atom Interferometry

Since its first conception in 1985 [76], with the first experimental realisations appearing in 1991 [77–80], the atomic interferometer has become one of the most powerful instruments in measuring absolute values of acceleration around today. Atom interferometry relies on the same principles as the more familiar Michelson interferometer: a coherent beam is divided into two parts that subsequently traverse different paths before later being recombined. Any difference in optical path length between these two paths then results in the formation of an interference pattern to be observed by the detector.

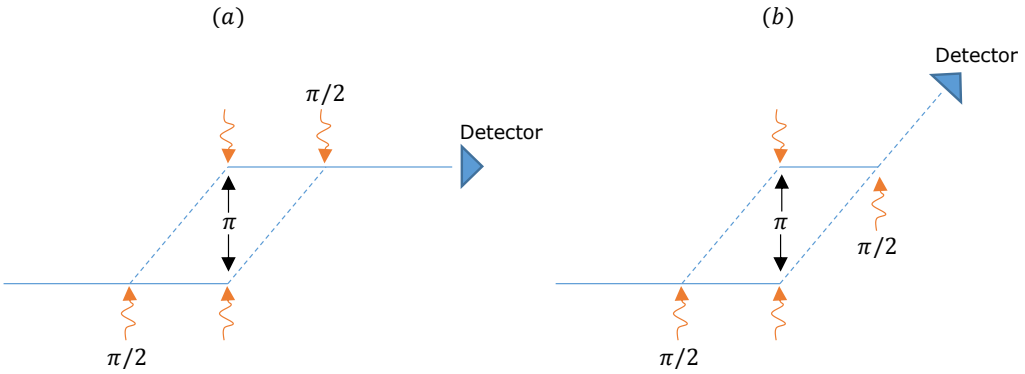

Figure 1.6: Diagrams capturing the several stages of atom interferometry leading to beam splitting and recombination. The experimental procedure is broken down into a sequence of three pulses: the atomic wave function is initially split by the first $\pi/2$, followed by a π pulse acting to reverse their relative motion. The final pulse then acts to overlap the partial wave packets. The two possible routes are depicted by (a) and (b) which depends on the tuning of the final $\pi/2$ pulse.

The foundation of an atom interferometry experiment is the quantum mechanical phenomenon wave-particle duality, which tells us that the interference phenomena observed within optical interferometry should arise in an equivalent scenario for atomic beams. Schematically, atomic wave functions are split and recombined using a sequence of laser pulses tuned to the hyperfine (angular momentum) transition energies of the atomic ground state. Due to the conservation of momentum, absorption of laser photons will induce a change in recoil velocity of allowing control over the spatial separation of atoms.

The initial splitting of the beam is achieved through a "$\pi/2$" pulse, which divides the initial atomic state, labelled $|1, p\rangle$ into an superposition of the two states $|1, p\rangle$ and $|2, p + \hbar k\rangle$, with p the initial particle momentum and k the photon wave-number respectively. Wave packets pertaining to the $|2, p + \hbar k\rangle$ state will begin to branch off with a recoil velocity

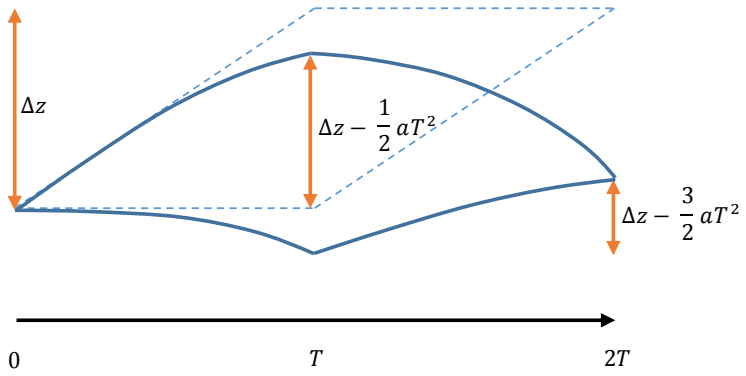

Figure 1.7: Figure displaying how the atomic trajectories within an atom interferometry experiment vary in the presence of a uniform acceleration a. For reference, the dashed line indicates the trajectory in the absence of any external forces.

of $\hbar k/m_A$ (where m_A is the mass of the atom). After some time interval, the states are inverted and separation is reversed via a "π" pulse. This pulse stimulates the transitions $|2, p + \hbar k\rangle \rightarrow |1, p\rangle$ and $|1, p\rangle \rightarrow |2, p + \hbar k\rangle$, causing the previously divergent states to converge. At the point of recombination, a final "$\pi/2$" pulse places the two wave packets into the same hyperfine state (either $|1, p\rangle$ or $|2, p + \hbar k\rangle$, aligning their motion for detection. The entire process incorporating each of these transitions is shown in Figure 1.6.

From a mathematical standpoint, the phase shifts associated with traversing a given path decompose into two parts: the phase shift entailed by the free evolution of the atom, and that arising from interactions with the optical pulses. The measure of the contribution due to the free-evolution of the atom comes from the Feynman's path integral formulation of quantum mechanics [81] , which states that the atomic wave-functions Ψ evaluated at initial and final space-time points (t_i, x_i) and (t_f, x_f) are linked through the relation

$$\Psi(t_f, \vec{x}_f) = e^{iS_{\mathrm{CL}}} \Psi(t_i, \vec{x}_i) \ , \tag{1.52}$$

where the classical action S_{CL} is defined by

$$S_{\mathrm{CL}} = \int_{t_i}^{t_f} \mathcal{L}(x, \dot{x}) \, \mathrm{d}t \ , \qquad \mathcal{L} = T - V \ , \tag{1.53}$$

where T and V respectively denote the kinetic and potential energies of the atom, with its dynamics specified by the solutions of the Euler-Lagrange equations. Equation (1.52) holds true over scales such that S_{CL} is much greater than one, else a full path integral treatment is required which involves summing over all possible paths connecting the initial and final points [82]. In treating the atom as a propagating plane wave, Equation (1.52) implies a phase change at the level of the action, denoted $\Delta^{(A)}$, given by

$$\Delta^{(A)} = S_{\mathrm{CL}} \ . \tag{1.54}$$

For the cases of a uniform gravitational force profile, and by extension that for any scalar interaction, it can be shown that phases shifts arising from classical path differences exactly cancel [40, 64, 82] meaning that the phase differenced measure within the experiment is controlled entirely by the remaining optical contribution. As detailed in Reference [82], the transition amplitudes describing an atom moving from the $|1, p\rangle$ state to the $|2, p + \hbar k\rangle$ and vice versa are given by

$$A_{12} = A_{21} = \frac{1}{\sqrt{2}} e^{-i(\vec{k}\cdot\vec{x} - \omega t)} \,, \tag{1.55}$$

where $\vec{k}$ is the photon wave-vector and ω its frequency. The pre-factor of $1/\sqrt{2}$ corresponds to a transition probability of 0.5 which can be achieved through tuning the duration and intensity of the laser pulses [83]. This dictates that the propagating photon imparts a phase change of $(\vec{k} \cdot \vec{x} - \omega t)$ upon absorption at position $\vec{x}$ and time t. Referring again to Figure 1.6, along each trajectory photon absorption occurs twice: once to transmit momentum to the atom and then once to subsequently remove it. Dependent on the path, this absorption takes place at different positions at different times. In addition, it follows from Equation (1.55) that only motion parallel to that of the photon propagation contributes to the optical phase difference. Through the aid of Figure 1.7, tracing these phase differences leads to the to a net photon contribution $\Delta^{(P)}$ of

$$\Delta^{(P)} = \Big\{ k(z_2 - z_1) - w(t_2 - t_1) \Big\} - \Big\{ k(z_3 - z_2) - w(t_3 - t_2) \Big\} \,, \tag{1.56}$$

where the two terms separate phase contributions from the two paths. The above assumes that photons are propagating entirely in the z direction. The indexed co-ordinates t_i and z_i correspond to the respective times and positions of the absorbing atom under a given light pulse i, where $i = 1, 2, 3$. In taking a uniform time separation T in between the light pulses, the temporal entries in Equation (1.56) exactly cancel. In the absence of any external acceleration, atomic trajectories are simply straight lines which leads to a vanishing contribution $\Delta^{(P)} = 0$. However, turning on a uniform acceleration field breaks the inherent symmetry of the experiment, where as a result atoms will fall three times as far during the second half of the experiment than the first. In this case, the two displacement terms can be written as

$$z_2 - z_1 = \Delta z - \frac{1}{2} a T^2 \,, \qquad\qquad z_3 - z_2 = \Delta z - \frac{3}{2} a T^2 \,, \tag{1.57}$$

where Δz corresponds to the displacement of the linear trajectory and a denotes the component of the acceleration parallel to the direction of photon propagation. Therefore, it follows that the contribution to the phase sourced by atom-photon interactions is given by

$$\Delta^{(P)} = k a T^2 \,. \tag{1.58}$$

In general, it is sufficient to assume a uniform field profile across the time and length scales of the experiment. As a result, the action contribution to the phase difference vanishes which implies that all of the phase difference information is programmed into the outcome of Equation (1.58).

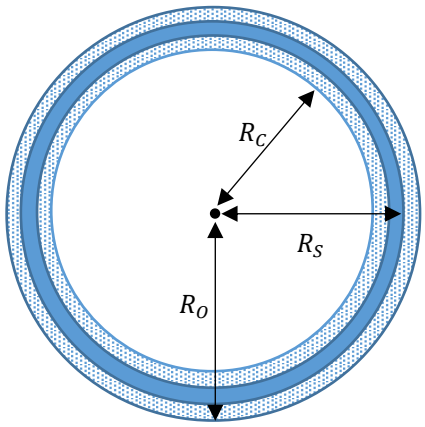

Figure 1.8: Illustration of the thin-shell effect present within the walls of a spherical vacuum chamber. The shaded regions correspond to the shell, with the solid band corresponding to the core for which the field lies at minima of the effective potential.

1.4.2 The Chameleon in a Spherical Vacuum Chamber

In practice, an atom interferometry experiment involves suspending a source object at the center of a vacuum chamber. Potentially harmful to the experimental procedure are the non-linear effects associated with the chamber itself, which can influence the system in a number of ways. The most immediate of these concerns is whether of not the chamber is sufficiently large to allow the chameleon field to relax into its equilibrium value. Recall that solving for the chameleon profile around a spherically symmetric source invoked the assumption that the exterior field approaching the source could be treated perturbatively around the background equilibrium value. However, if the specification of the chamber does not allow for this, then the external solution must be centred around another field value. For the case of a spherical vacuum chamber, this adjusted value can be calculated analytically, as detailed in Reference [64]. It turns out that the background field value $\phi^{(\mathrm{bg})}$ scales with chamber parameters as

$$\phi^{(\mathrm{bg})} = \begin{cases} \phi_{\mathrm{min}}^{(\mathrm{bg})} & \text{if } \; M^3\Lambda^5 \leq R_C^3\rho_{\mathrm{bg}} \\ \\ \left(8\Lambda^5 R_C^2/\pi^2\right)^{1/3} & \text{if } \; M^3\Lambda^5 > R_C^3\rho_{\mathrm{bg}}^3 \end{cases} , \tag{1.59}$$

with R_C and ρ_{bg} denoting the radius and density of the vacuum chamber respectively. Therefore, within a vacuum chamber, any solution obtained for the chameleon field profile around a spherical source object must be modified according to the above. External influences on the chameleon field can also potentially complicate matters here. If the walls of the chamber are sufficiently thick, the field has adequate space to respond to the change in the density field upon approaching from the outside. This acts as to effectively decouple the experimental system from any external influence, meaning that any environmental screening manifest

within the Earth's chameleon field is inconsequential. A calculation to verify this assumption was presented in Reference [64]. The idea was to prescribe the core-shell decomposition used when solving for a spherical source to the spherical vacuum chamber. The effective potential describing the immersing environment can then be built perturbatively around some background field value $\phi^{(\mathrm{E})}$. In light of this, the position of the outer core-shell interface within the vacuum chamber can be given by

$$R_S = R_O \sqrt{1 - \frac{2M}{\rho_{\mathrm{wall}} R_O^2} \phi^{(\mathrm{E})}} \,, \tag{1.60}$$

with R_O here corresponding to the outer radius of the vacuum chamber (incorporating the walls) and R_S is now the position of the outer shell; ρ_{wall} is the density of the vacuum chamber wall. The background field value $\phi^{(\mathrm{E})}$ in this case arises from the chameleon scalar interpolating between some surface value of the Earth, and the equilibrium value of the surrounding environment. To obtain an order of magnitude bound on the requirement for the lab to be decoupled from external influence, two approximations can be made. As the Earth is highly screened, one could argue that the background value satisfies $\phi^{(\mathrm{E})} \sim \phi^{(\mathrm{E})}_{\mathrm{min}}$ proximate to the Earth's surface, where $\phi^{(\mathrm{E})}_{\mathrm{min}}$ is the field value minimising the effective potential within the Earth. Additionally, the assumption can be made that $\rho_{\mathrm{wall}} \sim \rho_{\mathrm{E}}$. Effective decoupling requires that the recovered position for the outer core-shell radius falls within the walls of the vacuum chamber i.e. $R_S > R_C$. This way, the field reaches its equilibrium value within the walls of the chamber and thus external influences can be neglected. In introducing $\delta^{(t)}$ as the thickness of the chamber walls, one finds that

$$\delta^{(t)} \gtrsim \frac{\lambda_{\mathrm{bg}}^2}{R_C} \,, \tag{1.61}$$

where the compton wavelength of the field λ_{bg} has been introduced as the inverse mass m_{bg}^{-1}. The above also assumes that $\delta^{(t)} \ll R_S$. This is therefore a consistency requirement of Equation (1.61). Using this result, it turns out that for an interferometry experiment performed just below the meter scale, the above bound is comfortably satisfied across the parameter space. Thus, the screening due to the walls of the vacuum chamber prevents any external chameleon signals from influencing the interior solutions.

As a final point, it was noted in References [85] and [86] that above certain coupling strengths, the length scales of the chameleon become short enough that the chameleon field begins to respond to the molecular structure of the gas contained within the vacuum chamber. As a result, the chameleon field becomes heterogeneous as it can now resolve across the distance scales between the individual nuclei. However, these effects were shown [85] to only enter at very strong couplings $M/M_{\mathrm{PL}} \leq 10^{-8}$ so they can arguably be dismissed in an atom interferometry experiment aiming to probe weaker couplings of order $M/M_{\mathrm{PL}} \geq 10^{-5}$.

The subsequent chapters will now be devoted to the research conducted in an attempt to increase the constraining power of an atom interferometry experiment on the chameleon model. The choice to study the chameleon model in particular was partly to follow suit with

the ongoing research within the field, and in-part to do with the relative simplicity of the model: the symmetron for example has an additional free parameter, and calculations involving the dilaton field are much more involved from a mathematical standpoint. However as previously noted, the field profiles of all three models display very similar behaviour when considering a spherical source object, where all can be seen to exhibit a thin-shell mechanism [41]. Therefore, the hope is that the implications of this work on the chameleon field can be extended to the symmetron and dilaton fields, potentially motivating similar analyses to be performed for these models in the future.

Chapter 2

Ellipticity Weakens Chameleon Screening

In screened scalar field theories governed by the presence of non-linearities, it is natural to question whether the shape of the source object changes the efficiency of screening. Source shape dependence has been considered in Reference [93] for theories exhibiting Vainshtein screening, where the comparison of several sources (spherical, cylindrical and planar) showed a reduction in the effectiveness of the screening for the non-spherical geometries. In a cosmological setting, this motivates targeting searches for the Galileon field at matter morphologies such as walls or filaments.[1] The purpose of this chapter is to examine whether deforming the source object from a sphere to an ellipsoid generates any shape enhancements that heighten the detectability of a fifth force screened by the chameleon mechanism. Due to the complexity of the calculations, the analysis presented here will be restricted exclusively to the chameleon model although, as dilaton and symmetron models have very similar phenomenology to the chameleon for spherical sources, it is expected that the sensitivity of the chameleon to the shape of the source object derived in this article will extend to the dilaton and symmetron models as well. A related study has previously been performed for the chameleon in Reference [94] which exploits analogies between the chameleon field equations and equations in electrostatics to analyse the chameleon field around an ellipsoidal source. It should be noted however, that only the far field solution was presented in Reference [94] and that this does not hold in the regime of interest in this chapter, where a more complete treatment is required and presented.

This chapter will begin by recalling the theoretical structure of the chameleon, forming Section 2.1. This will then be followed by a review of the form of the gravitational field profile around an ellipsoidal source in Section 2.2. Section 2.3 then contains the derivation of the chameleon field profile around an ellipsoidal source. The findings of this work will then be concluded in Section 2.4 with a discussion of the implications of these results for the possibility of detecting the chameleon in a laboratory experiment. In the appendices, further details are given justifying various approximations made in the main body of the text.

[1] In contrast to the models previously mentioned, Vainshtein screening occurs in theories with non-linearities present in the kinetic terms.

2.1 The Chameleon Theory

The chameleon field is described by the following action:

$$\mathcal{S} = \int \mathrm{d}^4x\,\sqrt{-g}\left\{\frac{M_{\mathrm{PL}}^2}{2}R - \frac{1}{2}\partial_\mu\phi\partial^\mu\phi - V(\phi)\right\} + \int \mathrm{d}^4x\,\mathcal{L}_m\big(\psi_m, A^2(\phi)g_{\mu\nu}\big)\,, \tag{2.1}$$

where the chameleon field ϕ is minimally coupled to gravity and non-minimally coupled to matter. Here $M_{\mathrm{PL}}^2 = 1/(8\pi G)$ is the reduced Planck mass and $V(\phi)$ is the scalar potential. This simplified model assumes a universal minimal coupling between the conformally rescaled metric $\tilde{g}_{\mu\nu} = A^2(\phi)g_{\mu\nu}$ and each matter species, ψ_m. As noted in Section 1.3, we will always work in the regime $\phi \ll M$ which results in the conformal factor taking the linear form $A(\phi) = 1 + \frac{\phi}{M}$, where M denotes the coupling strength between the chameleon and matter. The density dependent behaviour of the chameleon requires that the chameleon potential $V(\phi)$ contains non-trivial self interaction terms. As mentioned in Section 1.3, the studies of the chameleon model presented here will work with the choice $V(\phi) = \frac{\Lambda^5}{\phi}$ for the self-interaction potential.

When the matter source is static and non-relativistic the chameleon field equation that results from the action in Equation (2.1) is

$$\nabla^2\phi = \frac{\partial V}{\partial\phi} + \rho\frac{\partial A}{\partial\phi}\,, \tag{2.2}$$

where ρ is the matter energy density. This indicates that the chameleon can be considered as a field moving in an effective potential:

$$V_{\mathrm{EFF}} = V(\phi) + \rho A(\phi)\,, \tag{2.3}$$

when ρ is assumed to be constant. The mass of the field follows by considering fluctuations around the vacuum state ϕ_{min}, such that $V'_{\mathrm{EFF}}(\phi_{\mathrm{min}}) = 0$:

$$m^2 = \frac{\partial^2 V_{\mathrm{EFF}}}{\partial\phi^2} = \frac{\partial^2 V}{\partial\phi^2} + \rho\frac{\partial^2\Omega}{\partial\phi^2}\,. \tag{2.4}$$

Substituting the choice of potential $V(\phi)$ and conformal factor $\Omega(\phi)$ described above, it follows that the position of the minimum of the effective potential and the mass of the chameleon field are

$$\phi_{\mathrm{min}} = \Big(\frac{\Lambda^5 M}{\rho}\Big)^{1/2}\,, \quad m^2 = 2\Big(\frac{\rho^3}{\Lambda^5 M^3}\Big)^{1/2}\,, \tag{2.5}$$

where it is evident that in regions of higher density the field value is smaller and the force has a shorter interaction range, due to a larger mass of the field and correspondingly reduced Compton wavelength.

The chameleon theory as introduced here does not solve the cosmological constant problem, a fine tuned constant term is required in the scalar potential if the chameleon is to drive

the acceleration of the expansion of the universe. Reconciling the chameleon with cosmological observations requires the mass of the field in the cosmological vacuum today to be of the order of the Hubble scale $m \simeq H_0$ [96, 97]. The chameleon model relies on the presence of non-linear terms in its potential, and therefore when considered as a quantum effective field theory non-renormalisible operators are inevitable. The theory is not protected from quantum corrections, and the scalar potential must be considered fine tuned, and therefore the theory should only be treated as a low energy effective theory. These quantum corrections can become important in laboratory searches, and in the early universe [26, 98, 99]. It is acknowledged that this fine tuning is a potential issue for chameleon theories but to attempt to solve this problem is beyond the scope of this work. Moreover this work is primarily aimed at demonstrating the more general point that density dependent couplings of scalar fields could well be detected within laboratory experiments, and that the strength of the force is sensitive to the shape of the source.

2.2 Gravity around an Ellipsoidal Source

Before turning to the chameleon, it proves useful to first review the Newtonian gravitational field profile surrounding an ellipsoidal source. The following analysis of ellipsoidal geometries involves the use of spherical prolate coordinates which are discussed in more detail in Appendix 2.A. Spherical prolate and Cartesian co-ordinates are related via the following transformations:

$$\begin{aligned} x &= a\sqrt{(\xi^2-1)(1-\eta^2)}\,\cos(\phi)\,, \\ y &= a\sqrt{(\xi^2-1)(1-\eta^2)}\,\sin(\phi)\,, \\ z &= a\xi\eta\,, \end{aligned} \tag{2.6}$$

and are defined such that the major axis of the ellipse lies along the z-direction with foci at $z = \pm a$. The co-ordinate ϕ represents the conventional azimuthal angle appearing in spherical polar co-ordinates whereas ξ and η are analogous to the radial and polar angular components respectively. The coordinate ranges are $+1 < \xi < \infty$, $-1 < \eta < +1$ and $0 < \phi < 2\pi$. The only dimensionful parameter entering the coordinate system is the focal length a which controls the size of the ellipsoid. The gravitational potential, Φ, is governed by Poisson's equation:

$$\nabla^2\Phi = -\frac{\rho}{2M_{\rm PL}^2}\,. \tag{2.7}$$

To determine the gravitational field profile around a compact ellipsoidal source of constant density, $\rho_{\rm obj}$, contained within $1 \leq \xi \leq \xi_0$, and embedded in a zero density background, the following system of equations must be solved:

$$\nabla^2\Phi = 0\,, \qquad \text{for } \xi_0 \leq \xi < \infty\,, \tag{2.8}$$

$$\nabla^2\Phi = -\frac{\rho_{\rm obj}}{2M_{\rm PL}^2}\,, \qquad \text{for } 1 \leq \xi \leq \xi_0\,. \tag{2.9}$$

The shape parameter describing the source ξ_0 may be related to other common ellipsoidal parametrisations such as the ellipticity e and the compression factor ζ via the following

relations:

$$e = \frac{1}{\xi_0}, \qquad \zeta = \frac{\sqrt{\xi_0^2 - 1}}{\xi_0} \,, \tag{2.10}$$

where a smaller value of ξ_0 reflects a lower compression factor or equivalently a higher ellipticity. Finding the complete solution to the boundary value problem of Equation (2.8) involves imposing boundary conditions such that Φ and $\nabla\Phi$ are continuous at $\xi = \xi_0$, that Φ decays as $\xi \to \infty$ and is regular at $\xi = 1$. This problem admits a separable homogeneous solution of the form $\Phi = \tilde{\Phi}(\phi)\sum_{l=0}^{\infty} X_l(\xi)H_l(\eta)$, which pairs the η and ξ dependent factors as a sum over an orthonormal set of basis functions. As the system under consideration has azimuthal symmetry, it is possible to make the simplifying assumption that Φ is independent of ϕ, and thus $\tilde{\Phi}$ is constant. Outside of the source, $\xi \geq \xi_0$, the Laplace equation

$$\frac{(\xi^2-1)(1-\eta^2)}{(\xi^2-\eta^2)}\left\{\frac{1}{X_l(\xi)}\frac{\partial}{\partial\xi}(\xi^2-1)\frac{\partial X_l(\xi)}{\partial\xi} + \frac{1}{H_l(\eta)}\frac{\partial}{\partial\eta}(1-\eta^2)\frac{\partial H_l(\eta)}{\partial\eta}\right\} = 0 \,, \tag{2.11}$$

can be separated into two copies of Legendre's equation:

$$\frac{\partial}{\partial\xi}(\xi^2-1)\frac{\partial X_l(\xi)}{\partial\xi} - \lambda_l X_l(\xi) = 0 \,, \tag{2.12a}$$

$$\frac{\partial}{\partial\eta}(1-\eta^2)\frac{\partial H_l(\eta)}{\partial\eta} + \lambda_l H_l(\eta) = 0 \,, \tag{2.12b}$$

where λ_l is a separation constant. As is shown in Equation (2.89) of Appendix 2.B, this leads to the specific relation $\lambda_l = l(l+1)$ for any non-negative integer l. This has the effect of reducing these equations to Legendre form. The corresponding Legendre functions of the first kind $P_l(x)$ are defined on the interval $(-\infty, \infty)$, whereas those of the second kind $Q_l(x)$ are defined on the interval $(1, \infty]$. It means therefore that solutions to the ξ equation above can be Legendre functions of either the first or second kind, whereas solutions to the η equation can only be Legendre functions of the first kind. The full solution for Φ in the exterior of the source is a linear combination of these Legendre functions:

$$\Phi = \sum_{l=0}^{\infty} A_l P_l(\eta)P_l(\xi) + B_l P_l(\eta)Q_l(\xi) \,, \qquad \text{for } \xi \geq \xi_0 \,, \tag{2.13}$$

where A_l and B_l are l-dependent constants. The first term in this expression diverges as $\xi \to \infty$, this requires setting $A_l = 0$ in order to ensure that the field decays at infinity. It remains to determine the form of Φ in the interior of the source. This can be written as the sum of a homogeneous solution of the form given in Equation (2.13) and a particular integral, $\Phi_{\rm PI}$ that takes the form

$$\Phi_{\rm PI} = -\frac{\rho_{\rm obj}a^2}{8M_{\rm Pl}^2}\big(\xi^2-1\big)\big(1-\eta^2\big) \equiv -\frac{\rho_{\rm obj}a^2}{12M_{\rm PL}^2}(\xi^2-1)\big[P_0(\eta) - P_2(\eta)\big] \,. \tag{2.14}$$

Imposing that the solution does not diverge at the centre of the source, $\xi = 1$, the full interior solution can be written as

$$\Phi = \sum_{l=0}^{\infty} C_l P_l(\eta)P_l(\xi) - \frac{\rho_{\rm obj}a^2}{12M_{\rm PL}^2}(\xi^2-1)\big[P_0(\eta) - P_2(\eta)\big] \,, \qquad 1 < \xi \leq \xi_0 \,. \tag{2.15}$$

The surviving unknowns B_l and C_l are identified by imposing the remaining boundary conditions that ensure that the field and its first derivatives are continuous across the surface of the object at ξ_0. This leads to the final solution for the form of the gravitational field profile for an ellipsoidal source:

$$\Phi = \frac{M_{\rm obj}}{8\pi M_{\rm PL}^2 a} \begin{cases} Q_0(\xi) - P_2(\eta)Q_2(\xi) \ , & \xi > \xi_0 \\ Q_0(\xi_0)[1 - P_2(\eta)P_2(\xi)] & 1 < \xi \leq \xi_0 \\ + \frac{1}{\xi_0(2P_2(\xi_0)+1)} \{P_2(\xi_0) - P_2(\xi) + 2P_2(\eta)P_2(\xi) & \\ + 2P_2(\eta)P_2(\xi)[1 + P_2(\xi_0)]\} & \end{cases} , \tag{2.16}$$

where $M_{\rm obj}$ is the mass of the source.

2.3 The Chameleon Profile Around an Ellipsoidal Source

To find the chameleon field profile around an ellipsoidal source, one follows a very similar procedure to that taken to solve the gravitational equations in the previous section. The main differences arise when considering the form of the chameleon field profile in the interior of the source. As illustrated in Figure 2.1, it is expected that an ellipsoidal source will give rise to similar chameleon behaviour to that due to a spherical object, meaning that a sufficiently large source will form a 'thin-shell'. This occurs when the chameleon field reaches the field value that minimises the effective potential in the interior of the source. Due to the large mass of fluctuations around this value, the field is unable to move from this minimum and remains stuck at this value for almost the whole of the interior of the object, it only changes its value in a thin-shell near the surface [60]. This same behaviour is expected for an ellipsoidal source, with the difference that the thin shell is defined by two ellipsoids.[2] This decomposition of the solution is illustrated in Figure 2.1. As for spherical objects, a core region where the field reaches the minimum of the effective potential may not exist. If it is absent the object is referred to as 'thick-shell' and the field profile just takes the form of a standard Yukawa force law. If the mass of the field is negligible this is exactly analogous to the gravitational potential (with the possibility of a different coupling constant) determined in the previous section, because the field never reaches the non-linear region of the chameleon potential. As for the case of the sphere, solutions can be constructed by assuming that a core region exists. The criteria allowing for the formation (or disappearance) of the core region can then be evaluated once the full solution is obtained. Thus, analogous to the spherical scenario, the chameleon field equations can be broken down in the following way:

$$\begin{aligned} \nabla^2\phi &= m_{\rm bg}^2(\phi - \phi_{\rm min}^{\rm (bg)}) \ , & \xi_0 \leq &\xi < \infty \ , \\ \nabla^2\phi &= \frac{\rho_{\rm obj}}{M} \ , & \xi_{\rm core} \leq &\xi \leq \xi_0 \ , \\ \nabla^2\phi &= m_{\rm obj}^2(\phi - \phi_{\rm min}^{\rm (obj)}) \ , & 1 \leq &\xi \leq \xi_{\rm core} \ , \end{aligned} \tag{2.17}$$

[2] This is to say that the inner and outer surfaces are parametrised with different ellipcities

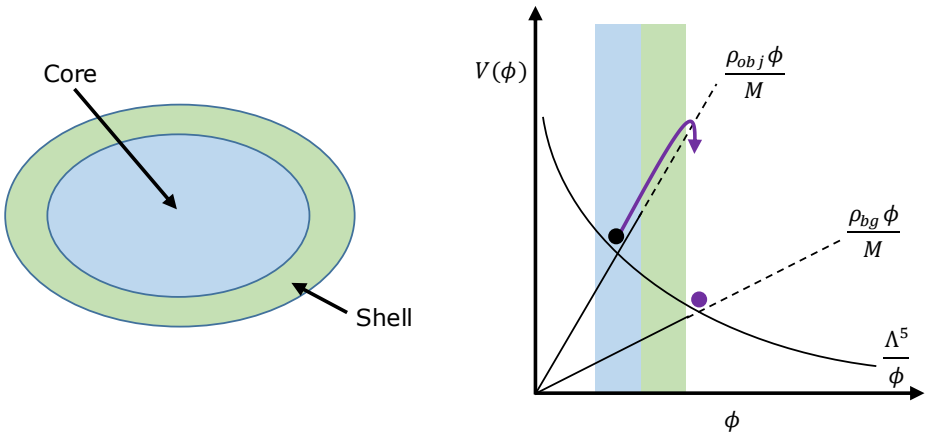

Figure 2.1: The chameleon field profile decomposes into core, shell and exterior regions. The relevant regime within the potential is indicated for each of the three regions.

where $\phi_{\rm min}^{\rm (bg)}$ and $m_{\rm bg}$ are the field value and mass at the minimum of the effective potential in the background of the experiment, where the density is assumed to be $\rho_{\rm bg}$, whilst $\phi_{\rm min}^{\rm (obj)}$ and $m_{\rm obj}$ are the equivalent values in the interior of the source, which has density $\rho_{\rm obj}$.

In what follows it will be argued that the mass of the chameleon can always be neglected when studying the behaviour of the field close to the source. At distances far from the source, the Yukawa suppression becomes important and the mass of the field plays an important role in determining when this occurs. Closer to the source the important dimensionless (in natural units) combination of parameters is ma; the mass of the chameleon multiplied by the focal length of the ellipse. Within the available chameleon parameter space and considering values for the size and mass of the source object suitable for laboratory experiments the combination ma is always small, and therefore the mass of the chameleon can be safely neglected in the analysis that follows. In Appendix 2.B this approximation is explored in more detail which involves computing the first order corrections in ma to the massless solution. The procedure presented closely follows previous work deriving ellipsoidal solutions to the Helmholtz equation in [100–103].

Neglecting the masses of the chameleon in Equation (2.17) reduces them to the forms of the Laplace and Poisson equations, solved for the gravitational case in the previous section. The chameleon thin-shell solution only differs from the gravitational solution by the existence of the core region. However, as for the gravitational scenario, it required that the field must decay at infinity, be regular at the centre of the ellipsoid, $\xi = 1$, and that the field and its first derivative are continuous at the surface of the source and at the surface of the core region, $\xi_{\rm core}$. The position of the surface of the core will be determined from these boundary

conditions. Therefore the solution has the form

$$\phi = \sum_{l=0}^{\infty} V_l P_l(\eta) P_l(\xi) + \phi_{\rm min}^{\rm (obj)} \ , \qquad 1 \leq \xi \leq \xi_{\rm core} \ ,$$

(2.18a)

$$\phi = \sum_{l=0}^{\infty} \Big(C_l P_l(\eta) P_l(\xi) + D_l P_l(\eta) Q_l(\xi) \Big) - \frac{1}{6} \frac{\rho_{\rm obj}}{M} (\xi^2 - 1) \Big[P_0(\eta) - P_2(\eta) \Big] \ , \quad \xi_{\rm core} \leq \xi \leq \xi_0 \ ,$$

(2.18b)

$$\phi = \sum_{l=0}^{\infty} W_l P_l(\eta) Q_l(\xi) + \phi_{\rm min}^{\rm (bg)} \ , \qquad \xi_0 \leq \xi \leq \infty \ .$$

(2.18c)

The determination of the remaining unknowns, V_l, C_l, D_l, W_l and $\xi_{\rm core}$ requires imposing the continuity of ϕ, and $\partial\phi/\partial\xi$ across the two surfaces at ξ_0 and $\xi_{\rm core}$.[3] Importantly, these boundary conditions must apply for all η, thus the boundary conditions are imposed separately for each P_l. For example continuity of ϕ at $\xi_{\rm core}$ requires

$$\phi_{\rm min}^{\rm (obj)} = C_0 + D_0 Q_0(\xi_{\rm core}) - \frac{1}{6} \frac{\rho_{\rm obj}}{M} (\xi_{\rm core}^2 - 1) \ , \tag{2.19a}$$

$$V_2 P_2(\xi_{\rm core}) = C_2 P_2(\xi_{\rm core}) + D_2 Q_2(\xi_{\rm core}) + \frac{1}{6} \frac{\rho_{\rm obj}}{M} (\xi_{\rm core}^2 - 1) \ , \tag{2.19b}$$

$$V_l P_l(\xi_{\rm core}) = C_l P_l(\xi_{\rm core}) + D_l Q_l(\xi_{\rm core}) \ , \qquad l = 1, 3, 4, 5, \ldots \ . \tag{2.19c}$$

After applying all of the above boundary conditions the final form of the chameleon field (to all orders in l) in the exterior of an ellipsoidal source is

$$\phi = \frac{1}{2} \frac{\rho_{\rm obj} a^2}{3M} \Big\{ \xi_0 (\xi_0^2 - 1) - \xi_{\rm core} (\xi_{\rm core}^2 - 1) \Big\} \Big(Q_0(\xi) - P_2(\eta) Q_2(\xi) \Big) + \phi_{\rm min}^{\rm (bg)} \ , \tag{2.20}$$

for $\xi_0 \leq \xi < \infty$ and the position of the surface of the core, $\xi_{\rm core}$, is given implicitly by the expression

$$\frac{6}{\rho_{\rm obj} a^2} \left(\frac{M^3 \Lambda^5}{\rho_{\rm bg}} \right)^{1/2} + (\xi_{\rm core}^2 - 1) \Big\{ 1 + 2 \xi_{\rm core} Q_0(\xi_{\rm core}) \Big\} = (\xi_0^2 - 1) \Big\{ 1 + 2 \xi_0 Q_0(\xi_0) \Big\} \ . \tag{2.21}$$

These results differ from the results presented in Reference [94] due to the appearance of the quadrupole term $P_2(\eta)$ in Equation (2.20), which is included in the analysis presented here but was neglected in previous work. As a result, the solutions presented here do not lead to the enhancement of the field at the 'tips' of the ellipsoid that was suggested in Reference

[3] Note that the values of the constants C_l do not take the same values as the constants found in the gravitational case in the previous section.

[94]. The thin shell solution holds whenever there is a solution to Equation (2.21) which gives a real and strictly positive value for $\xi_{\rm core}$. This is difficult to determine analytically, but is straightforward to do numerically. The implications of these solutions will be investigated in the following section. For a sufficiently thin shell ($\xi_0 - \xi_{\rm core} \ll 1$), an analytic expression for the position of the interior surface of the shell can be found by manipulating Equation (2.21):

$$\xi_0 - \xi_{\rm core} = \frac{6}{\rho_{\rm obj} a^2}\left(\frac{M^3\Lambda^5}{\rho_{\rm bg}}\right)^{\frac{1}{2}} \frac{1}{(3\xi_0^2 - 1)Q_0(\xi_0)} \ . \tag{2.22}$$

As a consistency check of this result, one can verify that this expression recovers the familiar expression for the thin shell of a sphere upon taking the spherical limit $\xi_0 \to \infty$, with a fixed. For large ξ the Legendre function of the second kind becomes $Q_0(\xi) = 1/2\xi$, to first order. For objects that retain a thin shell as they are deformed from an ellipsoid to a sphere, it can be assumed that both ξ_0 and the shell position $\xi_{\rm core}$ are large. Equation (2.22) then becomes

$$\frac{6M}{3\rho_{\rm obj} a^2}\phi_{\rm min}^{\rm (obj)} = \xi_0^2 - \xi_{\rm core}^2 \ , \tag{2.23}$$

where it has been assumed that $\phi_{\rm min}^{\rm (obj)} \ll \phi_{\rm min}^{\rm (bg)}$, which is valid as long as $\rho_{\rm obj} \gg \rho_{\rm bg}$. At large ξ the ellipsoidal coordinate ξ can be related to the radial coordinate in spherical polars by $\xi = r/a$ (this is derived in Appendix 2.C). Hence, identifying $\xi_{\rm core}^2 = S^2/a^2$ and $\xi_0^2 = R^2/a^2$ leads to

$$S^2 = R^2 - \frac{2M}{\rho_{\rm obj}}\phi_{\rm min}^{\rm (obj)} \ , \tag{2.24}$$

which is the familiar expression for the thin shell of a sphere first derived in Reference [60].

2.4 Comparisons to Gravity

The intention of this work is to determine whether or not ellipsoidal deformations impact on the efficiency of chameleon screening, and as a result, the detectability of the chameleon. The chameleon force on a test particle due to the ellipsoidal source can be found from the chameleon potential derived in the previous section as $\vec{F}_\phi = -\vec{\nabla}\phi/M$. Outside of the source, $\xi > \xi_0$, the chameleon and gravitational potentials have been identified to obey the same functional form. Therefore, the ratio of the corresponding forces is a constant independent of the coordinates:

$$\frac{F_\phi}{F_G} = 2\left(\frac{M_{\rm PL}}{M}\right)^2\left\{1 - \frac{\xi_{\rm core}(\xi_{\rm core}^2 - 1)}{\xi_0(\xi_0^2 - 1)}\right\} \ . \tag{2.25}$$

As expected the chameleon force is maximised when there is no core region in the interior, $\xi_{\rm core} = 1$, and in this case if M is chosen to lie at the Planck scale, the chameleon force is twice the gravitational force. Once a core region develops the chameleon force is suppressed, this is the essence of chameleon screening, and this behaviour can be clearly seen in Figure 2.2. To determine how changing the shape of a source affects the screening, the mass of the object will be fixed such that only the effect of deformations are being considered. Assuming a fixed uniform density for the interior across the ellipsoidal and spherical sources, the size of any given ellipsoid can be referred to in terms of the parameter $R_{\rm EFF}$ which is the

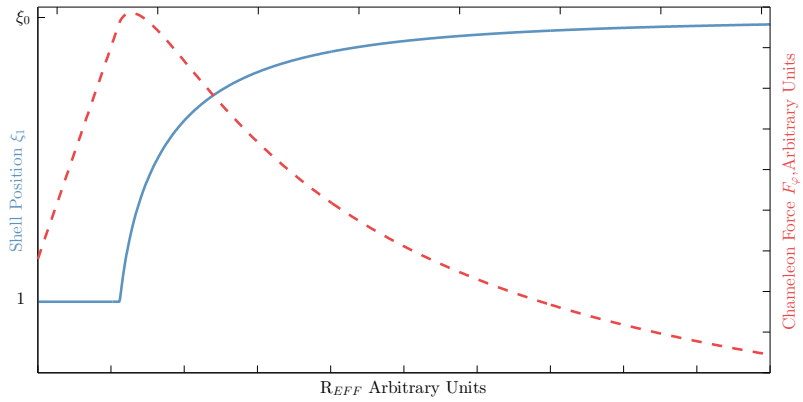

Figure 2.2: The blue line represents the scaling of the relative size of the shell region within an ellipsoidal source of size $R_{\rm EFF}$. At the far left, a constant value is approached as the shell solution pervades the entire object and the core region is absent. As the effective radius is increased, the extent of the shell region begins to diminish due to the emergence of a core region. The dotted red line shows the corresponding dependence of the magnitude of the chameleon force sourced by the compact object. The maximum force magnitude occurs when the radius of the source corresponds to the formation of a core region.

radius of a sphere of the same mass, $R_{\rm EFF} = a(\xi_0(\xi_0^2 - 1))^{1/3}$, this expression is derived in Appendix 2.C, Equation (2.116). Unless noted otherwise, any figures quoted have been obtained by taking the source object and background densities to be 1 gcm^{-3} and 10^{-17} gcm^{-3} respectively, which are appropriate values for laboratory experiments. Due to the nature of prolate spheroidal coordinates, variations in the ellipsoidal structure are most sensitive at low ξ, whilst the value of $\xi_0 = 5$ is visually almost indistinguishable from a perfect sphere. Accordingly, we take $\xi_0 = 5$ to represent the spherical limit. Figure 2.3a shows the shape dependence of both the gravitational force and the chameleon force for a source exhibiting screening, due to the formation of a core region. It is clear from Figure 2.3 that whilst the shape of the chameleon profile is the same as the shape of the gravitational profile for each ellipsoid, the ratio of the chameleon to gravitational force increases as the source becomes more ellipsoidal. This can be attributed to the ellipsoidal source favouring a comparatively smaller core component, resulting in less effective screening. Such behaviour is displayed in Figure 2.4 which shows how the volume of the core scales with the compression of an object. As the internal chameleon structure responds to deformations by reducing the core region, there will be some threshold ellipticity where screening is deactivated, as the core vanishes. It follows that the onset of forming a shell is delayed as the source becomes more ellipsoidal, as can be seen from Figure 2.5. This figure shows the ratio of the chameleon and gravitational forces for different sized objects with different ellipticities. For ease of comparison, the specific choice $M = M_{\rm PL}$ was taken in order to generate this figure, but the shape dependence of the effect is independent of the choice of M. When $F_\phi/F_G = 2$ there is no thin shell and the chameleon force is unscreened. As the size of the source is increased, as parameterised by the effective radius $R_{\rm EFF}$, a thin shell develops and the chameleon force

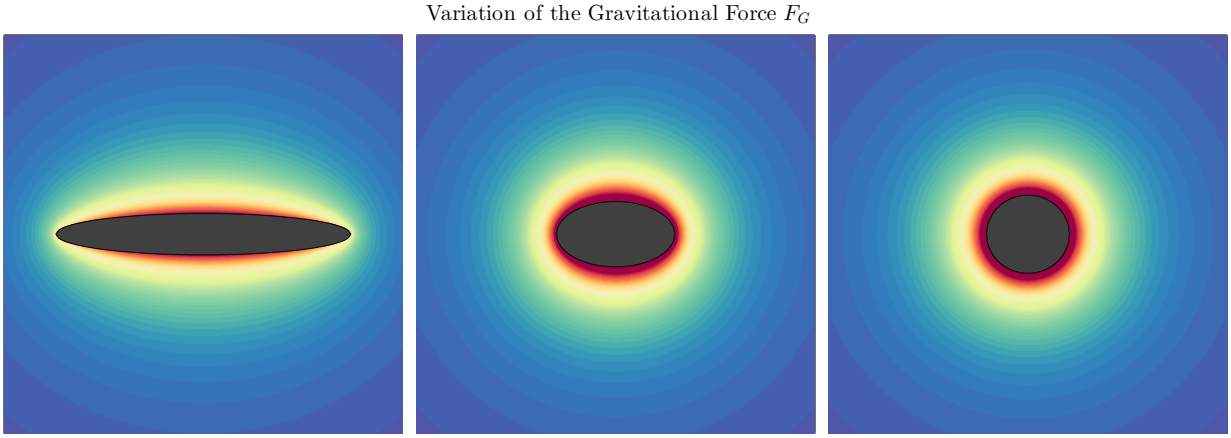

(a) The shape dependence of the gravitational force. This also represents the shape dependence of the unscreened chameleon force around objects that do not have a thin shell.

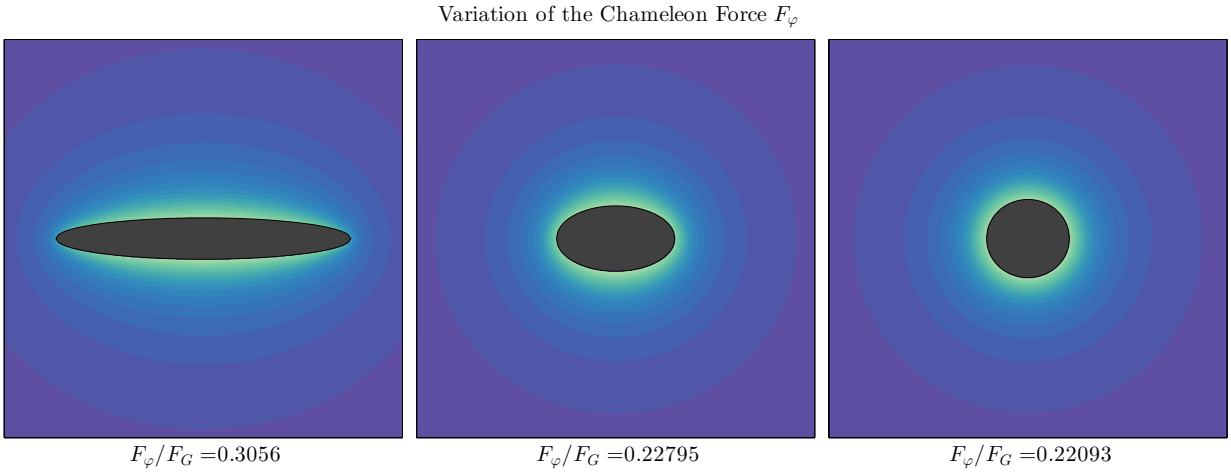

(b) The shape dependence of the chameleon force characteristic of objects for which a shell region has developed.

Figure 2.3: Comparison of the shape dependence of the gravitational and chameleon force. The mass of the source, represented by the black region, is the same for all plots. From left to right the ellipsoids have $\xi_0 = 1.01$, $\xi_0 = 1.1$ and $\xi_0 = 5$ in both subfigures, corresponding to ellipticities ~ 0.99, 0.91 and 0.2 respectively. The colours indicate the strength of the force, with red indicating regions of strongest force and blue indicating regions of weakest force. The colour spectrum across these images has been normalised to the same limits to highlight the chameleons relative contribution. Increasing the ellipticity of the source can be seen to increase the ratio between the chameleon and the gravitational interactions. The parameter values $\Lambda = 10^{-12}$ GeV and $M = 0.5M_{\rm PL}$ were chosen to generate these plots, but the shape dependence is independent of these choices.

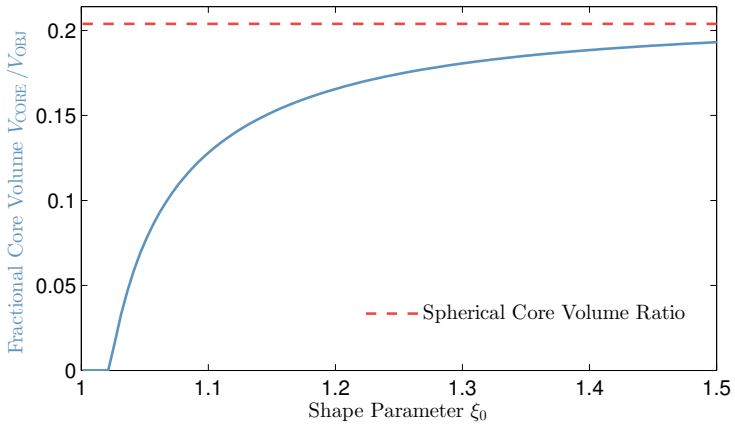

Figure 2.4: Example of how the size of the core region decays as the ellipticity of the source object increases (lower ξ_0). The line asymptotes to the core volume for the spherical scenario as $\xi_0 \to \infty$, represented by the red dashed line. This figure was generated for an object of size $R_{\rm EFF} = 4$m as this value captures the whole range of scaling effects. M and Λ were set as $M_{\rm PL}$ and 10^{-12} GeV respectively.

is suppressed. Figure 2.5 shows that this occurs for larger $R_{\rm EFF}$ when the source is more ellipsoidal, or equivalently has a smaller ξ_0. This figure also demonstrates that the shape enhancement persists as the size of the source is increased. A closer inspection of the data used to generate Figure 2.5 approximates that the impact of deforming a sphere to an ellipsoid of $\xi_0 = 1.01$ is to enhance the chameleon force by as much as 40%. The difficulty in determining $\xi_{\rm core}$ analytically, makes it difficult to determine whether there is a maximum shape enhancement possible, or whether it continues to increase as the source is made more ellipsoidal. However, as there is a limit to the ellipticity of an object that can be created, the behaviour of the shape enhancement as the ellipticity is increased much beyond the values considered here is not relevant for any realistic experimental scenario.

Current experimental constraints on the chameleon from Casimir experiments, atomic spectroscopy and torsion balance tests of gravity [75, 104–106] restrict the chameleon parameters to lie in the ranges $\Lambda \leq 10^{-10}$ GeV and 10^4 GeV $\leq M \leq M_{\rm PL}$. The values of Λ that were studied here were confined to the range 10^{-14} GeV $\leq \Lambda \leq 10^{-10}$ GeV as chameleon theories that can be connected to the dark energy scale with $\Lambda \sim 10^{-12}$ GeV are of most interest. Varying these parameters varies the size of object which forms a thin shell, as shown in Figure 2.6.

Figure 2.6 also shows how the onset of screening varies with the background density $\rho_{\rm bg}$. As the density of the environment is decreased the magnitude of the shape enhancement is seen to increase, as shown by the widths of the coloured bands. Laboratory experiments searching for the chameleon can be made more sensitive if the background density is decreased, this increases the value of $\phi_{\rm bg}$ and makes the chameleon field harder to screen.

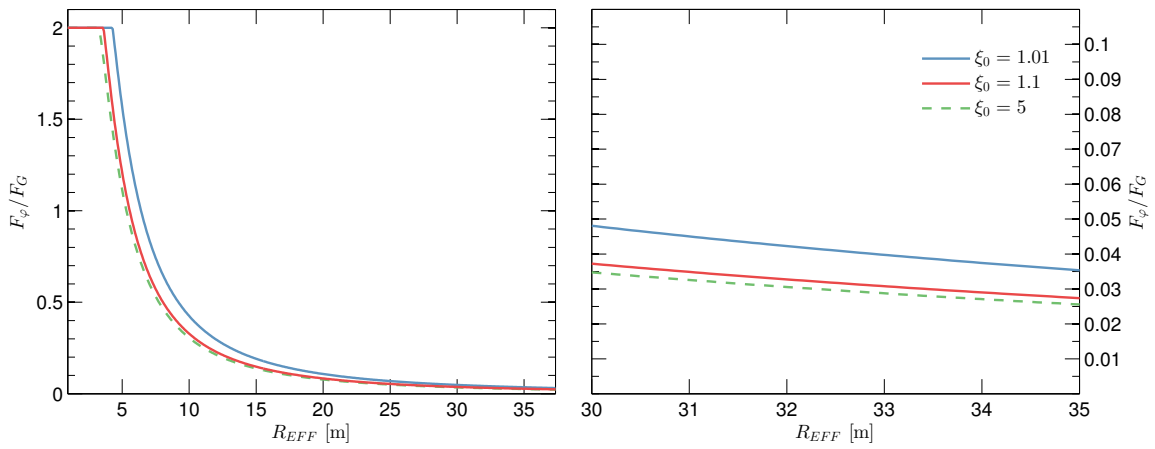

Figure 2.5: The ratio of the chameleon to gravitational forces as a function of the size of the source mass, parameterised by the radius of a sphere of equal mass $R_{\rm EFF}$. The different lines show sources of different ellipticities, with the green line being the most spherical and the blue line the most ellipsoidal. The right hand plot is a magnification of a region of the left hand plot to show that the shape enhancement of the chameleon force persists as the size of the source is increased. To obtain numerical values the parameters were chosen to be $\rho_{\rm obj} = 10^3$ kgm^{-3}, $\rho_{\rm bg} = 10^{-14}$ kgm^{-3}, $M = M_{\rm PL}$, and Λ set at the dark energy scale 10^{-12} GeV

However creating increasingly more diffuse vacuums is a difficult task. We have shown here that increasing the ellipticity of the source can increase the chameleon field strength in a similar manner to decreasing the density of the vacuum within which the experiment is performed. Changing the shape of the source is an easier technical challenge than decreasing the density of the vacuum chamber and could therefore be used to increase the sensitivity of current proposals to detect the chameleon field, including that of Reference [64]. Comparison between the two plots in Figure 2.6 shows how varying Λ changes the size of the source for which a thin shell first forms. This allows any laboratory experiment to increase the range of its sensitivity to Λ by searching for the chameleon around both spherical and ellipsoidal sources. In principle, one could tune the size and shape of the chameleon source as to exploit this enhancement to maximise the detectability of a given point in the chameleon parameter space. As the value of Λ is increased the difference between the chameleon field around an ellipsoidal and a spherical source decreases. The available chameleon parameter space is shown in Figure 2.7. The left hand plot shows the ratio of the chameleon to gravitational forces for a sphere in a laboratory scenario chosen to correspond to that of the experiment proposed in Reference [64]. The right hand plot shows the large region of parameter space in which the chameleon force can be enhanced by changing from a spherical to an ellipsoidal source.

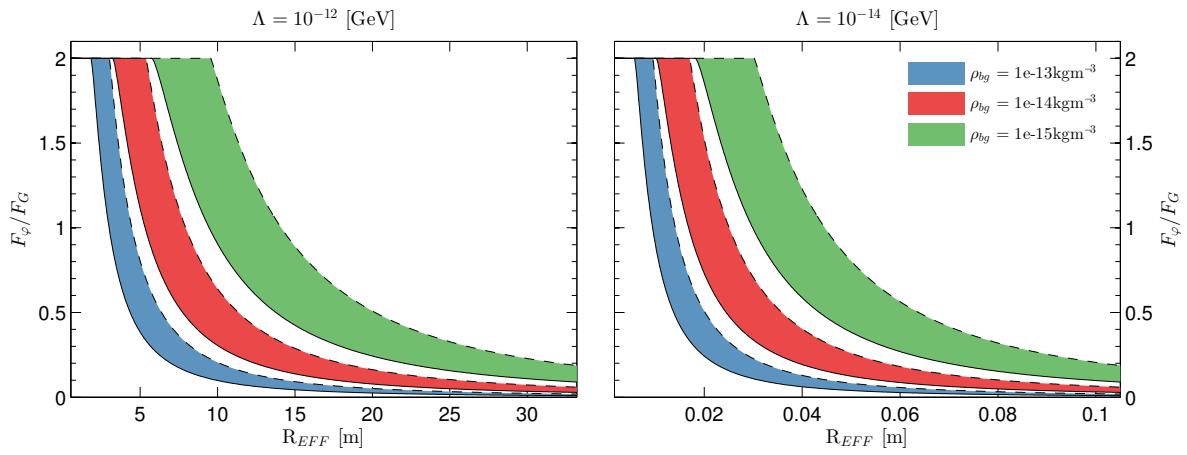

Figure 2.6: The ratio of the chameleon to gravitational force as a function of the size of the source for different choices of Λ and $\rho_{\rm bg}$. The lower edge of each band, drawn with a solid line, shows the force ratio for a spherical source. The upper edge of each band, drawn with a dashed line, shows the force ratio for an ellipsoid with $\xi_0 = 1.001$.

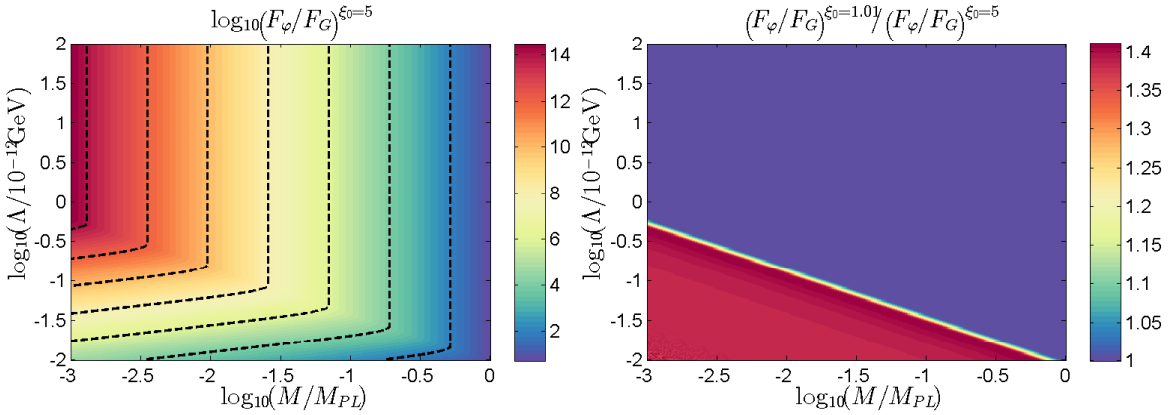

Figure 2.7: Left: The ratio of the chameleon to gravitational forces as a function of the parameters Λ and M for a spherical source object with $R_{\rm EFF} = 1$ cm. The ambient and source densities take our reference values, 1 gcm^{-3} and 10^{-17} gcm^{-3}. Right: The enhancement of the chameleon force when an ellipsoid with $\xi_0 = 1.01$ is compared to a sphere.

2.5 Conclusions

The work presented in this chapter has demonstrated that increasing the ellipticity of a source, whilst keeping the density and mass of the source fixed, increases the ratio of the screened chameleon to gravitational forces. This is not necessarily because the chameleon

force gets stronger but instead the because gravitational force suffers far more from the deformation. This behaviour is illustrated in Figure 2.3. Thus when performing an experiment to search for a chameleon, replacing a spherical source with an ellipsoid of identical mass enhances the effects of the chameleon when compared to gravity thereby increasing the sensitivity of the experiment. For realistic choices of parameters, moving to an ellipsoidal source finds enhancements of the chameleon force by up to 40%. It has also been outlined that for a sufficiently flattened disk, the shape enhancement effects emulate reducing the density of the lab vacuum by up to an order of magnitude. Thus, to increase chances of detection, changing the geometry of the source can be used as a cost effective alternative to lowering the ambient density.

The central message here is that when considering the effects of fifth forces which possess screening mechanisms, the effects of the force can be underestimated if only spherical sources are considered, and that the strength of the force can vary significantly with the shape of the source. Ellipsoidal sources can be studied analytically and so are a useful test bed in which to study these effects. However, the promising results gathered for the ellipsoid make the idea of geometric enhancements of the chameleon field an interesting topic to pursue. This leads naturally on to the work presented in Chapter 3, which studies these effects for a broader range of source objects.

As a final note, the calculations presented here have neglected the effects arising due to the finite size of the vacuum chamber, as discussed in Chapter 1. In particular, the supposition has been made that the vacuum chamber is sufficiently large such as to allow the chameleon value to reach its equilibrium value. In practice this condition is not met when constructing a vacuum chamber following the specification of that in Reference [64]. This acts to shift the background field to a lower value forces the development a larger core region thus magnifying the screening effect. This however, is a systematic adjustment which in principle shouldn't threaten the implications of this work, as the chameleon interactions appearing in the spherical scenario are compromised in the same fashion.

2.A Spherical Prolate Coordinates

The appropriate coordinate system to describe ellipsoidal geometries is prolate spheroidal coordinates. As described in the text, these are defined such that the major axis of the ellipse lies along z with foci at $z = \pm a$. They relate to Cartesian co-ordinates via the following transformations:

$$\begin{aligned} x &= a\sqrt{(\xi^2-1)(1-\eta^2)}\,\cos(\varphi)\,, \\ y &= a\sqrt{(\xi^2-1)(1-\eta^2)}\,\sin(\varphi)\,, \\ z &= a\xi\eta\,. \end{aligned} \tag{2.26}$$

The co-ordinate φ represents the conventional azimuthal angle appearing in spherical polar co-ordinates whereas ξ and η are analogous to the radial and polar angular components respectively, with $+1 < \xi < \infty$, $-1 < \eta < +1$ and $0 < \phi < 2\pi$. This allows for the calculation of the associated scale factors:

$$\begin{aligned} h_\xi &= \sqrt{\left(\frac{\partial x}{\partial \xi}\right)^2 + \left(\frac{\partial y}{\partial \xi}\right)^2 + \left(\frac{\partial z}{\partial \xi}\right)^2} = a\sqrt{\frac{\xi^2-\eta^2}{\xi^2-1}}\,, \\ h_\eta &= \sqrt{\left(\frac{\partial x}{\partial \eta}\right)^2 + \left(\frac{\partial y}{\partial \eta}\right)^2 + \left(\frac{\partial z}{\partial \eta}\right)^2} = a\sqrt{\frac{\xi^2-\eta^2}{1-\eta^2}}\,, \\ h_\varphi &= \sqrt{\left(\frac{\partial x}{\partial \varphi}\right)^2 + \left(\frac{\partial y}{\partial \varphi}\right)^2 + \left(\frac{\partial z}{\partial \varphi}\right)^2} = a\sqrt{(\xi^2-1)(1-\eta^2)}\,, \end{aligned} \tag{2.27}$$

which can be used to determine the form of the Laplacian in prolate spheroidal coordinates:

$$\nabla^2\phi = \frac{1}{h_\xi h_\eta h_\varphi}\sum_{i=1}^{3}\frac{\partial}{\partial \xi_i}\frac{h_\xi h_\eta h_\varphi}{h_i^2}\frac{\partial \phi}{\partial \xi_i}\,, \tag{2.28}$$

$$= \frac{1}{a^2(\xi^2-\eta^2)}\left\{\frac{\partial}{\partial \xi}(\xi^2-1)\frac{\partial \phi}{\partial \xi} + \frac{\partial}{\partial \eta}(1-\eta^2)\frac{\partial \phi}{\partial \eta} + \frac{\xi^2-\eta^2}{(\xi^2-1)(1-\eta^2)}\frac{\partial^2\phi}{\partial \varphi^2}\right\}\,. \tag{2.29}$$

2.B Computing the Massive Chameleon

The purpose of this appendix is to justify the assumption, made in the main body of the text, that the chameleon mass can be neglected. Beginning with the equation of motion

$$\nabla^2\phi = m^2(\phi - \phi_{\rm min}^{\rm (bg)})\,, \tag{2.30}$$

performing the field redefinition $\psi = \phi - \phi_{\rm min}^{\rm (bg)}$ and writing the mass term as $m^2 = -h^2/a^2$ allows one to recover the Helmholtz equation in its canonical form. Note that h is now imaginary, so care must be taken. In spherical prolate coordinates the equation of motion to be solved is now

$$\frac{1}{(\xi^2-\eta^2)}\left\{\frac{\partial}{\partial \xi}(\xi^2-1)\frac{\partial \psi}{\partial \xi} + \frac{\partial}{\partial \eta}(1-\eta^2)\frac{\partial \psi}{\partial \eta} + \frac{\xi^2-\eta^2}{(\xi^2-1)(1-\eta^2)}\frac{\partial^2\psi}{\partial \varphi^2}\right\} = -h^2\psi\,. \tag{2.31}$$

As for the Poisson equation, has separable solutions of the form $\psi = \tilde{\Phi}(\phi)\sum_{l=0}^{\infty}X_l(\xi)H_l(\eta)$ governed by the equations

$$\frac{\partial^2\tilde{\Phi}(\varphi)}{\partial \varphi^2} + \kappa^2\tilde{\Phi}(\varphi) = 0\,, \tag{2.32}$$

$$\frac{\partial}{\partial \xi}(\xi^2-1)\frac{\partial X_l(\xi)}{\partial \xi} - \left(\frac{\kappa^2}{\xi^2-1} - h^2\xi^2 + \lambda_l\right)X_l(\xi) = 0\,, \tag{2.33}$$

$$\frac{\partial}{\partial \eta}(1-\eta^2)\frac{\partial H_l(\eta)}{\partial \eta} + \left(\frac{-\kappa^2}{1-\eta^2} - h^2\eta^2 + \lambda_l\right)H_l(\eta) = 0\,, \tag{2.34}$$

where κ and λ_l are separation constants, which are chosen to be real. Equation (2.32) has trigonometric solutions of the form $\tilde{\Phi}(\varphi) = \frac{\cos}{\sin}(\kappa\varphi)$. The equations for $X_l(\xi)$ and $H_l(\eta)$ are identical, and only differ in the ranges of the dependent coordinates ξ and η. The equation for $H_l(\eta)$ will prove easier to solve, and therefore this will be addressed first. The solution for $X_l(\xi)$ will then be determined from this by an integral transform. As the system is taken to possess an azimuthal symmetry, $\kappa = 0$ can be set to zero, implying that $\tilde{\Phi}(\varphi) = \tilde{\Phi}_0 = \text{const.}$ With this choice of κ, Equation (2.12b) resembles the Legendre equation:

$$(\eta^2 - 1)\frac{\partial^2 f_n}{\partial \eta^2} + 2\eta\frac{\partial f_n}{\partial \eta} - n(n+1)f_n = 0 \ , \tag{2.35}$$

that has solutions $f_n = P_n, Q_n$, the Legendre functions of the first and second kind respectively. In fact as will be seen shortly, the resemblance becomes exact in the massless case, when $h = 0$ and $\lambda_l = l(l+1)$ where the subscript has been introduced to λ_l as a way of marking out the particular value of l under consideration. Given the resemblance, one can attempt to solve the equation of motion for $H_l(\eta)$ as a linear superposition of Legendre functions:

$$H_l(\eta) = \sum_{n=0}^{\infty} A_n^l P_n(\eta) \ , \tag{2.36}$$

for constant A_n^l. Here, only the Legendre polynomials $P_n(\eta)$ appears in this Equation (2.36) is that the Legendre functions of the second kind, $Q_n(\eta)$ are only defined in the range $\eta > 1$ whereas the angular coordinate η covers the interval [-1,1]. Substituting Equation (2.36) into Equation (2.34) (with $\kappa = 0$) and utilising Equation (2.35) to replace the derivative terms leads to

$$\sum_{n=0}^{\infty}(h^2\eta^2 + n(n+1) - \lambda_l)A_n^l P_n = 0 \ . \tag{2.37}$$

To determine the coefficients A_n^l and the separation constants λ_l, one can make use of the recursion relation for Legendre Polynomials:

$$\eta^2 P_n = \frac{n(n-1)}{4n^2-1}P_{n-2} + \left[\frac{n^2}{4n^2-1} + \frac{(n+1)^2}{(2n+1)(2n+3)}\right]P_n + \frac{(n+1)(n+2)}{(2n+1)(2n+3)}P_{n+2} \ , \tag{2.38}$$

which when substituted into Equation (2.37) gives the following recursive relationship:

$$\begin{aligned}\sum_{n=0}^{\infty}\left[h^2\left\{\frac{n^2}{4n^2-1} + \frac{(n+1)^2}{(2n+1)(2n+3)}\right\} + (n(n+1) - \lambda_l)\right]A_n^l P_n + \\ h^2\frac{n(n-1)}{4n^2-1}P_{n-2}A_n^l + h^2\frac{(n+1)(n+2)}{(2n+1)(2n+3)}A_n^l P_{n+2} = 0 \ .\end{aligned} \tag{2.39}$$

As $P_{n<0} = 0$, it is possible to set $A_{n<0}^l = 0$ which allows for the re-arrangement each of the individual summations in Equation (2.39) to obtain

$$\begin{aligned}\sum_{n=0}^{\infty}\left[h^2\frac{(n+2)(n+1)}{(2n+3)(2n+5)}A_{n+2}^l + \left\{\left(\frac{n^2}{4n^2-1} + \frac{(n+1)^2}{(2n+1)(2n+3)}\right)h^2 + n(n+1) - \lambda_l\right\}A_n^l + \right. \\ \left. h^2\frac{n(n-1)}{(2n-3)(2n-1)}A_{n-2}^l\right]P_n = 0 \ .\end{aligned} \tag{2.40}$$

As the Legendre polynomials are orthogonal over the interval [-1,1], this equation imposes a three-term recursion formula relating coefficients for all $n \in \mathbb{N}_0$

$$h^2 \frac{(n+2)(n+1)}{(2n+3)(2n+5)} A^l_{n+2} + \left\{ \left(\frac{n^2}{4n^2-1} + \frac{(n+1)^2}{(2n+1)(2n+3)} \right) h^2 + n(n+1) - \lambda_l \right\} A^l_n + h^2 \frac{n(n-1)}{(2n-3)(2n-1)} A^l_{n-2} = 0 \; . \tag{2.41}$$

Evidently, the above interconnects alternating coefficients and admits the trivial solution $A_l = 0 \;\; \forall \;\; l$ which applies for all λ_l. Non-trivial solutions depend on either even or odd terms, it will soon be demonstrated that each of these series imposes different conditions on λ_l and therefore both cannot exist independently. The method of continued fractions may be applied to this recursion formula in order to generate a transcendental equation for λ_l. To continue it is convenient to present Equation (2.41) in a more compact fashion. Introducing three additional parameters α_n, β_n and γ_n defined by

$$\begin{aligned} \alpha_n &= h^2 \tilde{\alpha}_n \quad \text{where } \tilde{\alpha}_n = \frac{(n+2)(n+1)}{(2n+3)(2n+5)} \; , \\ \beta_n &= h^2 \tilde{\beta}_n + n(n+1) \quad \text{where } \tilde{\beta}_n = \left[\frac{n^2}{4n^2-1} + \frac{(n+1)^2}{(2n+1)(2n+3)} \right] \; , \\ \gamma_n &= h^2 \tilde{\gamma}_n \quad \text{where } \tilde{\gamma}_n = \frac{n(n-1)}{(2n-3)(2n-1)} \; , \end{aligned} \tag{2.42}$$

Equation (2.41) becomes

$$\alpha_n A^l_{n+2} + (\beta_n - \lambda_l) A^l_n + \gamma_n A^l_{n-2} = 0 \; . \tag{2.43}$$

Going further, one can define $N^l_n = -\alpha_{n-2} \frac{A^l_n}{A^l_{n-2}}$ and $\delta_n = \gamma_n \alpha_{n-2}$ to arrive at the expression

$$N^l_n = \frac{\delta_n}{\beta_n - \lambda_l - N^l_{n+2}} \; , \qquad\qquad n \geq 2 \; . \tag{2.44}$$

This allows for the construction of an infinite continued fraction for the quantity N^l_n:

$$N^l_n = \cfrac{\delta_n}{\beta_n - \lambda_l - \cfrac{\delta_{n+2}}{\beta_{n+2} - \lambda_l - \cfrac{\delta_{n+4}}{\beta_{n+4} - \lambda_l - ...}}} \equiv \left| \frac{\delta_n}{\beta_n - \lambda_l} \right| - \left| \frac{\delta_{n+2}}{\beta_{n+2} - \lambda_l} \right| - \left| \frac{\delta_{n+4}}{\beta_{n+4} - \lambda_l} \right| - ... \; , \tag{2.45}$$

where the second equality employs the standard *Pringsheim* notation as a more concise representation. Using the recursion formula of Equation (2.43) to determine the leading terms in the series ($n = 0$ and $n = 1$), one finds that

$$N^l_2 = \beta_0 - \lambda_l \; , \qquad\qquad N^l_3 = \beta_1 - \lambda_l \; , \tag{2.46}$$

where

$$0 = \beta_0 - \lambda_l - \cfrac{\delta_2}{\beta_2 - \lambda_l} + \cfrac{\delta_4}{\beta_4 - \lambda_l} + \cfrac{\delta_6}{\beta_6 - \lambda_l} - \ \ldots \ . \tag{2.47}$$

A similar expression exists for the odd entries:

$$0 = \beta_1 - \lambda_l - \cfrac{\delta_3}{\beta_3 - \lambda_l} + \cfrac{\delta_5}{\beta_5 - \lambda_l} + \cfrac{\delta_7}{\beta_7 - \lambda_l} - \ \ldots \ . \tag{2.48}$$

The roots of these two transcendental equations correspond to the various eigenvalues λ_l for the even and odd expansion of the series solution, and can be solved to any order required. See for example References [100] and [102] for more details of the general case. Of particular interest is how the solution behaves in the small mass limit ($|h| = ma \ll 1$), so the remaining part of the calculation will work under this assumption. In this case, solutions for the coefficients A_n^l and λ_l in Equation (2.43) can be built in terms of series expansions in h^2:

$$A_n^l = \sum_{i=0}^{\infty} a_{n,i}^l h^{2i}, \tag{2.49}$$

$$\lambda_l = \sum_{i=0}^{\infty} b_{l,i} h^{2i}. \tag{2.50}$$

Substituting Equations (2.49) and (2.50) into Equation (2.43) and using Equation (2.42) leads to the result

$$\sum_{i=0}^{\infty} \left[\tilde{\alpha}_n a_{n+2,i}^l h^{2i+2} + \tilde{\gamma}_n a_{n-2,i}^l h^{2i+2} + \tilde{\beta}_n a_{n,i}^l h^{2i+2} + n(n+1) a_{n,i}^l h^{2i} - a_{n,i}^l \sum_{j=0}^{\infty} b_{l,j} h^{2i+2j} \right] = 0 \ . \tag{2.51}$$

The above must hold true for all values of h, thus Equation (2.51) can be evaluated order by order in the small parameter h^2 up to $\mathcal{O}(h^4)$:

$$h^0 : n(n+1) a_{n,0}^l - a_{n,0}^l b_{l,0} = 0 \ , \tag{2.52}$$

$$h^2 : \tilde{\alpha}_n a_{n+2,0}^l + \tilde{\gamma}_n a_{n-2,0}^l + \tilde{\beta}_n a_{n,0}^l + n(n+1) a_{n,1}^l - a_{n,1}^l b_{l,0} - a_{n,0}^l b_{l,1} = 0 \ , \tag{2.53}$$

$$h^4 : \tilde{\alpha}_n a_{n+2,1}^l + \tilde{\gamma}_n a_{n-2,1}^l + \tilde{\beta}_n a_{n,1}^l + n(n+1) a_{n,2}^l - a_{n,2}^l b_{l,0} - a_{n,1}^l b_{l,1} - a_{n,0}^l b_{l,2} = 0 \ . \tag{2.54}$$

By first solving Equation (2.52), expressions for the entire range of coefficients can be built up progressively. The solution to Equation (2.52) is

$$b_{l,0} = l(l+1), \qquad a_{n,0}^l = a_0 \delta_{n,l} \ , \tag{2.55}$$

where a_0 is an unknown constant and $\delta_{n,l}$ is the Kronecker delta function. Substituting Equation (2.55) into Equation (2.53) gives

$$\tilde{\alpha}_n a_0 \delta_{n+2,l} + \tilde{\gamma}_n a_0 \delta_{n-2,l} + \tilde{\beta}_n a_0 \delta_{n,l} + n(n+1) a_{n,1}^l - a_{n,1}^l l(l+1) - a_0 \delta_{n,l} b_{l,1} = 0 \ . \tag{2.56}$$

Prompted by the three Kronecker delta functions appearing in Equation (2.56), only the cases of $n = l-2$, $n = l$, and $n = l+2$ are seen to lead to non-zero coefficients:

$$n = l-2 \ : \qquad a^l_{l-2,1} = \frac{\tilde{\alpha}_{l-2} a_0}{2(2l-1)} \ , \tag{2.57}$$

$$n = l \ : \qquad b_{l,1} = \tilde{\beta}_l, \tag{2.58}$$

$$a^l_{l,1} = a^l_1 \ \text{ an unknown constant} \ , \tag{2.59}$$

$$n = l+2 \ : \qquad a^l_{l+2,1} = -\frac{\tilde{\gamma}_{l+2} a_0}{4l+6} \ , \tag{2.60}$$

$$n \neq l-2,\ l,\ l+2 \ : \qquad a^l_{n,1} = 0 \ . \tag{2.61}$$

The results of Equation (2.57), in particular for $b_{l,0},\ a^l_{n,0}$ and $b_{l,1}$ can be incorporated into Equation (2.54) to then obtain

$$\tilde{\alpha}_n a^l_{n+2,1} + \tilde{\gamma}_n a^l_{n-2,1} + \tilde{\beta}_n a^l_{n,1} + n(n+1) a^l_{n,2} - a^l_{n,2} l(l+1) - a^l_{n,1} \tilde{\beta}_l - a_0 \delta_{n,l} b_{l,2} = 0 \ . \tag{2.62}$$

Equation (2.54) is found to only recover non-zero coefficients for the choices $n = l-4,\ n = l-2,\ n = l,\ n = l+2$ and $n = l+4$. Following the same approach as before by considering these choices individually, leads to

$$n = l-4 \ : \qquad a^l_{l-4,2} = -\frac{\tilde{\alpha}_{l-4} \tilde{\alpha}_{l-2} a_0}{8(2l-1)(3-2l)} \ , \tag{2.63}$$

$$n = l-2 \ : \qquad a^l_{l-2,2} = \frac{\tilde{\alpha}_{l-2} a^l_1}{2(2l-1)} + \frac{(\tilde{\beta}_{l-2} - \tilde{\beta}_l)\tilde{\alpha}_{l-2} a_0}{4(2l-1)^2} \ , \tag{2.64}$$

$$n = l \ : \qquad b_{l,2} = -\frac{\tilde{\alpha}_l \tilde{\gamma}_{l+2}}{2(2l+3)} + \frac{\tilde{\alpha}_{l-2} \tilde{\gamma}_l}{2(2l-1)}, \tag{2.65}$$

$$a^l_{l,2} = a^l_2 = \text{unknown constant} \ , \tag{2.66}$$

$$n = l+2 \ : \qquad a^l_{l+2,2} = \frac{\tilde{\gamma}_{l+2} a^l_1}{2(2l+3)} + \frac{(\tilde{\beta}_{l+2} - \tilde{\beta}_l)\tilde{\gamma}_{l+2} a_0}{4(2l+3)^2} \ , \tag{2.67}$$

$$n = l+4 \ : \qquad a^l_{l+4,2} = \frac{\tilde{\gamma}_{l+4} \tilde{\gamma}_{l+2} a_0}{8(2l+3)(2l+5)} \ , \tag{2.68}$$

$$n \neq l-4,\ l-2,\ l,\ l+2,\ l+4 \ : \qquad a^l_{n,2} = 0 \ . \tag{2.69}$$

One this point one can begin to determine some of these coefficients. Considering the case of $l = 0$, using Equation (2.42) in Equations (2.55), (2.57)-(2.61) and (2.63)-(2.68) leads to

$$b_{0,0} \ = \ 0;\ a^0_{n,0} = a_0 \delta_{n,0};\ b_{0,1} = \frac{1}{3} \ , \tag{2.70}$$

$$a^0_{0,1} \ = \ a_1 = \ \text{constant};\ a^0_{2,1} = -\frac{a_0}{9};\ a^0_{n,1} = 0 \text{ for } n \neq 0, 2 \ , \tag{2.71}$$

$$a^0_{0,2} \ = \ a^0_2 = \ \text{constant};\ b_{0,2} = -\frac{2}{135};\ a^0_{2,2} = -\frac{a_1}{9} + \frac{2a_0}{567};\ a^0_{4,2} = \frac{a_0}{525} \ . \tag{2.72}$$

It follows from Equation (2.49) that

$$A_0^0 = a_0 + a_1 h^2 + a_2^0 h^4 + \mathcal{O}(h^6) \,, \tag{2.73}$$

$$A_2^0 = -\frac{a_0}{9} h^2 - \left(\frac{a_1}{9} - \frac{2a_0}{567} \right) h^4 + \mathcal{O}(h^6) \,, \tag{2.74}$$

$$A_4^0 = \frac{a_0}{525} h^4 + \mathcal{O}(h^6), \tag{2.75}$$

and from Equation (2.50) that

$$\lambda_0 = \frac{1}{3} h^2 - \frac{2}{135} h^4 + \mathcal{O}(h^6) \,. \tag{2.76}$$

What remains is to determine the values of the remaining unknown coefficients $a_0,\ a_1$ and a_2^0. This can be done through normalisation, which involves imposing that the angular solution $H_l(\eta)$ given in Equation (2.36) has the same normalisation factor as that of a single spherical harmonic $P_l(\eta)$. Recalling that

$$\int_{-1}^{1} P_m(\eta) P_k(\eta) \, \mathrm{d}\eta = \frac{2}{(2m+1)} \delta_{m,k} \,, \tag{2.77}$$

it follows that normalisation requires

$$\int_{-1}^{1} (H_l(\eta))^2 \, \mathrm{d}\eta = \frac{2}{(2l+1)} \,, \tag{2.78}$$

Substituting Equation (2.49) into Equation (2.36) and expanding to $\mathcal{O}(h^4)$ recovers the expression

$$\begin{aligned} H_l(\eta) &= a_0 P_l + (a^l_{l-2,1} P_{l-2} + a^l_{l,1} P_l + a^l_{l+2,1} P_{l+2}) h^2 \\ &\quad + (a^l_{l-4,2} P_{l-4} + a^l_{l-2,2} P_{l-2} + a^l_{l,2} P_l + a^l_{l+2,2} P_{l+2} + a^l_{l+4,2} P_{l+4}) h^4 + \mathcal{O}(h^6) \end{aligned} \tag{2.79}$$

Inserting into the normalisation condition Equation (2.78) and using Equation (2.77) we obtain

$$\begin{aligned} \int_{-1}^{1} (H_l(\eta))^2 \, \mathrm{d}\eta &= \frac{2}{2l+1} a_0^2 + \frac{4 a_0 a_1}{2l+1} h^2 + \left[\frac{4 a_0 a^l_2}{2l+1} + \frac{2 a_1^2}{2l+1} + \frac{2 (a^l_{l-2,1})^2}{2l-3} + \frac{2 (a^l_{l+2,1})^2}{2l+5} \right] h^4 \\ &= \frac{2}{(2l+1)} \,. \end{aligned} \tag{2.80}$$

Then, solving Equation (2.80) at each order in h^2 gives:

$$h^0 \ : \ a_0^2 = 1 \rightarrow a_0 = 1 \,, \tag{2.81}$$

$$h^2 \ : \ a_1 = 0 \,, \tag{2.82}$$

$$h^4 \ : \ a^l_2 = -\frac{1}{8} \left(\frac{l^2 (l-1)^2}{(2l-3)(2l+1)(2l-1)^4} + \frac{(l+2)^2 (l+1)^2}{(2l+5)(2l+1)(2l+3)^4} \right) . \tag{2.83}$$

In particular for the case $l = 0$, Equation (2.83) yields

$$a_2^0 = -\frac{1}{810} \, . \tag{2.84}$$

Substituting for a_0, a_1 and a_2^0 from Equations (2.81), (2.82) and (2.84) into Equations (2.73)-(2.75) specifies the series expansion coefficients to be

$$\begin{aligned} A_0^0 &= 1 - \frac{1}{810}h^4 + \mathcal{O}(h^6) \, , & (2.85) \\ A_2^0 &= -\frac{1}{9}h^2 + \frac{2}{567}h^4 + \mathcal{O}(h^6) \, , & (2.86) \\ A_4^0 &= \frac{1}{525}h^4 + \mathcal{O}(h^6) \, . & (2.87) \end{aligned}$$

These may be consolidated with Equation (2.36) to obtain an expression for the angular solution up to terms of order h^4:

$$\begin{aligned} H_0(\eta) &= A_0^0 P_0(\eta) + A_2^0 P_2(\eta) + A_4^0 P_4(\eta) \\ &= \left(1 - \frac{1}{810}h^4\right) P_0(\eta) - \left(\frac{1}{9}h^2 - \frac{2}{567}h^4\right) P_2(\eta) + \frac{1}{525}h^4 P_4(\eta) + \mathcal{O}(h^6) \, . \end{aligned} \tag{2.88}$$

It follows that the massless limit $h = 0$ results in equality $H_0(\eta) = P_0(\eta)$. Moreover by considering λ_l defined in Equation (2.50) and using Equation (2.55) we see that

$$\lambda_l = l(l+1) + O(h^2) \, . \tag{2.89}$$

which justifies the Legendre form of the equations that have been used in the massless limit. This technique can of course be generalised to derive $H_l(\eta)$ for $l > 0$, but this is left to the interested reader. The primary aim of this appendix has been to demonstrate how small mass corrections feed into the chameleon solutions around an ellipsoidal source, where it has been shown that these corrections enter at order h^2 which supports the use of the massless approximation.

2.B.1 The Radial Solutions

Although as can be seen by comparing Equations (2.33) and (2.34), the radial component $X_l(\xi)$ of the field obeys the same differential equation as the angular component $H_l(\eta)$, it is defined over the coordinate range $1 \leq \xi \leq \infty$ rather than $-1 \leq \eta \leq 1$. Since the angular solution $H_l(\eta)$ is comprised of Legendre polynomials that are only defined over the interval $[-1, 1]$ they are not applicable as solutions to the radial equation (Equation (2.33)). Moreover, the method employed to derive the angular solution utilised a recursion relation that does not hold for Legendre functions of the second kind and so we cannot repeat this analysis to determine $X_l(\xi)$. Nonetheless, a solution valid over the appropriate coordinate range can be found; a result presented in Reference [100] shows that, if a function $H_l(\eta)$ is a solution to a problem of the form shown in Equation (2.34), then another solution, say

$\chi^l(h\xi)$ may be obtained by performing an integral transform. The transform of the angular solution, in its general form $H_l(\eta) = \sum_{n=0}^{\infty} A_n^l P_n(\eta)$, corresponds to

$$\chi^l(h\xi) = \sum_{n=0}^{\infty} A_n^l \int_{-1}^{1} e^{ih\xi\eta}\, P_n(\eta)\, \mathrm{d}\eta \,. \tag{2.90}$$

This can be solved by employing the following relation between the Legendre polynomials and Bessel functions of the first kind:

$$J_{n+\frac{1}{2}}(h\xi) = (i^n\sqrt{2\pi})^{-1}\Big(\frac{h\xi}{2}\Big)^{1/2} \int_{-1}^{1} e^{ih\xi\eta}\, P_n(\eta)\, \mathrm{d}\eta \,, \tag{2.91}$$

and a second, linearly independent solution can be found using a related identity for Bessel functions of the second kind $Y_{n+\frac{1}{2}}(h\xi)$ as they have the same derivative properties. Together, the two independent solutions read

$$\begin{aligned} \chi_1^l(h\xi) &= \Big(\frac{2\pi}{h\xi}\Big)^{1/2} \sum_{n=0}^{\infty} A_n^l\, i^n\, J_{n+\frac{1}{2}}(h\xi) \,, \\ \chi_2^l(h\xi) &= \Big(\frac{2\pi}{h\xi}\Big)^{1/2} \sum_{n=0}^{\infty} A_n^l\, i^n\, Y_{n+\frac{1}{2}}(h\xi) \,. \end{aligned} \tag{2.92}$$

The general solution is therefore constructed by taking a linear superposition of the above:

$$X_l(\xi) = W^l \chi_1^l(h\xi) + V^l \chi_2^l(h\xi) \,, \tag{2.93}$$

with the index l being introduced to allow for the integration parameters W^l, V^l to vary with different values of the separation constant, λ_l. Reintroducing the chameleon mass, $m = -ih/a$, the full solution is found to be

$$\psi(\xi,\eta) = \sum_{l=0}^{\infty}\sum_{k=0}^{\infty} A_k^l P_k(\eta) \sum_{n=0}^{\infty} \Big(\frac{2\pi}{ma\xi}\Big)^{1/2} A_n^l i^{(n+3/2)} \Big\{ W^l J_{n+\frac{1}{2}}(ima\xi) + V^l Y_{n+\frac{1}{2}}(ima\xi) \Big\} \,. \tag{2.94}$$

The constant value introduced by the normalisation of the polar solution $\tilde{\Phi}_0$ has been absorbed into the values of W^l, V^l. In considering to massless limit of the radial solutions $X_l(\xi)$, one needs to proceed a little more carefully as there are superficial divergences that arise when taking $m \to 0$. The best way to handle this seems to be to transform the radial Bessel functions appearing in Equation (2.93) into modified Bessel functions using

$$\begin{aligned} J_\sigma(ix) &= e^{\frac{\sigma i\pi}{2}} I_\sigma(x) \,, \\ Y_\sigma(ix) &= i e^{\frac{\sigma i\pi}{2}} I_\sigma(x) - \frac{2}{\pi} e^{-\frac{\sigma i\pi}{2}} K_\sigma(x) \,, \end{aligned} \tag{2.95}$$

where $I_\sigma(x)$ and $K_\sigma(x)$ correspond to exponentially growing and decaying functions respectively. The solution presented in Equation (2.93) then becomes

$$X_l(\xi) = -\Big(\frac{2\pi}{ima\xi}\Big)^{1/2} \sum_{n=0}^{\infty} A_n^l i^n \Big((W^l + iV^l) e^{i\pi/4} e^{\frac{in\pi}{2}} I_{n+\frac{1}{2}}(ma\xi) - \frac{2V^l}{\pi} e^{-i\pi/4} e^{-\frac{in\pi}{2}} K_{n+\frac{1}{2}}(ma\xi) \Big) \,. \tag{2.96}$$

Regularity as $\xi \to \infty$ implies that $W^l + iV^l = 0$ in order to cancel the divergence arising in the $I_{n+\frac{1}{2}}(ma\xi)$ term. $X_l(\xi)$ then simplifies to

$$X_l(\xi) = \frac{2}{\pi}\left(\frac{2\pi}{ima\xi}\right)^{1/2} e^{-i\pi/4} V^l \sum_{n=0}^{\infty} A_n^l i^n e^{-\frac{in\pi}{2}} K_{n+\frac{1}{2}}(ma\xi) \ . \tag{2.97}$$

It then proves convenient to express Equation (2.97) in terms of a *Hankel Function* of the first kind which is related to the Bessel function $K_\nu(z)$ via

$$K_\nu(z) = \frac{i\pi}{2} e^{i\pi\nu/2} H_\nu^{(1)}(ze^{i\pi/2}) \quad [-\pi < \arg z \leq \pi/2] \ , \tag{2.98}$$

from which it follows that

$$X_l(\xi) = -W^l \left(\frac{2\pi}{ima\xi}\right)^{1/2} \sum_{n=0}^{\infty} A_n^l i^n H_{n+\frac{1}{2}}^{(1)}(ima\xi) \ . \tag{2.99}$$

Now recalling $\psi = \phi - \phi_{\min}^{(\mathrm{bg})}$, it follows from Equation (2.94) using Equation (2.99) that the complete solution for the massive system is

$$\phi(\xi,\eta,\phi) = -\left(\frac{2\pi}{ima\xi}\right)^{1/2} \sum_{l=0}^{\infty}\sum_{k=0}^{\infty} W^l A_k^l P_k(\eta) \sum_{n=0}^{\infty} A_n^l i^n H_{n+\frac{1}{2}}^{(1)}(ima\xi) \ + \ \phi_{\min}^{(\mathrm{bg})} \ . \tag{2.100}$$

Using the above result makes it much easier to deal with the small mass limit, or more precisely the limit $ma \ll 1$. In this case, taking $ma \ll 1$ translates to a small argument for the Hankel function (of the first kind), which obeys

$$\lim_{z\to 0} \ H_\nu^{(1)}(z) = -\frac{i}{\pi}\Gamma(\nu)\left(\frac{1}{2}z\right)^{-\nu} \ , \tag{2.101}$$

where $\Gamma(\nu)$ is the Gamma function. It follows that when $ma \ll 1$, we have

$$\phi(\xi,\eta,\phi) = \frac{1}{\sqrt{\pi}} \sum_{l=0}^{\infty}\sum_{k=0}^{\infty} W^l A_k^l P_k(\eta) \sum_{n=0}^{\infty} A_n^l \, \Gamma\left(n+\frac{1}{2}\right) \left(\frac{2}{ma\xi}\right)^{n+1} \ + \ \phi_{\min}^{(\mathrm{bg})} \ . \tag{2.102}$$

On the surface there doesn't appear to be a well defined limit as $ma \to 0$, as each successive term in the sum over n appears to diverge more and more rapidly as n increases. However this isn't the case as will be demonstrated now. Recall A_n^l is given as an expansion in ma through Equation (2.49). Inserting this into Equation (2.102) gives

$$\phi(\xi,\eta,\phi) = \frac{1}{\sqrt{\pi}} \sum_{l=0}^{\infty}\sum_{k=0}^{\infty} W^l A_k^l P_k(\eta) \sum_{n=0}^{\infty}\sum_{j=0}^{\infty} a_{n,j}^l (-1)^j (ma)^{2j-n-1} \Gamma\left(n+\frac{1}{2}\right)\left(\frac{2}{\xi}\right)^{n+1} + \phi_{\min}^{(\mathrm{bg})} \ . \tag{2.103}$$

This still doesn't look particularly good, but there are conditions on the parameter $a_{n,j}^l$. Extending the analysis which led to Equations (2.61) and (2.69), it follows that all of the coefficients $a_{n,j}^l = 0$ unless $l - 2j \leq n \leq l + 2j$. In particular for the non-zero coefficients $a_{n,j}^l$,

there is the bound $2j-n-1 \geq -(l+1)$. This implies that when coefficients are non-zero, the mass of the field always entails divergent inverse-power terms in Equation (2.103). However, these divergences can be systematically cancelled by recalling that the coefficients W^l are so far undetermined. Therefore, one is completely free to rewrite $W^l = \tilde{W}^l(ma)^{(l+1)}$, and with which guarantees that there are no divergent contributions to the series expansion in Equation (2.103). Now, in the limit that $ma \to 0$, only the term $2j - n - 1 = -(l + 1)$ survives and all the rest go to zero. Incorporating $\tilde{W}^l$ into Equation (2.103) leads to the result

$$\phi(\xi,\eta,\phi) = \frac{1}{\sqrt{\pi}}\sum_{l=0}^{\infty}\sum_{k=0}^{\infty}\tilde{W}^l A_k^l P_k(\eta)\sum_{n=0}^{\infty}\sum_{j=0}^{\infty}a_{n,j}^l(-1)^j(ma)^{2j-n+l}\,\Gamma\left(n+\frac{1}{2}\right)\left(\frac{2}{\xi}\right)^{n+1} + \phi_{\min}^{(\mathrm{bg})}\,, \tag{2.104}$$

where now the $(ma)^{2j-n+l}$ term does not diverge as $m \to 0$. To close this section, we demonstrate consistency of this solution by showing that the general $l = 0$ solution for the massive case reduces to the solution of the massless problem when setting $m = 0$. As a reminder, the (exterior) chameleon field equation (Equation (2.17)) for a massless system reduces to the Laplace equation, where the solutions to this problem were presented when discussing the external solutions for gravity. Therefore, the target is to recover the $l = 0$ entry of

$$\phi(\xi,\eta,\phi) = \sum_{l=0}^{\infty}\varphi_l(\xi,\eta,\phi) = \sum_{l=0}^{\infty}W_l P_l(\eta)Q_l(\xi)\,, \tag{2.105}$$

from the massive $l = 0$ result:

$$\phi_0(\xi,\eta,\phi) = \frac{1}{\sqrt{\pi}}\sum_{k=0}^{\infty}\tilde{W}^0 A_k^0 P_k(\eta)\sum_{n=0}^{\infty}\sum_{j=0}^{\infty}a_{n,j}^0(-1)^j(ma)^{2j-n}\,\Gamma\left(n+\frac{1}{2}\right)\left(\frac{2}{\xi}\right)^{n+1} + \phi_{\min}^{(\mathrm{bg})}\,, \tag{2.106}$$

with the subscript of zero signifying that the above corresponds to the $l = 0$ component of the complete solution. Quoting a result from the preceding discussion, in the massless case the only surviving series coefficient of the form A_n^l is A_l^l i.e when $l = n$ (see Equations (2.49) and (2.52)). Further, inspection of Equation (2.104) for $l = 0$ shows that all but one of the radial terms inherit a mass dependence, with the exception being when $2j = n$. Collectively, these results can be used to eliminate two of the three summations: allowing one to write

$$\phi_0(\xi,\eta,\phi) = \frac{1}{\sqrt{\pi}}\,\tilde{W}^0\,P_0(\eta)\sum_{n=0}^{\infty}a_{n,n/2}^0\,(-1)^{n/2}\,\Gamma\left(n+\frac{1}{2}\right)\left(\frac{2}{\xi}\right)^{n+1} + \phi_{\min}^{(\mathrm{bg})}\,. \tag{2.107}$$

Previously, in Equations (2.72) and (2.81), the coefficients $a_{n,n/2}^0$ were determined up to $n = 4$ and given by

$$a_{0,0}^0 = 1\,, \qquad a_{2,1}^0 = -\frac{1}{9}\,, \qquad a_{4,2}^0 = \frac{1}{525}\,. \tag{2.108}$$

Expanding the summation explicitly the first three terms of the Taylor series are identified to be

$$\phi_0(\xi,\eta,\phi) = \frac{\tilde{W}^0}{\sqrt{\pi}\xi}P_0(\eta)\left\{\Gamma\Big(\frac{1}{2}\Big) + \frac{4}{9}\,\Gamma\Big(\frac{5}{2}\Big)\frac{1}{\xi^2} + \frac{16}{525}\,\Gamma\Big(\frac{9}{2}\Big)\frac{1}{\xi^4} + \ldots\right\} + \phi_{\min}^{(\mathrm{bg})}\,, \tag{2.109}$$

substituting the numerical values of the gamma functions gives

$$\phi_0(\xi,\eta,\phi) = \tilde{W}^0\, P_0(\eta)\left\{\frac{1}{\xi} + \frac{1}{3}\frac{1}{\xi^3} + \frac{1}{5}\frac{1}{\xi^5} \;+\; \ldots\right\} +\; \phi_{\text{min}}^{(\text{bg})}\;, \tag{2.110}$$

The terms appearing in brackets correspond to the series expansion of the Legendre function of second kind $Q_0(\xi)$. Therefore, the massless result for $l = 0$ is described by

$$\varphi_0(\xi,\eta,\phi) = \tilde{W}^0 P_0(\eta) Q_0(\xi)\;, \tag{2.111}$$

as recovered for the $l = 0$ case when solving the exterior Laplace equation (Equation (2.105)).

2.C Relating Ellipsoidal to Spherical coordinates

In the large distance limit $\xi \gg 1$ the relationship between ellipsoidal and spherical coordinates that can be inferred from Equation (2.26) becomes

$$\begin{aligned} a\xi\sqrt{1-\eta^2} &= r\text{sin}(\theta)\;, \\ a\xi\eta &= r\text{cos}(\theta)\;. \end{aligned} \tag{2.112}$$

This simplifies to

$$\eta = \cos(\theta)\;, \qquad \xi = \frac{r}{a}\;. \tag{2.113}$$

We have described the size of the ellipsoids in this work in terms of a reference sphere of the same volume. Equating the volumes of a sphere of radius R with an ellipsoid of focal length a and surface position ξ_0 gives

$$\frac{4}{3}\pi R^3 = \int \text{d}V_{\text{ellipsoid}} = \int_0^{2\pi}\int_{-1}^{1}\int_1^{\xi_0} h_\xi h_\eta h_\varphi \;\text{d}\xi\text{d}\eta\text{d}\varphi\;. \tag{2.114}$$

Recalling the scale factors

$$h_\xi = a\sqrt{\frac{\xi^2-\eta^2}{\xi^2-1}}\;, \quad h_\eta = a\sqrt{\frac{\xi^2-\eta^2}{1-\eta^2}}\;, \quad h_\phi = a\sqrt{(\xi^2-1)(1-\eta^2)}\;, \tag{2.115}$$

we find that

$$R^3 = a^3\xi_0\Big(\xi_0^2 - 1\Big)\;. \tag{2.116}$$

This assigns an effective radius to an ellipsoid defined by ξ_0.

Chapter 3

Solving the Chameleon Field Equation using Finite Element Analysis

One thing that holds universally true across the various screened scalar fields theories is that they don't present particularly user-friendly differential equations. Their highly non-linear nature means that even solving their boundary value problems around something as routine as a spherical source object calls for a host of approximations to be made. However, it is precisely the non-linearities that define these models which makes the consideration of alternative source objects an interesting topic. In moving to the ellipsoid for the case of the chameleon model, a similar range of approximations lead to a solvable yet complicated system of equations that perpetuated the idea that departures from a spherical source geometry may be the way forward when it comes to constraining the parameter space of the theory. Ultimately, what is needed is a means of systematically assessing the various possibilities of source shape that are available, without having to launch into a full, and likely infeasible analytic study each time. For this reason, a decision was made to shift focus towards a numerical treatment of the problem, which subsequently unlocked much greater possibilities for consideration. In addition to this, approaching the system numerically makes implementing the entire experimental configuration much more straightforward.[1] This in principle, then opens up the potential to study, and generate constraints for screened scalar fields across the host of both ongoing and upcoming fifth-force experiments [86, 108–110].

The various numerical schemes around to deal with partial differential equations generally fall into three categories: the finite difference method (FDM), the finite element method (FEM), and the finite volume method (FVM). The oldest and probably most familiar of these, the FDM, is built around using Taylor expansions as a means to approximate derivatives on a discretised space. Although it is often praised for its simplicity, the method relies on a topologically structured (often equispaced) grid. This approach can be highly problematic for non-linear problems, due to their tendency for field variations to occur over very

[1] Taking the example of solving around a source in a spherical vacuum chamber, dealing with this problem by hand would prove tricky due to the complexities involved with having to impose boundary conditions across what would be a spherical surface in a non-spherical coordinate system.

short distance scales. On a logically square network, this can drive the truncation errors associated with derivative approximations fatally high unless excessive computational resources are allocated to the problem. For the same reasons, this also makes the FDM the suboptimal choice for considering complex source geometries due to the possibility of acute variations in the density field.

Unlike the finite difference method, the two remaining approaches (FEM and FVM) do not rely on the strong (differential) form of the equations describing the problem. Instead, they utilise integral forms which avoid the need for a specific discretisation of the target domain. Accordingly, it is possible to construct a discrete space tailored to meet the demands of the problem. This technique also allows for discontinuities in the density field (generally arising when implementing a source object) to be handled much more readily as a result of relaxed conditions on the regularity of the discrete solution (that is, the integral forms are less sensitive to high values of local derivatives). To add to this, Neumann boundary conditions appear naturally within the formulation meaning that one doesn't have to enforce them by hand as is the case for the finite difference method. All of these advantages do come at a cost, as it makes designing and implementing such methods from the ground up a huge endeavour. Fortunately, the automated solution of differential equations was the target of the FEniCS Project, launching in 2003, which has led to a state of the art collection of software libraries built around the finite element framework. The platform, developed for both C++ and Python, was found to be incredibly suitable for dealing with non-linear systems and as a result, the work presented in this chapter was obtained, and in many ways made possible by the numerical machinery provided by the FEniCS Project [111].

To keep things in line with previous work, data will be gathered and presented exclusively for the case of the chameleon model. However, this was more a consequence of time limitations. In fact, the program was designed in such a way that it could be easily extended to produce the corresponding data for the symmetron field. This is discussed briefly in Appendix 3.A. In principle, the dilaton field could also be incorporated into this work, although the presence of a non-canonical kinetic term makes the task of reaching the integral statement of the problem a little more involved. That being said, examples of applying the finite element method to numerous problems involving non-standard derivative terms are presented within the FEniCS Project documentation. Therefore, one would not expect to face any additional complications within the implementation of the solver.

The scope of this work was two-fold. The primary objective was to study a catalogue of different source geometries in the context of an atom interferometry experiment searching for the chameleon interaction. In particular, to better understand the various factors at play when it comes to choosing the optimal geometry for constraining the theory. However, as the project developed, the viability of the finite element method came incredibly apparent. As a tool most often found within the remit of computational fluid dynamics, a secondary target became to demonstrate the utility of the finite element solver when dealing with non-linear models of dark energy.

To begin, this chapter will include some background material on the finite element method.

This will be followed by a formal definition of the problem and an on-the-fly discussion of the mathematical tools required for its implementation into the numerical system. Details of the simulation procedure will then be covered before moving on to the results of this research.

3.1 Piecewise Linear Approximations and the Finite Elements

One of the central concepts behind finite element analysis is the piecewise approximation of functions using polynomials. The idea was initially suggested by Richard Courant in the early 1940's [112] before being picked up by structural engineers in search for an improved technique for numerically dealing with complicated elliptic systems. At the heart of this idea, was the set of linear functions $\mathbb{P}_1$ of two variables such that

$$\phi(x_1, x_2) = a_0 + a_1 x_1 + a_2 x_2 \ . \tag{3.1}$$

The unknown coefficients of such functions $\phi \in \mathbb{P}_1$ are uniquely determined by its values on the vertices of a non-degenerate triangle.[2] Suppose that instead of describing a function on a single triangle, the target is to describe a function over some polygon Ω. The same logic for a function over a single triangle can be applied by subdividing the domain into a network of triangles, known as a triangulation. Introducing the space of linear functions $\mathbb{P}_1 = \{a_0 + a_1 x_1 + a_2 x_2 | a_0, a_1, a_2 \in \mathbb{R}\}$ within each triangle P_i, a function ϕ will be uniquely determined by its values at the vertices of this triangulation. Furthermore, as the values of $\phi|P_i \in \mathbb{P}_1$ along an edge depend only on the values at the connecting vertices, the piecewise description of ϕ is automatically continuous across edges. An example triangulation for the case of a trapezium is depicted in Figure 3.1. Denoting the N vertices within the triangulation as $\mathbf{p}_i$ where $i = 1, 2, \ldots, N$, it is useful to define a linear function e_i such that

$$e_i(p_j) = \delta_{ij} \ , \tag{3.2}$$

which graphically looks like a pyramid, reaching its apex value of 1 for vertex $i = j$ and falls to zero for all others. It was found that the function ϕ defined over Ω can be built using e_i as a basis:

$$\phi(x_1, x_2) = \sum_{i=1}^{N} \phi\left(\mathbf{p}_i\right) e_i(x_1, x_2) \ . \tag{3.3}$$

As the value of e_i is only non-zero within triangles containing the vertex $\mathbf{p}_i$, this is known as a local basis. What this has achieved is to break the problem space into finite (triangular) elements and use a local basis to construct a piecewise linear (linear within each triangle) yet globally continuous function. This globally continuous function can be the approximation to the exact solution of a partial differential equation, which is exactly how the finite element method handles the transition to a discrete space. Here, in contrast to the finite difference method, the process is not confined to a structured grid. Instead, the user is free

[2] A degenerate triangle can be described by three collinear points, which would form a line when connected. There would therefore be a redundant point which doesn't provide any more information, thus the three unknowns of the linear function would not be fully specified.

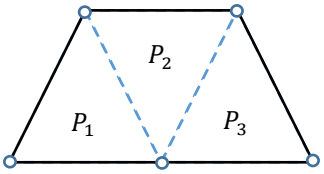

Figure 3.1: Example triangulation of a trapezium. The polygon is broken into three triangular subdomains P_i. Common edges are represented by the dashed blue lines to emphasize the continuity of a piecewise linear function across the boundary. The vertices used to calculate the unknown coefficients of each linear function are identified using circles.

to define the triangulation, on *whichever* domain most suits the problem.[3] This could be as straightforward as locally tuning element size in regions of interest, to something as involved as triangulating an aeroplane wing to study air flow.

3.2 The Chameleon Field within a Spherical Vacuum Chamber

To keep things simple, the numerical system will be built by embedding a spherical vacuum chamber within a square domain.[4] As depicted by Figure 3.1, the width of the simulation box will be denoted W and the radius of the vacuum chamber will be given by R_C. The boundary value problem in question, defined over the domain Ω with boundary $\partial\Omega$ then appears as follows:

$$\begin{aligned} \nabla^2\phi &= -\frac{\Lambda^5}{\phi^2} + \frac{\rho}{M}, && \text{in } \Omega \ , \\ \phi &= \phi_{\text{min}}^{(\text{wall})} && \text{on } \partial\Omega \ . \end{aligned} \tag{3.4}$$

To handle this problem using a finite element solver, the above must be reformulated into its variational (or weak) form. This involves recalling a well known result from vector calculus known as Green's Theorem, which states that for two scalar fields ϕ, φ we have

$$\int_\Omega \left(\nabla^2\phi\right)\varphi + \int_\Omega \nabla\phi\cdot\nabla\varphi = \int_{\partial\Omega} \left(\partial_n\phi\right)\varphi \ , \tag{3.5}$$

where the term appearing on the right hand side $\partial_n\phi$ denotes the exterior normal derivative which is otherwise written as $\nabla\phi\cdot\hat{\mathbf{n}}$. The unit normal vector $\hat{\mathbf{n}}$ is defined for points along the

[3] In truth, there are some relatively light restrictions on the method of triangulation. However, these more control how adjacent triangles should meet as opposed to the overall shape of the triangulation.

[4] Unlike the finite difference method, the FEM accommodates domains of arbitrary construction, meaning that in principle one could have solved the problem on a circular/spherical domain.

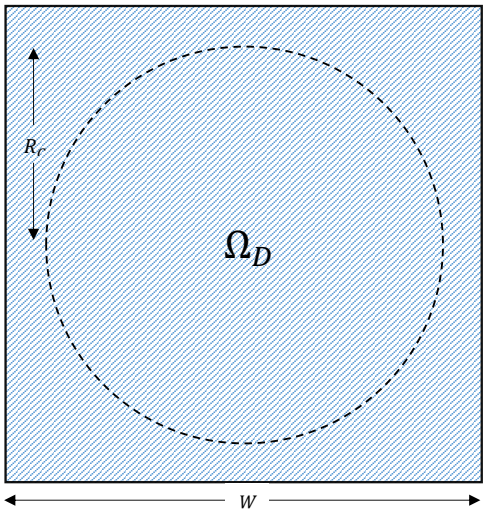

Figure 3.1: Illustration of the simulation space, denoted Ω_D. The boundary of the spherical vacuum chamber of radius R_C is depicted using the dotted line. The total width of the domain is given by W.

boundary $\partial\Omega$, pointing outwards from the domain Ω. The variational form of this problem then follows from introducing the field equation of Equation (3.4) into the above through the $\nabla^2\phi$ term to give

$$\int_\Omega \left(\frac{-\Lambda^2}{\phi^2} + \frac{\rho}{M}\right)\varphi + \int_\Omega \nabla\phi\cdot\nabla\varphi = \int_{\partial\Omega} (\partial_n\phi)\,\varphi\ . \tag{3.6}$$

The next task is to deal with the boundary term appearing on the right-hand side of Equation (3.6). The easiest way to do this is to construct the vacuum chamber in such a way that the thickness of the walls is always greater than the Compton wavelength of the field $\lambda_\phi^{(\mathrm{wall})}$. This ensures that the field falls to its expectation value within the walls, which in turn implies that the Neumann boundary term $\partial_n\phi$ can be set to zero. More formally, if we define the half-width of the simulation mesh as W with the chamber radius as R_C, then we have

$$W - R_C > \frac{1}{\sqrt{2}}\left(\frac{\Lambda^5 M^3}{\rho_{\mathrm{wall}}}\right)^{1/4}\ , \qquad \forall\, M,\ \Lambda\ . \tag{3.7}$$

Satisfying the above,[5] the Neumann boundary term disappears and Equation (3.6) simplifies to

$$\int_\Omega \left(\frac{-\Lambda^2}{\phi^2} + \frac{\rho}{M}\right)\varphi + \int_\Omega \nabla\phi\cdot\nabla\varphi = 0\ , \qquad \forall\varphi\ . \tag{3.8}$$

[5]This corresponds to $W - R_C > 0.1$mm for $\Lambda = 10^{-10}$ GeV, $M = M_{\mathrm{PL}}$ and $\rho_{\mathrm{wall}} = 1\,\mathrm{gcm}^{-3}$. Data was gathered for a chamber radius of 15cm and a system half-width of 18cm which falls well within this margin for all parameter choices of interest.

At this point, ϕ is now the unknown chameleon field and φ is an arbitrary function. This function, φ, is known within the finite element literature as a test function, with its sole use being to verify the equation satisfied by the unknown ϕ. Accordingly, φ is not an unknown of the system, but instead something introduced to write down the problem. Generally speaking, when moving to a discretised system for numerical analysis, the established choice is to take the test function as the nodal basis function(s) $\sum e_i$ used to build the finite element space, something known as the Galerkin method. This approach is ideal as the resulting matrices to be handled by the solver are symmetric in addition to relaxing the smoothness requirements on the field ϕ [112, 113]. Further, as this basis is almost orthogonal (for the most part $\int\int e_i e_j = 0$ as the only time both of the basis entries are non-zero is if they belong to the same triangle) the matrices handled by the solver are sparse. Note, this is advantageous from a computational perspective as only non-zero elements alongside their indices need to be stored. As a result, this significantly reduces computation time by eliminating the operations performed on the zero elements. The variational form in Equation (3.8) above corresponds to a semi-linear form, being non-linear in the unknown ϕ and linear in the test function φ. In order to call the finite element solver for this problem, we need to arrive at linear and bilinear forms for the fields ϕ and φ. This involves linearising the inverse power term for ϕ around some input solution denoted ϕ_k. To achieve this, the non-linear term is expanded around the input function ϕ_k as

$$\frac{1}{\phi^2} \approx \frac{1}{\phi_k^2} - \frac{2}{\phi_k^3}\left(\phi - \phi_k\right) + \mathcal{O}((\phi - \phi_k)^2) = \frac{3}{\phi_k^2} - \frac{2}{\phi_k^3}\phi + \dots \ . \tag{3.9}$$

Following this, the chameleon equation to be solved in its integral form becomes

$$\int_\Omega \left\{ \nabla\phi \cdot \nabla\varphi + \left(\frac{2\Lambda^5}{\phi_k^2}\phi \right) \varphi \right\} = \int_\Omega \left\{ \left(\frac{3\Lambda^5}{\phi_k^2} - \frac{\rho}{M} \right) \varphi \right\} \ , \tag{3.10}$$

from which the left-hand side is identified to be the bilinear term $a(\phi, \varphi)$ and the linear form $L(\varphi)$ as the right-hand side. Note that the above describes the full three dimensional system. Simulations will be performed by utilising the rotational symmetry such as to project the problem onto a two-dimensional space. Transforming to cylindrical polar coordinates (x, z, θ) has the effect of introducing a correction to the two-dimensional Laplacian such that the weak form of Equation (3.10) becomes

$$\int_\Omega \left\{ \nabla\phi \cdot \nabla\varphi + \left(\frac{2\Lambda^5}{\phi_k^2}\phi + \frac{1}{x}\frac{\partial\phi}{\partial x} \right) \varphi \right\} = \int_\Omega \left\{ \left(\frac{3\Lambda^5}{\phi_k^2} - \frac{\rho}{M} \right) \varphi \right\} \ . \tag{3.11}$$

In order to avoid numerical instabilities, some manipulation is required to express the problem in units more applicable to the system. Ideally we want to write the chameleon field equation at the centimetre scale which is more appropriate to the system size. This rescaling essentially allows for sensible variations in the field values to be resolved by the grid. As Equation (3.4) is currently written in [GeV], the move to inverse centimetres [cm^{-1}] can be achieved by introducing the constant α_m, which represents the corresponding conversion factor

$$\alpha_{cm} = 5.0667 \times 10^{13}\ \mathrm{GeV}^{-1}\mathrm{cm}^{-1} \ . \tag{3.12}$$

As a result, the gradient operator quoted in S.I units $\tilde{\nabla}^2$ follows from the relation

$$\nabla^2 = \frac{1}{\alpha_{cm}^2}\tilde{\nabla}^2 \, . \tag{3.13}$$

Furthermore, fields convert to inverse meters via

$$\phi = \frac{\tilde{\phi}}{\alpha_{cm}} \, . \tag{3.14}$$

It is sensible to write the two energy scales of the theory M and Λ around the Planck mass $M_{\rm PL}$ and the dark energy scale $\Lambda_{\rm DE}$ respectively. This allows for the problematic hierarchy between these scales to be absorbed into constant coefficients which are easier to handle numerically. As a result, the non-linear self interaction term in the field equation becomes

$$\frac{\Lambda^5}{\phi^2} = \left(\frac{\Lambda}{\Lambda_{\rm DE}}\right)^5 \frac{\Lambda_{\rm DE}^5 \, \alpha_m^2}{\tilde{\phi}^2}. \tag{3.15}$$

Further, the source term can be quoted [g cm^{-3}] by calling a second conversion factor α_g which links [g] to [GeV]

$$\alpha_g = 5.6095 \times 10^{23} \, \mathrm{g}^{-1} \, \mathrm{GeV} \, . \tag{3.16}$$

As a result of the above, one obtains that

$$\frac{\rho}{M} = \left(\frac{\alpha_{\rm g}\alpha_{cm}^{-3}}{M_{\rm PL}}\right)\tilde{\rho}\left(\frac{M_{\rm PL}}{M}\right) \, . \tag{3.17}$$

Collecting each of the above terms together, the field equation to be implemented into the finite element solver appears as

$$\tilde{\nabla}^2\tilde{\phi} = -\gamma_1\frac{\tilde{\Lambda}^5}{\tilde{\phi}^2} + \gamma_2\frac{\tilde{\rho}}{\tilde{M}}, \tag{3.18}$$

with

$$\begin{aligned} \tilde{\Lambda} &= \frac{\Lambda}{\Lambda_{\rm DE}} \, , & \tilde{M} &= \frac{M}{M_{\rm PL}} \, , \\ \gamma_1 &= \left(\Lambda_{\rm DE} \, \alpha_m\right)^5 = 3.3391 \times 10^8 \, , & \gamma_2 &= \frac{\alpha_{\rm kg}}{M_{\rm PL}} = 5.61 \times 10^5 \, . \end{aligned} \tag{3.19}$$

Calling a linear solver for the above problem involves recursively solving the linearised weak formulation of the chameleon field equation (Equation (3.11)) over a series of iterations. This strategy, referred to as Picard iteration or the method of successive substitutions, utilises a given solution ϕ_k to the linear problem from iteration k as the basis to search for an improved solution for iteration ϕ_{k+1}. The approach towards a converged solution following this method is shown in Figure 3.2 which displays the outcome of the finite element solver for a spherical source object within a vacuum chamber after 16 iterations. Initial conditions were set such that the field took the uniform value of $\phi_{\rm min}^{\rm (wall)}$ across the domain. Error estimation is handled for each iteration through the use of the vector norm $|\phi - \phi_k|$ which can be shown to relate to the residual $r = L(\varphi) - a(\phi_k, \varphi)$ where $L(\varphi)$ and $a(\phi_k, \varphi)$ are the semi-linear and bilinear forms respectively, as appearing in Equation (3.11). Typically objects with stronger curvatures require a greater number of iterations in order to reach convergence. The upper bound before terminating the solver was set at 30 iterations, where the convergence criteria specified residuals at the 10^{-6} level.

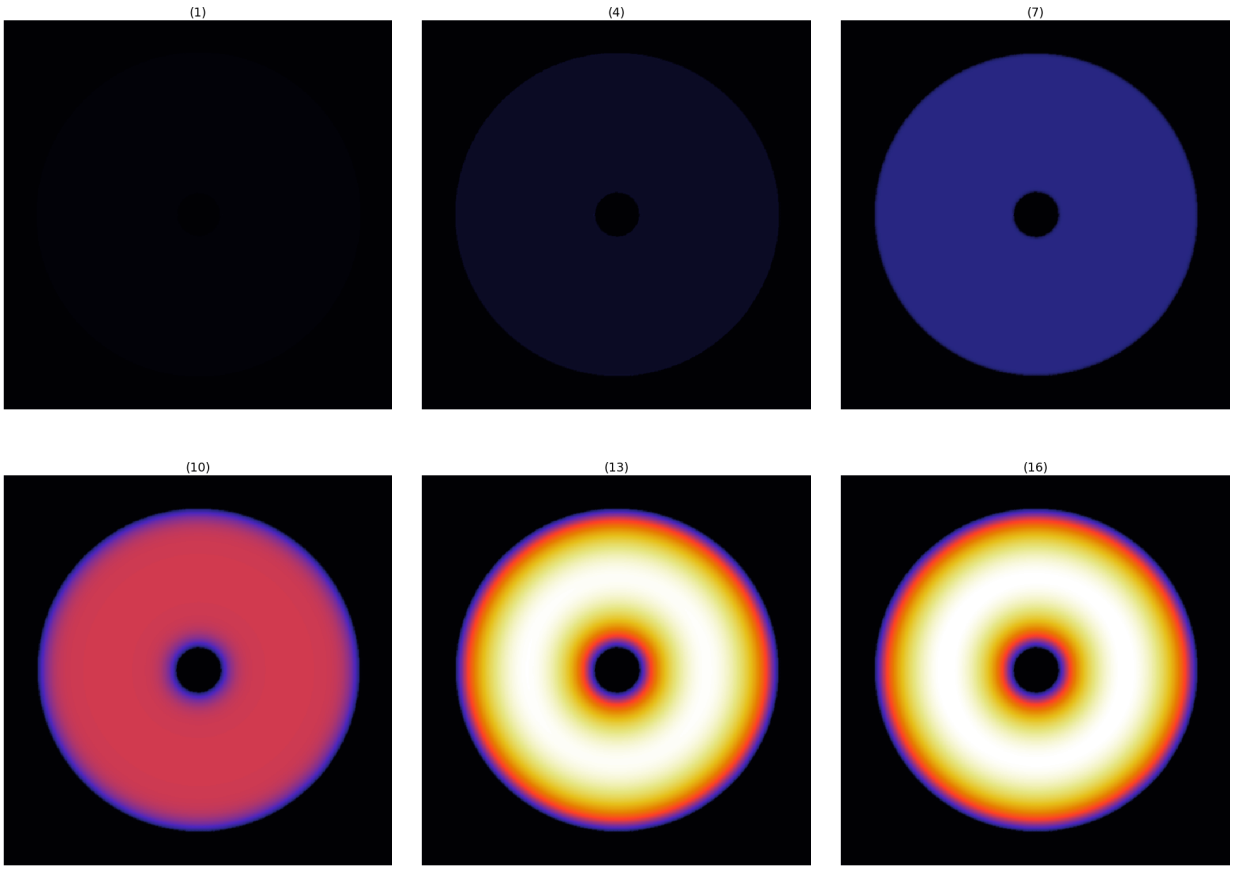

Figure 3.2: Figure capturing the convergence of the chameleon field for a spherical source within a vacuum chamber over 16 iterations, six of which have been displayed here with the iteration number specified at the top of each snapshot. The colour scheme here is normalised across figures, where the field moves between the source expectation value (black) and the chamber expectation value (white). The coloring in this case is following a linear interpolation scheme.

3.2.1 Finite Difference Integration

As an atom interferometry experiment is sensitive to the differences in atomic phase accumulated due to particles traversing different trajectories around a source, one of the aims of numerical simulations would be to map out these phase differences across the chameleon parameter space. For the spherical source, the problem greatly simplifies due to the force remaining approximately constant within the proximity of the experiment. It was mentioned in Chapter 1 that because of this, the action contribution to the phase difference vanishes and one is simply left with the contribution due to interactions with photons. This essentially reduces the task of calculating the phase difference to identifying the scalar accelerations within a specified region of the numerical grid. With more complex geometries however, this may not be sufficient. If the experiment leaves this regime, one is forced to perform a complete finite difference integration at the level of the action. This is generally calculated by evolving the two beam trajectories using a leapfrog algorithm. The classical action for a particle moving through a chameleon potential is given by

$$S = \int_0^T \mathrm{d}t \, \left\{ \frac{1}{2} \left(\dot{x}^2 + \dot{z}^2 \right) - \frac{\phi}{M} \right\} \, . \tag{3.20}$$

As previously this equation is built in units [GeV] which must be converted to inverse centimetres [cm^{-1}] to perform numerical integration. To deal with the conversion of the time coordinate, a third constant is invoked which has value

$$\alpha_s = 1.51925 \times 10^{24} \, \mathrm{GeV}^{-1} \, \mathrm{s}^{-1} \, , \tag{3.21}$$

which converts GeV back to seconds. Accordingly, the classical action can now be rewritten as

$$S = \int_0^{T_{[s]}} \mathrm{d}t_{[s]} \, \left\{ \delta_1 \left[\left(\frac{\partial x_{[cm]}}{\partial t_{[s]}} \right)^2 + \left(\frac{\partial z_{[cm]}}{\partial t_{[s]}} \right)^2 \right] + \delta_2 \frac{\phi_{[cm^{-1}]}}{\tilde{M}} \right\} \, , \tag{3.22}$$

where the constants δ_1 and δ_2 are given by

$$\delta_1 = \frac{\alpha_{cm}^2}{\alpha_s} \, , \qquad\qquad \delta_2 = \frac{1}{M_{\mathrm{PL}}} \frac{\alpha_s}{\alpha_{cm}} \, . \tag{3.23}$$

Thus after each time interval δt_{s}, the associated contribution to the action δS is given as follows:

$$\delta S = \left\{ \delta_1 \left[\left(\frac{\partial x_{[cm]}}{\partial t_{[s]}} \right)^2 + \left(\frac{\partial z_{[cm]}}{\partial t_{[s]}} \right)^2 \right] + \delta_2 \frac{\phi_{[cm^{-1}]}}{\tilde{M}} \right\} \delta t_{[\mathrm{s}]} \, . \tag{3.24}$$

3.2.2 Leapfrog Algorithm

The traditional leapfrog scheme involves evolving first order differential equations sequentially over each time-step. Firstly, the beam velocity $\dot{\phi} = \pi$ is moved forward a half-time step, using this to perform a full time-step iteration of the beam ϕ before bringing the velocity forward to a full time-step. Schematically, the algorithm can be described by the following procedure:

$$\pi_{\mathrm{n}+\frac{1}{2}} = \pi_{\mathrm{n}} + \frac{1}{2} \dot{\pi}_{\mathrm{n}} \delta t \, . \tag{3.25}$$

The field value is then iterated according to

$$\phi_{\mathrm{n}+1} = \phi_{\mathrm{n}} + \pi_{\mathrm{n}+\frac{1}{2}}\delta t \ , \tag{3.26}$$

and the velocity time-step is completed with

$$\pi_{\mathrm{n}+1} = \pi_{\mathrm{n}+\frac{1}{2}} + \frac{1}{2}\dot{\pi}_{\mathrm{n}+\frac{1}{2}}\delta t \ . \tag{3.27}$$

The chameleon force law can then be invoked to deal with the acceleration term via

$$\dot{\pi} = -\frac{\nabla\phi}{M} \ . \tag{3.28}$$

As previously, implementing this system for seconds and centimetres involves a rescaling of terms. In this case, the particle acceleration in simulation units is given by

$$\dot{\pi}_{[\mathrm{cms}^{-2}]} = -\frac{\gamma}{\tilde{M}}\frac{\partial\phi_{[\mathrm{cm}^{-1}]}}{\partial x_{[\mathrm{cm}]}}, \qquad \gamma = \frac{\alpha_{\mathrm{s}}^2}{\alpha_{\mathrm{cm}}^3 M_{\mathrm{PL}}} \ . \tag{3.29}$$

3.3 Force Scaling

The purpose of this section is to explore under what conditions, departures from a spherical source object would be a favourable choice for experimentation. The finite element solver was called for a number of source geometries across a range of model parameters M and Λ. Due to the convergence time associated with each run, mapping out the entire two-dimensional parameter space was out of reach within the allocated time frame. Instead, a number of slices were taken which involved fixing Λ and then studying how the chameleon profile varied across a range of choices for M. For the entirety of what is to follow, data was gathered for a vacuum chamber of radius $R_C = 15\,\mathrm{cm}$ where the width of the numerical domain was taken to be $W = 36\,\mathrm{cm}$. The volumes of all sources were normalised to that of a sphere with a radius of 2 cm. The objective here was to identify which source shape, if any, would lead to the tightest constraints on the chameleon parameter space. Furthermore, there was a question relating to whether these geometric effects were universal or were confined to regions of the parameter space where the field is screened, as indicated by the previous analytic study of the ellipsoid discussed in Chapter 2. Source geometries considered here were the sphere, torus, ellipsoid and cardioid. The torus was of great interest from a practical point of view due to being able to alleviate issues relating to the surface reflections of the laser pulses used to manipulate the atomic clouds. Here, pulses can be fired directly through the central cavity rather than tangential to the surface as would be the case for the simply connected geometries. In this case however, there is an ambiguity regarding where exactly along the central axis the interferometry experiment should be conducted. Unlike for the other sources, the existence of a local saddle point leads to a value of zero for the acceleration at the centre of the toroid. As depicted in Figure 3.1, scanning across the central axis of the torus allows one to identify the most ideal distance from the torus to perform an experiment. Importantly, with the exception of effects due to the finite size of the chamber, this distance

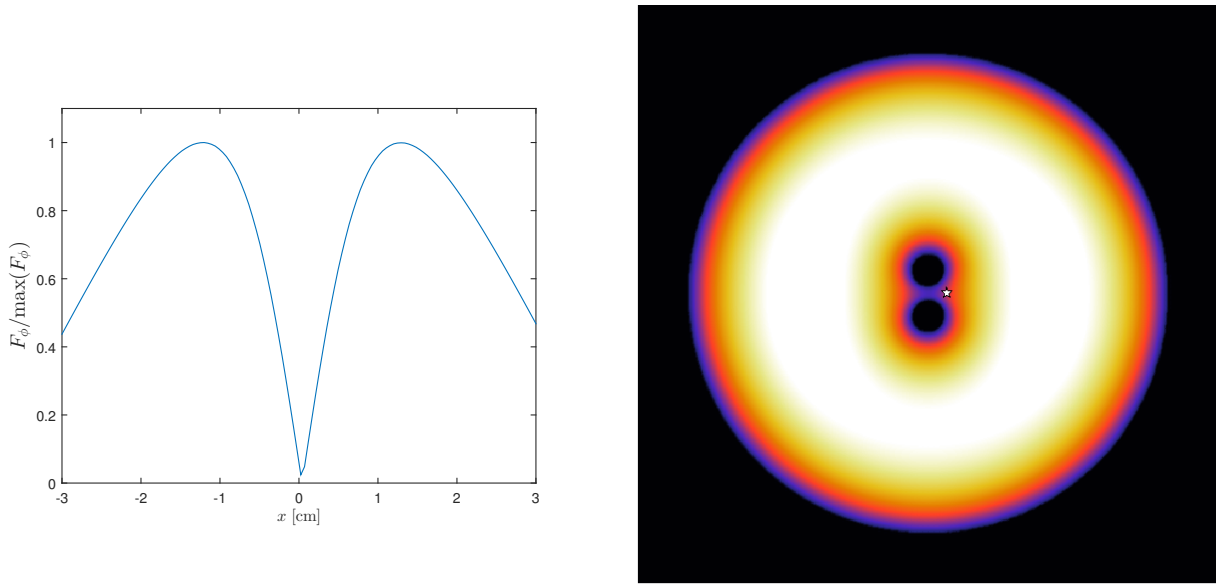

Figure 3.1: To the left is the variation of the chameleon force exerted by the toroid whilst moving along the central axis of rotation. The right displays a converged solution around a toroidal source, where the peak point of maximal acceleration is identified by the white star.

was found to be independent of the model parameters M and Λ. However, these finite size effects are not present within the window of parameter space of interest considered here. The inferred universality of the optimal distance from a torus to perform an experiment came from the fact that the exact scaling present in Figure 3.1 occurred for a very wide sample of parameter choices. Therefore, this value can be taken to remain constant for both the purposes of simulation and experiment.

The analytic work previously presented in Chapter 2 that the ellipsoid may be a favourable choice, especially when moving into the screened regime. However, the analytics only presented results normalised to the the gravitational force of the source, making it difficult to extract the important information (scalar accelerations) to make reference with a spherical source of the same mass. It was therefore sensible to solidify the inferences made in Chapter 2 by including the ellipsoid as part of the numerical study. The final source geometry under consideration was the cardioid described by work in Reference [114]. This is of particular interest for fifth force experiments due to it having the unique property of being an asymmetric geometry yet still sourcing a gravitational monopole. This novel feature could potentially be exploited when approaching Planck strength couplings for the chameleon field, where one would expect an asymmetric scalar field profile thus in principle making it possible to disentangle the two attractive forces. The results of this numerical work are displayed in Figure 3.2. It should be noted that outputs for the spherical case also provided a means to verify the numerical approach through comparison with the analytic results of Reference [64].

For several values of the self-interaction term Λ, the scaling of the scalar acceleration with the parameter M was studied for the various source geometries. One thing to notice is that

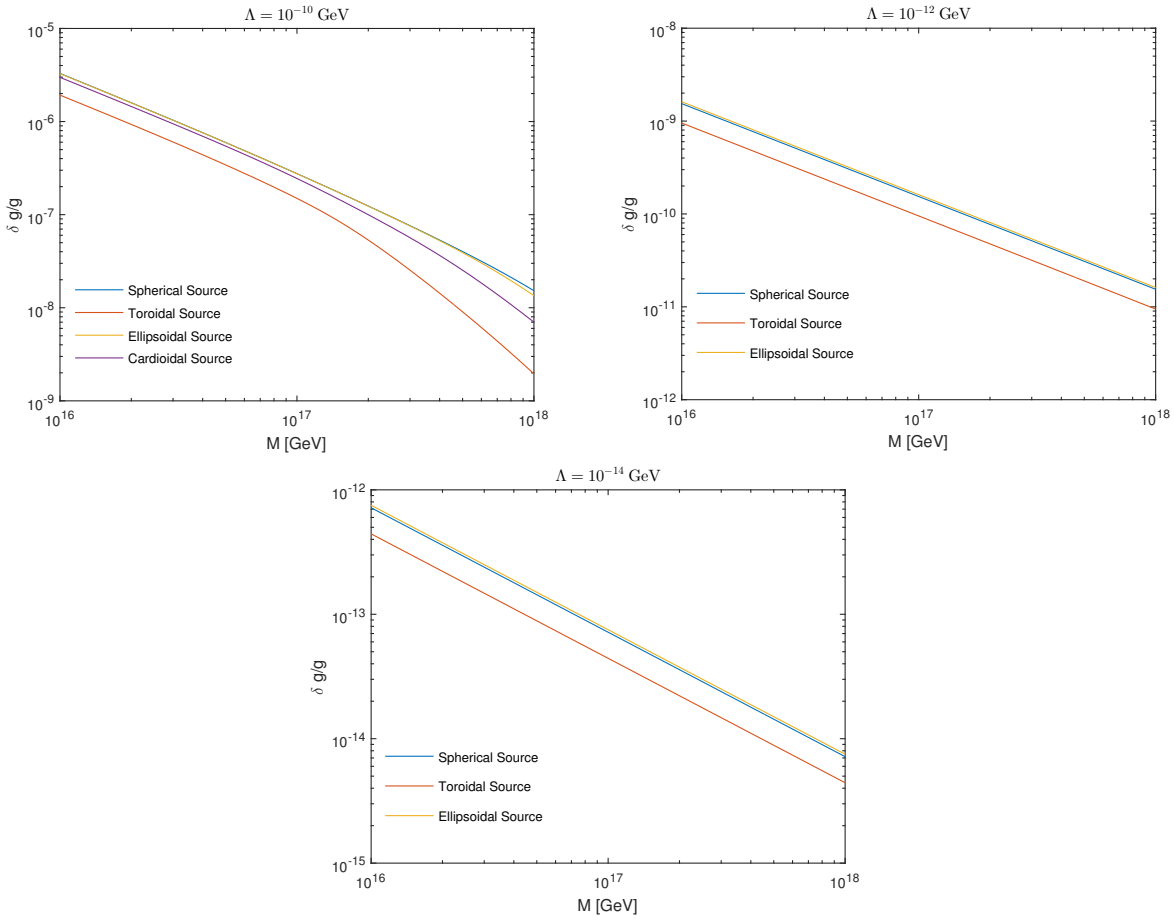

Figure 3.2: Figure displaying how the chameleon acceleration, normalised to the Earth's gravitational field g scales with model parameter M for three fixed values of Λ. Values of M lower than 10^{16} GeV have been omitted from the display as no additional structure is seen here. The scaling behaviour of the Cardioidal source was only accessible for $\Lambda = 10^{-10}$ GeV as a result of numerical instabilities.

only the range $10^{16} \leq M \leq 10^{18}$ GeV has been presented, as no additional structure was revealed for lower values of M. Furthermore, only one dissection of the parameter space was accessible for the cardioidal source (for $\Lambda = 10^{-10}$ GeV), which followed from a result of numerical instabilities. Specifically, the convexity of the object seemed to become an issue here which was ultimately a limitation of the mesh, a topic which is discussed in more detail in Section 3.4. For each of the scenarios, the toroid is found to produce the weakest acceleration across the entire range. One point to make here is that this issue could potentially be mitigated by tuning the inner radius of the torus, such as to reduce the size of the central cavity which would in turn magnify the attractive force. Data was gathered taking a conservative value of 0.5 cm for the inner radius, yet without full knowledge of the systematics at play here it is difficult to justify driving this parameter to a lower value. This could definitely be the focus of further work, although one would again need to take into consideration potential limitations of the grid if one were to shrink the inner cavity. One can see that for the ellipsoid (built with an ellipticity of $\xi = 1.01$), the story gets a little more interesting where it is observed to become the dominant source of acceleration when transitioning to lower values of Λ. Furthermore, if one were to dial the ellipticity ξ down to a value of 1.001 we would expect to see a greater enhancement of the chameleon acceleration over the spherical case.

The scaling behaviour observed for the ellipsoid is in full support of the previous analytic study of Chapter 2, which indicated that geometric enhancements would begin to surface as the effects of screening comes into play. In this case, the onset of screening becomes apparent when making the transition from $\Lambda = 10^{-10}$ GeV $\rightarrow 10^{-12}$ GeV, where accelerations now no longer exhibit differing logarithmic dependencies on M for different geometries. To bring some clarity to this remark, it is worth discussing how the structure of the scaling lines of Figure 3.2 relates to the chameleon screening. In essence, increasing M acts as to counter-act the thin-shell mechanism but at the same time inherently suppresses the force. For reference, this is most readily screen by examining Equations (1.43) and (1.45) that were derived to describe the screening of a spherical source in Chapter 1. Unique to each geometry, there is some critical value of M at which the shell region gets so expansive that the core region can no longer form, leading to an accelerated fall of in the force. This is the reason behind the tailing off of the lines as seen within the $\Lambda = 10^{-10}$ GeV example of Figure 3.2. Complementary to this behaviour, decreasing Λ drives the chameleon further into the screened regime, which is what restores the constant logarithmic scaling with M when moving from $\Lambda = 10^{-10}$ GeV down to the $\Lambda = 10^{-12}$ GeV level.

The final source under consideration was the cardioid, for which observations are limited to the scaling profile at the $\Lambda = 10^{-10}$ GeV level. For a sizeable portion of the range, the cardioid closely tails the spherical and ellipsoidal sources until the acceleration begins to fall off rapidly as we approach $M_{\rm PL}$. However, this behaviour is also displayed by the other sources amongst this stretch of parameters, although considerably less pronounced for the spherical and ellipsoidal cases. In this regime, the field does not have sufficient space to relax to the value minimising the effective potential. Thus, it makes sense that geometries with shorter distance scales begin to tail off sooner as they drive the central field minima to higher values, having a negative effect on the exerted force. For the case of the cardioid, it

is difficult to ascertain the viability for experimental application here. One could argue that any potential means of exploiting the asymmetry of the field profile would likely be negated by the relative deficit in acceleration when compared to other sources.

3.4 Shape Optimisation

The strategy for identifying the optimal geometry for a source object within an Atom Interferometry experiment was to construct a series of shapes using the Legendre polynomials as a basis. A range of series coefficients can be tested as a means to compare different source geometries. Without computational limitations, the optimal source could be identified by performing some form of annealing routine on objects defined by an arbitrarily large number of Legendre terms. However, due to the time and resource limitations, in this work, a sample space of approximately one hundred randomly generated objects will be used for analysis. Furthermore, only the first four Legendre polynomials will be used in the expansion.

3.4.1 Setting the Shape Parameters

In order to make direct comparisons, it is important to ensure that the masses of the source objects forming the test space are pinned to a common value. As the shape generation procedure is to involve an expansion of Legendre polynomials, this will therefore constrain the values of the series coefficients available for selection when building the sample pool. Dealing with sources of a constant density, this translates to normalising the usual volume integral in spherical polar coordinates:

$$V = \int r^2 \sin(\theta)\, \mathrm{d}r\mathrm{d}\theta\mathrm{d}\varphi \,, \tag{3.30}$$

noting that the limits of the radial coordinate inherit an angular dependence for objects defined in this way. Performing the simple integrals over r and φ the above becomes

$$V = \frac{2\pi}{3} \int_0^{\pi} R^3(\cos(\theta))\sin(\theta)\, \mathrm{d}\theta \,, \tag{3.31}$$

where the radial component expands as

$$R(\cos(\theta)) = \sum_i a_i P_i\left(\cos(\theta)\right) \ . \tag{3.32}$$

Thus the exact geometry of our source is specified completely by the values of the coefficients a_i. To keep the problem numerically tractable, for optimisation over sensible timescales, only coefficients a_0 to a_3 will be considered here. At this point it is sensible to perform a change of variables $x = \cos(\theta)$ such that

$$V = \frac{2\pi}{3} \int_{-1}^{1} \left(\sum a_i P_i(x)\right)^3 \mathrm{d}x \,. \tag{3.33}$$

Using the trinomial expansion formula on Equation (3.33), set to terminate at $i = 3$, one obtains

$$\begin{aligned} V = \frac{2\pi}{3}\int_{-1}^{1} \big\{ & a_0^3 + a_1^3 P_1(x)^3 + a_2^3 P_2(x)^3 + a_3^3 P_3(x)^3 + 3a_0^2\left(a_1 P_1(x) + a_2 P_2(x) + a_3 P_3(x)\right) \\ & + 3a_1^2 P_1(x)^2\left(a_0 + a_2 P_2(x) + a_3 P_3(x)\right) + 3a_2^2 P_2(x)^2\left(a_0 + a_1 P_1(x) + a_3 P_3(x)\right) \\ & + 3a_3^2 P_3(x)^2\left(a_0 + a_1 P_1(x) + a_2 P_2(x)\right) + 6a_0 a_1 a_2 P_1(x) P_2(x) + 6a_0 a_2 a_3 P_2(x) P_3(x) \\ & + 6a_1 a_2 a_3 P_1(x) P_2(x) P_3(x) + 6a_0 a_1 a_3 P_1(x) P_3(x)\big\}\ \mathrm{d}x\ . \end{aligned} \tag{3.34}$$

Fortunately, half of these terms vanish immediately due to the odd parity of the integrands. This leaves the following to be calculated:

$$\begin{aligned} V = \frac{2\pi}{3}\int_{-1}^{1} \big\{ & a_0^3 + a_2^3 P_2(x)^3 + 3a_0^2 a_2 P_2(x) + 3a_0 a_1^2 P_1(x)^2 + 3a_1^2 a_2 P_1(x)^2 P_2(x) \\ & + \ 3a_0 a_2^2 P_2(x)^2 + 3a_3^2 a_0 P_3(x)^2 + 3a_2 a_3^2 P_2(x) P_3(x)^2 \\ & + \ 6a_1 a_2 a_3 P_1(x) P_2(x) P_3(x) + 6a_0 a_1 a_3 P_1(x) P_3(x)\big\}\ \mathrm{d}x\ . \end{aligned} \tag{3.35}$$

Two useful formulas can be invoked to systematically deal with each term in the above, these are

$$\int_{-1}^{1} P_n(x)\,\mathrm{d}x = 0 \ \ (n \geq 1)\ , \qquad \int_{-1}^{1} P_m(x) P_n(x)\,\mathrm{d}x = \frac{2}{2n+1}\delta_{nm}\ . \tag{3.36}$$

The complete result is then

$$V = \frac{2\pi}{3}\left[2a_0^3 + 2a_0 a_1^2 + \frac{6}{5}a_0 a_2^2 + \frac{6}{7}a_0 a_3^2 + \frac{4}{35}a_2^3 + \frac{4}{5}a_1^2 a_2 + \frac{24}{105}a_2 a_3^2 + \frac{36}{35}a_1 a_2 a_3\right]\ . \tag{3.37}$$

The mass contained within these volumes will be set equal to that of a sphere of radius r_{EFF}. This requires the following to be satisfied:

$$r_{\mathrm{EFF}}^3 = a_0^3 + a_0 a_1^2 + \frac{3}{5}a_0 a_2^2 + \frac{3}{7}a_0 a_3^2 + \frac{2}{35}a_2^3 + \frac{2}{5}a_1^2 a_2 + \frac{12}{105}a_2 a_3^2 + \frac{18}{35}a_1 a_2 a_3\ . \tag{3.38}$$

The above is cubic in a_0 and a_2, and quadratic in a_1 and a_3. Values of $a_0 \to a_3$ are to be picked sequentially from a uniform distribution. In this case, the upper limit for a given choice is obtained by imposing that all subsequent coefficients vanish. The most sensible picking order seems to be $a_0 \to a_1 \to a_3 \to a_2$, which ensures that the cubic equation is left until the end. This therefore presents the following ranges when sampling our coefficients:

$$\begin{aligned} & 0 \leq a_0 \leq r_{\mathrm{EFF}}\ , \\ & 0 \leq a_1 \leq \sqrt{\frac{r_{\mathrm{EFF}}^3 - a_0^3}{a_0}}\ , \\ & 0 \leq a_3 \leq \sqrt{\frac{7}{3}\left(\frac{r_{\mathrm{EFF}}^3}{a_0} - a_0^2 - a_1^2\right)}\ . \end{aligned} \tag{3.39}$$

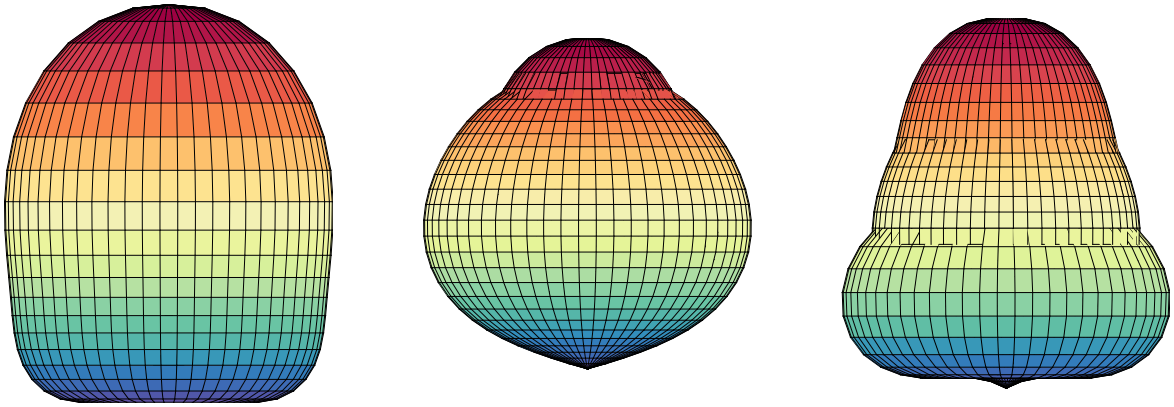

Figure 3.1: Example geometries built using a four term Legendre Series.

The remaining unknown a_2 can be found by solving the following cubic polynomial:

$$\frac{2}{35}a_2^3 + \frac{3}{5}a_0a_2^2 + \left(\frac{2}{5}a_1^2 + \frac{12}{35}a_3^2 + \frac{36}{35}a_1a_3\right)a_2 + \left(a_0^3 + a_0a_1^2 + \frac{3}{7}a_0a_3^2 - R_{\text{EFF}}^3\right) = 0\,. \quad (3.40)$$

3.4.2 Finding the Optimal Source Geometry

Following the scheme just outlined in Section 3.4.1, it is possible to seed arbitrarily generated source objects whilst ensuring that their masses remain constant over the sample space. For each source generated in this way, the finite element solver is then called to solve for the associated chameleon field within the vacuum chamber. As one is now dealing with asymmetric field profiles, an optimisation algorithm was implemented to identify the most favourable position to perform the experiment. This involves scanning the converged solution at some pre-set distance from the surface (taken to be 5 millimetres to conform with experimental targets) in order to identify the location exhibiting the greatest acceleration.

a_0	a_1	a_2	a_3	$\delta g/g$
0.82	0.02	0.85	3.94	$4.82 \cdot 10^{-11}$
0.97	0.59	0.03	3.99	$4.68 \cdot 10^{-11}$
0.97	0.59	0.03	3.99	$4.65 \cdot 10^{-11}$
1.34	0.18	0.41	2.89	$4.52 \cdot 10^{-11}$
1.47	0.19	0.27	2.63	$4.47 \cdot 10^{-11}$
2	0	0	0	$1.73 \cdot 10^{-11}$

Table 3.1: The correction to the Earth's gravitational acceleration for a range of sources built using a Legendre expansion for parameters $M = 10^{18}$ GeV and $\Lambda = 10^{-12}$ GeV. The first five entries correspond to the greatest accelerations returned from the sample pool. The final entry corresponds to the spherical result.

Outputs following this routine have been tabulated as shown in Table 3.1. It can be seen

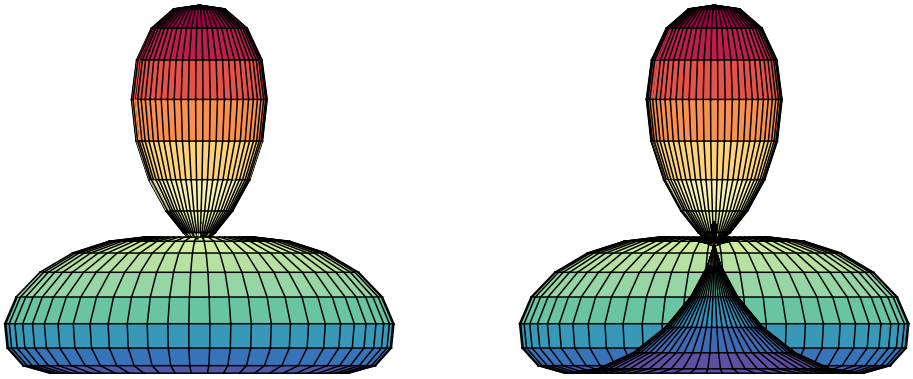

Figure 3.2: Three dimensional display of the optimal source object extracted from the sample pool. To the left is an external view of the source whereas to the right is a view of a cross section obtained by slicing the object in half. Colours here simply scale with the z coordinate which aids in visualisation.

that considerable gains over the spherical source can be realised even with a relatively limited range of test geometries. For the optimal source presented in Figure 3.2, it seems that performing the experiment near the tail regions seems to be the most beneficial, as seen in Figure 3.3. One possible reason for this could be the choke-point connecting these lobes to the main body, this could act to drive the field out of the interior vacuum value, essentially decoupling the adjacent regions. In a sense this could act to prevent the formation of a 'core' region within the source, essentially combating the screening effect. This lends itself to the idea that outside of the screened regime, where all mass contributes to the chameleon force, the sphere is the ideal source object, but loses favour when screening comes into play. At this point, the nature of the internal field structure seems to favour shorter length scales. It then makes sense why a source which is almost partitioned into three separate regions would come to source the greatest chameleon acceleration.

Following this logic, outside of the screened regime the sphere is expected to exert the greatest chameleon force, but as screening comes into effect the existence of internal structure seemingly favours objects which partition into smaller ones, leading to crossover at some point within the parameter space. As long as this crossover occurs before entering the region of the parameter space of interest, it would definitely be beneficial to consider such sources for experimentation, assuming that systematics could be controlled. It should be noted that this is only a preliminary comparison to the spherical reference object. One has to accept that this corresponds to the optimal configuration for a given set of model parameters $M = 10^{18}$ GeV and $\Lambda = 10^{-12}$ GeV and may not hold true for a practical portion of the unconstrained parameter space. Ideally, a complete scan of the parameter space would have to be performed. However, for this complex geometry with the current means of data acquisition, both convergence and numerical stability became problematic so this would require further treatment.

An attempt of sweeping across a cross section of the parameter space for $\Lambda = 10^{-10}$ GeV

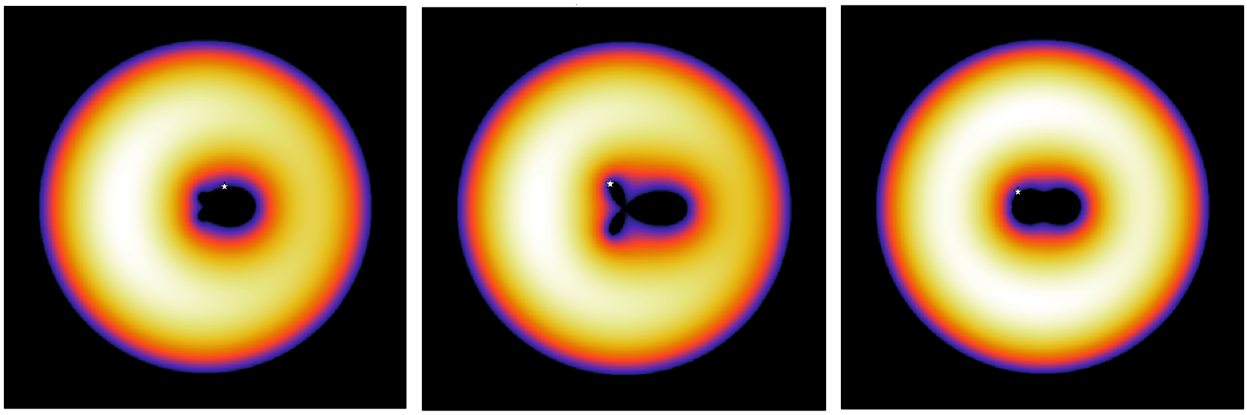

Figure 3.3: Scalar field profiles in the (x, z) plane for three of the source objects generated by the procedure discussed in Section 3.4.1. The field ranges between the source expectation value (black) and the vacuum expectation value (white). The central figures corresponds to that leading to the greatest acceleration. For each of the sources, the optimal location for the chameleon force is signified by the small white star.

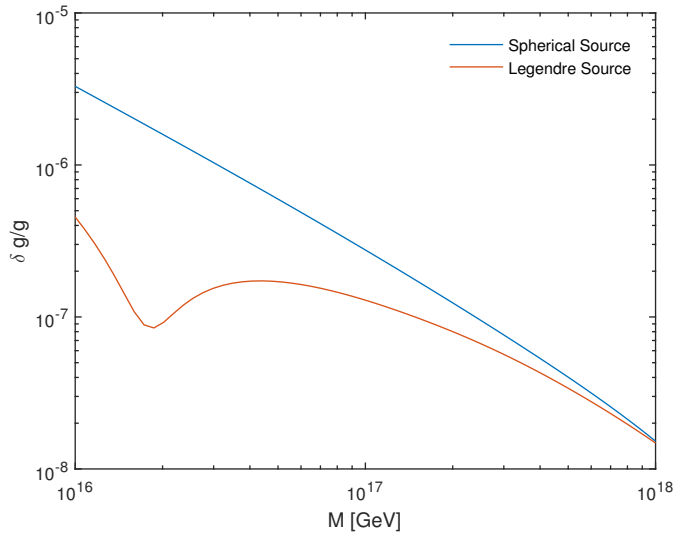

Figure 3.4: Comparison of how the chameleon acceleration, normalised to the Earth's gravitational field g scales the with value of the parameter M for a spherical source object and the optimal source achieved using a Legendre basis, as described in Table 3.1. This data was gathered for $\Lambda = 10^{-10}$.

is displayed in Figure 3.4. There is clearly some peculiar behaviour here for lower values of M, where the optimal source from Table 3.1 only comes to dominate as one hits Planck strength coupling. At this point, it is difficult to ascertain whether or not this behaviour is a result of numerical errors or a deeper level of chameleon phenomenology. For lower values of M, convergence was not met within the upper limit of iterations, requiring some relaxation on the convergence criteria. Typically, this only slightly compromises the accuracy of the data but there may be greater sensitivity for such a complex source. Time considerations at this point make it difficult to perform simulations at higher resolutions, suggesting that we have reached the limits of the uniform grid for this work. Fortunately, further gains in numerical precision and stability can be achieved through an appropriate reallocation of computational resources, refining the mesh in regions of significant variations in the density field whilst preserving a coarse grid for regions where the field varies more gradually. This becomes particularly important when dealing with objects containing pinch points such as that at the center of the source considered here, as can be seen in Figure 3.2.

Mesh Refinement

The benefits of performing simulations on a refined grid can be two-fold. Not only can we use refinement to more efficiently utilize computational power (such as to focus resources towards the areas where the field is expected to vary rapidly) thus reducing net simulation time, it can be also be used as a means to handle the numerical stabilities that typically arise when dealing with more complex source geometries. Of course, these outcomes are generally coupled; the areas inciting numerical instabilities tend to be where the field exhibits stronger variations, making them target spaces for a finer mesh structure. Intuition from previous analytic calculations tells us that most of the variations of the chameleon field are typically confined to a shell region of order the fields Compton wavelength λ_ϕ, around the discontinuity in the density field. This is used, as the basis to build a mesh refinement algorithm. Within this shell region, this field varies approximately linearly. Given that the finite element solver builds the solution around linear basis functions,[6] one can consider the mesh to be adequate once the size of the cells/elements at the boundary become smaller than the Compton wavelength of the field. At this point, one should be able to accurately resolve these essential variations of the scalar field. For higher values of M and lower Λ, this would become hugely problematic for a non-refined mesh as this value becomes incredibly small. As a result, one would expect to require an astronomically high uniform resolution before reaching a mesh independent solution. Below this threshold, numerical instabilities would enter as a result of the uniform mesh being unable to adequately resolve field variations across the appropriate length scales.

The implementation of the mesh refinement routine is depicted by Figure 3.5, which captures the first two iterations of the refinement algorithm. In practice, the refinement process continues for further iterations (parameters M and Λ dependent) but these additional stages are almost impossible to distinguish visually. Note that the use of the vector norm $|\phi - \phi_k|$ in assessing convergence becomes inadequate here due to the lack of weighting which one would require for a non-uniform mesh. Instead of dealing with a global sum such as the

[6] However, higher order polynomial elements can also be specified, resulting in an increase in computational complexity as a trade-off for greater accuracy.

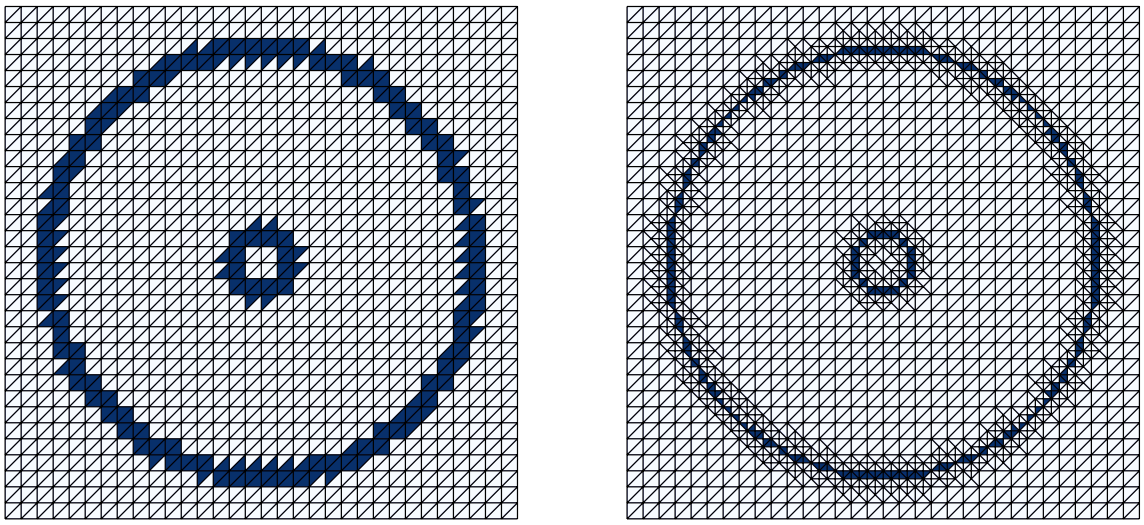

Figure 3.5: Figures moving left to right displaying the first two iterations of the mesh refinement algorithm. At each stage, the cells flagged for refinement have been shaded in blue.

residual (which was mentioned previously to relate to the vector norm), it was found to be more effective to monitor values locally. In particular, this meant focusing on the relative corrections to the solution obtained with each iteration at a given point. This point was chosen to lie within the region of which the experiment would be performed, as ultimately, this was the point for which results were extracted. This way, although the global vector norm tended to vary with different source geometries (making it difficult to define a more general criteria of convergence following this scheme), establishing the convergence at a particular point was found to yield consistency across all geometries. Similar to the previous criteria, convergence was met when successive corrections in the target area fell below the 10^{-5} level.

The outcome of the mesh refinement scheme for a variety of source objects is displayed in Figure 3.6. It can be seen that this approach allows for a relatively coarse mesh structure in regions where long wavelength field variations are expected whilst confining the finer resolutions to areas where the converse is true. This essentially allows one to realize a considerable gain in accuracy for the same number of simulation nodes when compared to the uniform counterpart. The most tangible way to capture the benefits of local mesh refinement comes from performing a mesh dependence study for both mesh structures. The study involves systematically reducing the simulation element size to identify how the accuracy of the solution responds to the simulation size. In addition to convergence defined within the solver, this introduces the idea of mesh convergence. As we allocate more computational resources to a problem, we expect to recover a greater approximation of the continuous solution. However, beyond a certain point, diminishing returns will begin to enter and the displacement of the solution from successive refinement will fall below some level of precision. Hitting this threshold

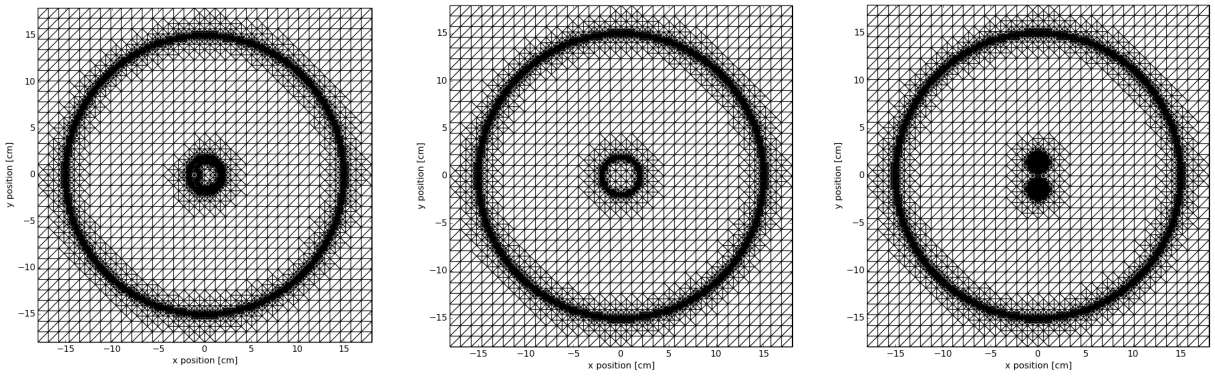

Figure 3.6: Figure demonstrating the scaling behaviour of the uniform and refined meshes for difference simulation resolutions (tied to the time to convergence). The refined mesh quickly reaches a mesh independent solution. In comparison, even the larger grid resolutions studied for the uniform mesh fail to realise mesh independence.

defines a state of mesh independence, the simulation is said to have entirely converged and no additional features of the solution can be revealed by increasing the complexity of the mesh. This essentially then allows one to establish the balance between performance and accuracy, allowing one to run the solver on the optimal mesh and avoiding excessive computation times.

The performance differences between both implementations are captured by Figure 3.7 which presents the scaling behaviour of relative acceleration with simulation time. For the uniform mesh, data was gathered from the solver running 128^2, 256^2, 512^2 and 1024^2 simulation nodes. Due to the additional nodes generated following the refinement scheme, an additional base resolution of 64^2 nodes was included for the refined case. This is because the time-scale turned out to be comparable to the lowest sample for the uniform grid. The most important observation here is that the refined problem appears to reach mesh convergence for as little as 128^2 base nodes, which places simulation times at just below one minute. Above this resolution, it seems that no additional accuracy is to be gained. To contrast, the uniform mesh fails to realize mesh independence across the sample space, with sizeable corrections still entering even with the transition from 512^2 to 1024^2 simulation nodes. Furthermore, even extending up to the 1024^2 case, the result fails to lie within the proximity of even the more conservative examples for the refined mesh, suggesting even higher resolutions would be required to reach mesh convergence for this set-up. It should be noted that data for both scenarios was gathered for a spherical source object within the vacuum chamber. This avoids any stability issues, allowing one to focus purely on simulation efficiency - taking only time considerations into account. Unfortunately, time limitations prevented full implementation of local mesh refinement for the purposes of data acquisition. However, the performance benefits presented in this section highlight the method of local mesh refinement as a clear step forward in efforts to map out the entire two-dimensional chameleon parameter space in manageable simulation times, in addition to unlocking the study of more complex geometries. Furthermore, in choosing to scan the parameter space perturbatively, it would

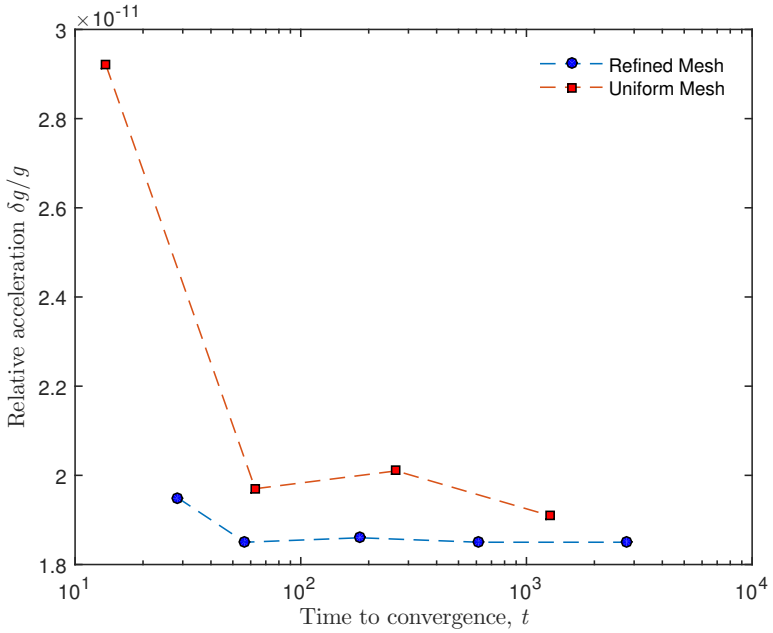

Figure 3.7: Figure demonstrating the scaling behaviour of the Uniform and Refined meshes for difference simulation resolutions (tied to the time to convergence). The refined mesh quickly reaches a mesh independent solution. In comparison, even the larger grid resolutions studied for the uniform mesh fail to realise mesh independence.

be possible to significantly reduce the number of iterations required until convergence by injecting the solution from the preceding choice of parameters as the initial conditions for the iterative solver. Coupling this with parallelisation, constraining the chameleon parameter space numerically for arbitrary experimental set-ups using a finite element solver should become attainable within the near future.

Summary

This chapter has focused on the implementation of a finite element scheme in order to develop a better understanding of how the chameleon force responds to the geometry of the source. It has been shown that there are a number of inviting alternatives to the typical spherical source object, based on their ability to exert a stronger scalar attraction when moving into the screened regime of the model parameter space. This has promising applications within an atom interferometry experiment, as the remaining parameter space to be explored corresponds to the window for which shape enhancement effects begin to manifest. There was also treatment of a toroidal source object, which was noted to be preferred from an practical perspective. This preference came from the fact that systematic errors associated with optical surface reflections can be avoided by performing an atom interferometry experiment on the central axis of the toroid. However, it was shown that for the example used, the decrease in the level of chameleon attraction was too substantial to justify the switch to the toroidal source.

As a more general note, the reach of the finite element implementation extends far beyond the application presented here. It is relatively easy to adapt the program to accommodate alternative experimental configurations, and it has also been demonstrated that working on an unstructured grid unlocks vast opportunity for increased computational efficiency through the local refinement of the simulation mesh. This allows for a targeted allocation of computational resources which has a huge positive impact on convergence times. As a result, application of this work to other studies focusing on the numerical treatment of the chameleon such as in Reference [110] should see considerable improvements in both accuracy and simulation time. The flexibility of this approach, being able to also incorporate the symmetron and dilaton fields, across a host of experimental setups, makes it essentially a universal tool that could be used in future work attempting constrain screened dark energy models across the current generation of lab based experiments.

3.A Finite Elements and the Symmetron

In principle, repeating the above analysis for the case of the symmetron field should be as straight-forward as inputting the appropriate linear and bilinear forms used within the solver. As an advantage over the chameleon, one does not have to worry about divergences arising from the inverse power law term within the effective potential. However, if the plan is to avoid the topological defects arising as a result of the spontaneously broken $\mathbb{Z}_2$ symmetry, one would have to take a little more care with the initial conditions to ensure that the solver converges at the global and not local minima. Nevertheless, the equation of motion for the symmetron is given by

$$\nabla^2\phi = \phi\left\{\left(\frac{\rho}{M^2} - \mu^2\right) + \lambda\phi^2\right\} \ . \tag{3.41}$$

Writing this differential equation in its variational form following the previous prescription leads to the result

$$\int_\Omega \phi\left\{\left(\frac{\rho}{M^2} - \mu^2\right) + \lambda\phi^2\right\}\varphi + \int_\Omega \nabla\phi\cdot\nabla\varphi = 0 \ , \qquad \forall\varphi \ . \tag{3.42}$$

As the first entry in the above is already linear in ϕ, one only has to worry about linearising the cubic self interaction term. This modifies the variational form into

$$\int_\Omega \left[\phi\left\{\left(\frac{\rho}{M^2} - \mu^2\right) + 3\lambda\phi_k^3\right\}\varphi + \nabla\phi\cdot\nabla\varphi\right] = \int_\Omega 2\lambda\phi_k^3\varphi \ , \qquad \forall\varphi \ . \tag{3.43}$$

The Dirichlet boundary conditions again can be set as the expectation value of the field within the chamber walls. In this case, as the density field is sufficiently high to restore the $\mathbb{Z}_2$ symmetry, this corresponds to imposing a field value of zero at the edges of the simulation domain.

3.B Setting up the Torus

A torus can be built by performing a full rotation of a circle of radius a and distance R from the axis of rotation. The parameters a and R describing the torus are known as the minor and major radii respectively. Writing the problem in a cylindrical coordinate system (x, y, θ), the volume integral is set-up as

$$V = 2\pi \int_{x_{\min}}^{x_{\max}} \int_{y_{\min}}^{y_{\max}} x \, \mathrm{d}x\mathrm{d}y \quad \begin{cases} \{x \in \mathbb{R} | \, (R-a) \leq x \leq (R+a)\} \\ \left\{ y \in \mathbb{R} | -\sqrt{a^2 - (x-R)^2} \leq y \leq \sqrt{a^2 - (x-R)^2} \right\} \end{cases} , \tag{3.44}$$

where the rotational symmetry of the torus has already been incorporated into the above to deal with the integral over the azimuthal angle θ. The bounds placed on the y-coordinate follow from the relation $(x-R)^2 + y^2 = a^2$. Integrating over y leads to

$$V = 4\pi a \int_{x_{\min}}^{x_{\max}} 2x \sqrt{1 - \left(\frac{x-R}{a} \right)^2} \, \mathrm{d}x \, . \tag{3.45}$$

Introducing the substitution $\bar{x} = (x-R)/a$ simplifies the problem as

$$V = 4\pi a^2 \int_{-1}^{1} (a\bar{x} + R) \sqrt{1 - \bar{x}^2} \, \mathrm{d}x = 4\pi a^2 R \int_{-1}^{1} \sqrt{1 - \bar{x}^2} \, \mathrm{d}x \, , \tag{3.46}$$

where the final equality follows from eliminating the term containing the odd integrand. The above is then easily solved through the change of variables $\bar{x} = \sin(t)$ to arrive at an expression for the volume of the torus. In choosing to normalise this to the volume of a reference spherical source object, an effective radius R_{EFF} is introduced such that

$$\frac{4\pi}{3} R_{\mathrm{EFF}}^3 = 2\pi^2 a^2 R. \tag{3.47}$$

Thus for a given effective radius of a source, one must find a sensible pairing of R and a. In order to maximise the axial acceleration within an atom interferometry experiment, the size of the interior hole $R-a$ should be kept to smaller values whilst leaving enough space for the Raman pulses to freely propagate. Using a crude back of the envelope approximation for an atomic cloud falling at $5\,\mathrm{cms}^{-1}$ over a runtime of $T = 30\,\mathrm{ms}$, ensuring that the experiment remains within the scope of the central cavity places a theoretical lower limit of 1.5 mm on the value of $R - a$. However, this calculation neglects effects due to a finite cross section of the incident laser pulse. Therefore for the purposes of data acquisition, this quantity was taken with the conservative value of 0.5 cm. Having specified the size of the central cavity, Equation (3.46) can be used to calculate the required major radius R in order to meet the volume targets. Let $R - a = \Delta$, then Equation (3.46) leads to a cubic equation to be solved for the unknown R

$$R^3 - 2\Delta R^2 + \Delta^2 R - \frac{2R_{\mathrm{EFF}}^2}{3\pi} = 0 \, , \tag{3.48}$$

which is readily dealt with numerically.

Chapter 4

A Proposed Experimental Search for Chameleons using Asymmetric Parallel Plates

The fact that the chameleon theory has been designed to suppress the associated fifth-force in dense environments, means that it could in principle be detected in a suitably designed laboratory experiment in high vacuum. Recent years have seen a wealth of experiments formulated for or appropriated to the detection of light scalar fields, reaching far into previously unconstrained regions of the theory parameter space utilising atom interferometry [40, 64, 83], cold neutron experiments [85, 86, 109, 116] and searches for Casimir-like forces [117, 118]. The remaining parameter space includes the chameleon theories that are most weakly coupled to matter, making them intrinsically harder to detect. However, moving into this segment of the parameter space also results in stronger manifestations of the non-linearities within the theory. Not only this, but even with the coupling strength M several orders of magnitude below the Planck scale $M_{\rm PL}$, screening drives the chameleon into becoming sub-dominant with respect to the gravitational force. Therefore, a means to disentangle the chameleon and gravitational interactions could help to take these limits even further. This ultimately raises an important question: can the current generation of fifth force experiments be appropriated to take advantage of the features induced by these non-linearities. As demonstrated for the example of an ellipsoidal source geometry, the answer to this question is yes: in moving away from the spherical source, not only can the magnitude of the exerted chameleon force increase, but the gravitational element also diminishes.

A number of the experiments amongst this wave of fifth-force searches make use of a parallel plate configuration to source the scalar field. Such an example are Casimir force experiments experiments which aim to measure the attractive force between the two plates. It is natural to question whether or not the parallel plate configuration can find a place within atom interferometry experiments. In this case, the scenario would slightly change as the focus would shift to studying the trajectories of particles moving between the plates rather than the attraction between them. In the conventional parallel plate setting, the density of the

two plates is kept the same and as a result, the gravitational component is removed from the problem. Accordingly, parallel plates can serve as a means to isolate the fifth-force. However, this symmetry also means that the chameleon force between finds an equilibrium position exactly half-way in-between them. In this case, the interaction strengths appearing within the configuration would be severely limited by the cancellations between the two competing plates. Fortunately, this is where the non-linear aspects of the theory become useful. In the screened regime of the parameter space, the chameleon force depends intrinsically on the plate density, becoming independent of the total mass of the plate. For planar objects, this is in contrast to the gravitational interaction which is controlled entirely by the mass of the source. Therefore, by making adjustments to the respective density fields of the parallel plates whilst maintaining their overall masses, the chameleon field could potentially be optimised for detection without having to reintroduce gravity back into the problem. Taking these ideas into account, this chapter will describe a novel parallel plate set-up,where the two plates have different densities but the same total mass. As is common in the treatment of parallel plates, the relevant quantity is actually the mass per unit area when working in the idealized picture where the plates are of infinite spatial extent. The target of this work was to study this configuration within the context of an atom interferometry experiment. Throughout the analysis, the masses of the individual plates were kept equal to ensure the symmetry of the gravitational field. It was found that introducing a density contrast feeds directly into an asymmetry for the chameleon field. Importantly, this asymmetry was then shown to lead to an enhancement of the chameleon presence within the experiment, with the additional advantage of removing the gravitational background.

The structure of this chapter is as follows: Section 4.1 will recap the key ingredients of the chameleon theory. The solution of the chameleon field profile between asymmetric plates will then be discussed, which will be broken down into two components: Section 4.2.1 will see the acquisition of the solution following a purely analytic approach, and Section 4.2.2 following a method which calls for numerical implementation. The potential of this configuration in the context of atom interferometry will then be covered in Section 4.3, followed by a brief summary of the findings of this work in Section 4.4.

Prior to the work presented in this chapter, analytic calculations of the chameleon field between two parallel plates relied on taking the strong coupling limit to fully specify the system [85, 116]. This corresponds to the regime of parameter space such that $M/M_{\rm PL} \leq 10^{-5}$ which is considerably more restrictive than the results presented to follow. Furthermore, this is the first calculation allowing the densities of the plates to differ. Therefore, the hope is that the results presented could be utilized for other similar fifth-force searches which utilise a parallel plate configuration, such as the bouncing neutron and casimir-force experiments.

4.1 The Chameleon Theory

I will begin by reminding the reader of the important aspects of the chameleon theory. Namely, when matter can be described as a static, non-relativistic perfect fluid, the behaviour

of the chameleon field is governed by an effective potential:

$$V_{\mathrm{EFF}}\left(\phi\right) = \frac{\Lambda^5}{\phi} + \frac{\rho\phi}{M}\,, \tag{4.1}$$

where ρ is the local energy density of matter. The model admits two energy scales M and Λ controlling the coupling to matter and self-interaction strengths respectively. The energy scale Λ controls the self interactions of the scalar. The scale M is constrained, by precision measurements of atomic structure and searches for fifth forces [75, 104, 105] to lie in the range $10^4\ \mathrm{GeV} \leq M \leq M_P \sim 10^{18}\ \mathrm{GeV}$. Through the connection to dark energy and the increasing expansion rate of the universe, Λ is expected to be of order 1 meV [13], while Casimir force measurements indicate $\Lambda < 100\,\mathrm{meV}$ [104–106]. Additional constraints also arise from astrophysical observations, in particular measurements of the period luminosity relation of Cephid variable stars [119] and comparing the rotation curves of main sequence stars with those of diffuse gas [120], however for the chameleon model considered in this work these observations are less constraining than terrestrial experiments. Given these constraints we take $10^{-2}\,\mathrm{meV} < \Lambda < 10^{+2}\,\mathrm{meV}$ as our range of interesting values. Additional constraints on the parameter space from atom interferometry [83] are presented alongside our key results in Figures 4.2 and 4.3. This effective potential ties the chameleon to the following non-linear elliptic partial differential equation:

$$\nabla^2\phi = \frac{-\Lambda^5}{\phi^2} + \frac{\rho}{M}\,. \tag{4.2}$$

In addition, the minimum of the effective potential (Equation (4.1)) $\phi_{\mathrm{min}}(\rho)$, and the mass of fluctuations around this minimum, $m_\phi(\rho)$ are given by

$$\phi_{\mathrm{min}}(\rho) = \Big(\frac{\Lambda^5 M}{\rho}\Big)^{1/2}, \quad m_\phi^2(\rho) = 2\Big(\frac{\rho^3}{\Lambda^5 M^3}\Big)^{1/2}\,. \tag{4.3}$$

4.2 Parallel Plate Solutions

The launch point into the proposed experiment is to consider the chameleon field between two parallel plates, where the two plates are allowed to be of different densities. The configuration being imagined is depicted by Figure 4.1. As is usually the case for such problems, the approximation is made that the plates are infinite in extent reducing the above to a one-dimensional system. Although this idealised system does make the analysis approachable, a hidden assumption here is that edge effects due to the finite size of the plates will have a negligible impact on the calculated result. A brief discussion of the systematics involved here will be discussed in Section 4.3. If the widths of the two plates R_1 and R_2 are normalised such to maintain a constant mass per unit area, then with the help of Gauss' law of gravitation

$$\oiint \mathbf{g}\cdot\mathrm{d}\mathbf{A} = -4\pi G M_{\mathrm{obj}}\,, \tag{4.4}$$

where $\mathbf{g}$ is the gravitational acceleration and M_{obj} is the mass of the source object. It is clear that the superposition of the gravitational attraction of each plate will cause the gravitational force to vanish within the central region. In contrast, it transpires that the chameleon

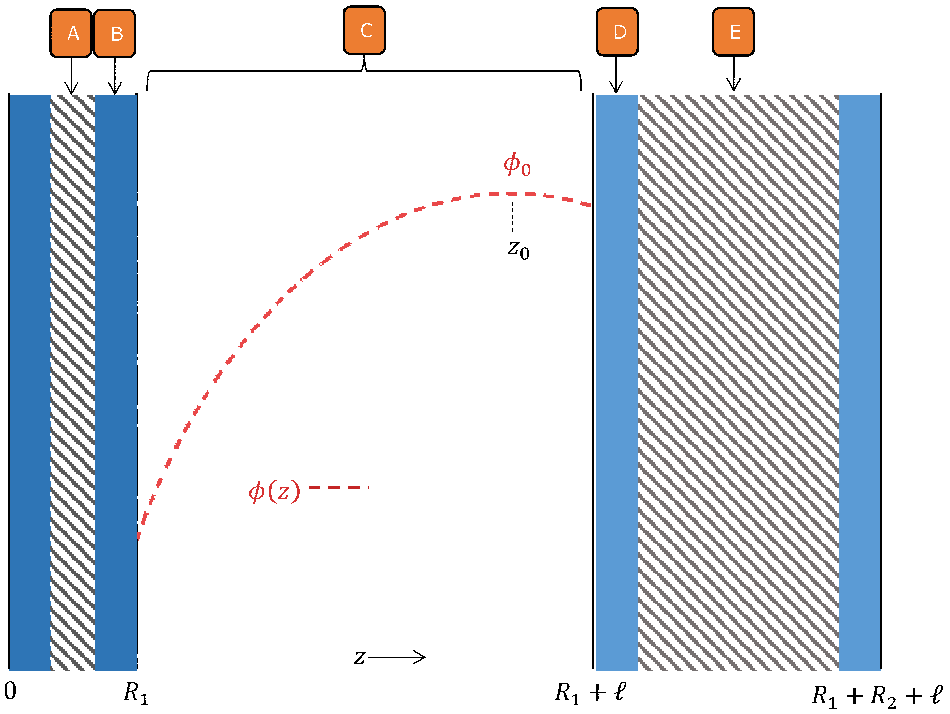

Figure 4.1: Parallel plate configuration with contrasting density values, keeping the density multiplied by the width of the plate the same for both plates. The plate separation is denoted ℓ with the left and right plate thicknesses as R_1 and R_2, with corresponding plate densities ρ_L and ρ_R respectively. The regions shaded with lines indicate where the field has reached the minimum of its effective potential inside the plate. The solid shaded regions are the shells in which the field rolls away from the minimum of the effective potential.

has a non-trivial field profile between the plates, as illustrated in Figure 4.1, and that this form is a function of the density of the two plates. Throughout this chapter, if the densities of the plates differ, without loss of generality it will be assumed that the left most plate has the higher density. Further, the width of the left-hand and right-hand plates will be denoted R_1 and R_2 respectively, with the plate separation given by ℓ.

The problem can be partitioned by making various approximations about the form of the effective potential in different regions, visualised in Figure 4.1. Analogous to the thin shell effect that occurs for the chameleon field profile around a sphere, if the plates are sufficiently wide they can be divided into core and shell regions. Represented by bands A and E in Figure 4.1, the core defines the space where the field lies near the potential minima $\phi \simeq \phi_{\rm min}(\rho)$, for which the field profile can be taken to remain constant. For the shell (bands B and D), the field is interpolating between the value that minimises the effective potential within the plate and some exterior value, bounded by the expectation value within the chamber. In doing so the field traverses the segment of the effective potential dominated by the density contribution. Furthermore, as long as the core region exists, the outer solutions completely decouple from the system. This means that the chameleon field profile between the plates becomes effectively independent of the behaviour of the chameleon outside the plates, and any chameleon perturbation attempting to propagate through the wall becomes exponentially suppressed if the Compton wavelength of the chameleon inside the plates is smaller than the plate thickness. Taking this as an assumption for now to then be verified at the end of the calculation, the problem reduces to a total of 4 interfaces across which to impose boundary conditions. Denoting the thickness of the shell adjacent to the boundary at R_1 to be δ_L and that adjacent to $R_1 + \ell$ to be δ_R, the problem reduces to solving the following set of equations:

$$\phi = \phi_L \ , \qquad z < R_1 - \delta_L \ , \tag{4.5a}$$

$$\nabla^2\phi = \frac{\rho_L}{M} \ , \qquad R_1 - \delta_L < z < R_1 \ , \tag{4.5b}$$

$$\nabla^2\phi = \frac{\rho_{bg}}{M} - \frac{\Lambda^5}{\phi^2} \ , \qquad R_1 < z < R_1 + \ell \ , \tag{4.5c}$$

$$\nabla^2\phi = \frac{\rho_L}{M} \ , \qquad R_1 + \ell < z < R_1 + \ell + \delta_R \ , \tag{4.5d}$$

$$\phi = \phi_R, \qquad z > R_1 + \ell + \delta_R, \tag{4.5e}$$

where δ_L and δ_R are unknowns to be determined through boundary conditions. The quantities ϕ_L and ϕ_R correspond to the evaluation of Equation (4.3) ($\phi = \phi_{\rm min}\left(\rho\right)$) for the left and right-hand plates respectively. The equations of Poisson form can be easily integrated out and matched at their respective core-shell interfaces. As usual, this involves enforcing the continuity of the field and its first derivative across the interface. Performing this calculation

finds that

$$\phi(z) = \frac{\rho_L}{2M}\left(x - (R_1 - \delta_L^{(2)})\right)^2 + \phi_L \ , \qquad R_1 - \delta_L < z < R_1 \ ,$$

$$\nabla^2\phi = \frac{\rho_{bg}}{M} - \frac{\Lambda^5}{\phi^2} \ , \qquad R_1 < z < R_1 + \ell \ , \tag{4.6}$$

$$\phi(z) = \frac{\rho_R}{2M}\left(x - \left(R_1 + l + \delta_R^{(1)}\right)\right)^2 + \phi_R \ , \qquad R_1 + \ell < z < R_1 + \ell + \delta_R \ .$$

Arriving at a solution describing the region between the two plates (band C) is a little more tricky. Initially the hope was to be able to utilise the same parabolic approximation invoked for the spherical and ellipsoidal analysis. However, with the benefit of hindsight, the validity of this approach would require significant plate separations to hold true, due to the large field decay length in the lab vacuum, so had no real practical application. This calculation has been included in the appendix as the results are still generally useful in building an intuition for how the density asymmetry influenced the field profile. The remaining option was to attempt to deal with the non-linear equation directly. At the time this research was performed, this calculation had been performed for the case of the chameleon field within a vacuum [85, 116, 117] although without allowing the densities of the plates to vary. Considering the low density (lab vacuum) region nested between the two parallel plates, it can be assumed that the behaviour of the chameleon field will primarily be driven by the its self-interaction term in Equation (4.1). This is because in moving from a high density to a low density region, the field traverses the segment of the effective potential dominated by the bare potential. This assumption can be imposed a priori on the system by artificially setting the density term to be zero within the field equation, leading to a solvable integral. In one dimension, the problem to be solved is now

$$\frac{\partial^2\phi}{\partial z^2} = -\frac{\Lambda^5}{\phi^2} \ . \tag{4.7}$$

The above can be multiplied by $\partial\phi/\partial z$ and integrated with respect to z to give the result

$$\frac{1}{2}\left(\frac{\partial\phi}{\partial z}\right)^2 = \frac{\Lambda^5}{\phi} + \alpha \ , \tag{4.8}$$

where α is a constant of integration. Introducing ϕ_0 as the value of ϕ at which the field reaches its maximum value between the two plates, that is $\partial\phi/\partial z = 0$, the above can be written as

$$\frac{1}{2}\left(\frac{\partial\phi}{\partial z}\right)^2 = \frac{\Lambda^5}{\phi\,(z)}\left(1 - \frac{\phi\,(z)}{\phi_0}\right) \ . \tag{4.9}$$

Taking the square root, this can be reformulated as the integral

$$\int_{\phi_0}^{\phi(z)} \frac{\varphi^{1/2}(z)}{\sqrt{1 - \frac{\varphi(z)}{\phi_0}}}\,\mathrm{d}\varphi = \pm\sqrt{2\Lambda^5}\,(z - z_0) \ , \tag{4.10}$$

where the second unknown constant of integration z_0 corresponds to the position between the plates at which the value of the field hits ϕ_0. After a sequence of relatively straightforward variable substitutions, this integral can be solved to recover an implicit equation of the form

$$\phi_0^{3/2}\left\{\arccos\sqrt{\frac{\phi(\mathrm{z})}{\phi_0}}+\sqrt{\frac{\phi(\mathrm{z})}{\phi_0}}\left(1-\frac{\phi(\mathrm{z})}{\phi_0}\right)^{1/2}\right\}=\mp\sqrt{2\Lambda^5}\,(z-z_0)\ . \tag{4.11}$$

Collecting everything together, the problem therefore reduces to the following set of equations:

$\underline{R_1-\delta_L<z<R_1:}$

$$\phi(z)=\frac{\rho_L}{2M}\left(z-(R_1-\delta_L)\right)^2+\phi_L\ . \tag{4.12}$$

$\underline{R_1<z<R_1+\ell:}$

$$\arccos\sqrt{\frac{\phi(\mathrm{z})}{\phi_0}}+\sqrt{\frac{\phi(\mathrm{z})}{\phi_0}}\left(1-\frac{\phi(\mathrm{z})}{\phi_0}\right)^{1/2}=\mp\sqrt{\frac{2\Lambda^5}{\phi_0^3}}\,(\mathrm{z}-\mathrm{z}_0)\ . \tag{4.13}$$

$\underline{R_1+\ell<z<R_1+\ell+\delta_R:}$

$$\phi(z)=\frac{\rho_R}{2M}\left(z-(R_1+l+\delta_R)\right)^2+\phi_R\ . \tag{4.14}$$

Proceeding from this point can be done one of two ways. The first path followed was to consider the limiting forms of Equation (4.13) at each boundary. This had the benefit of returning closed form expressions for the four unknowns of integration ϕ_0, z_0, δ_L and δ_R but at the expense of not being applicable across the entire chameleon parameter space. The second route is to impose the boundary conditions across the two interfaces directly onto the implicit equation for ϕ. In contrast to the first method, the resulting equations apply across the full parameter space at the expense of having to be handled numerically. Ultimately these two approaches are complementary as the full analytic results of the first method can be used to verify the numerical outcomes of the second. As they both have their merits, both of these approaches will be discussed in more detail within the sections to follow.

4.2.1 The Limiting Forms of the Central Solution

The goal in this case is to demonstrate the limiting forms of Equation (4.13) that lead to explicit expressions for the chameleon field $\phi\,(z)$. The natural variable appearing in Equation (4.13) is the ratio $\phi(z)/\phi_0$ which varies between 0 and 1. The important thing is to consider that any limiting cases only need to replicate the behaviour of this quantity approaching the surfaces of each plate, where the explicit form for ϕ becomes necessary. The simplest possibility is where the field maxima is significantly higher than the value at the vacuum-plate interface. In this case, the approximation $\phi(z)\ll\phi_0$ becomes relevant within the proximity of the boundary. Under this assumption, the field profile becomes

$$\phi(z)=\phi_0\left\{\frac{3}{2}\left(\frac{\pi}{2}\pm\sqrt{\frac{2\Lambda^5}{\phi_0^3}}\,(z-z_0)\right)\right\}^{2/3}\ . \tag{4.15}$$

As will be made clear shortly, the ambiguity involved due to the ± sign appearing in Equation (4.15) gets resolved upon imposing boundary conditions.

The other possibility is when the field value across the interface lies close to the vacuum maxima, which translates to the statement that $\phi(z)/\phi_0 \approx 1$. Neglecting sub-leading order corrections when perturbing $\phi(z)/\phi_0$ around 1 generates the profile

$$\phi(z) = \phi_0 \left(1 - \frac{\Lambda^5}{2\phi_0^3}\left(z - z_0\right)^2\right) \ . \tag{4.16}$$

These two forms (Equations (4.15) and (4.16)) can be paired in numerous ways to fully specify the chameleon for a large portion of the parameter space. Hereinafter, the results of Equations (4.15) and (4.16) will be described as the far and near-maxima solutions respectively.

Turning attention first to the boundary between the higher density left-hand plate, and the intermediate vacuum region, it is sensible to begin by considering the far-maxima solution. A simple argument can be made for this: at a higher density, the expectation value within the left-hand plate will be lower relative to that of the right-hand plate. This will have the effect of pulling the corresponding surface field value away from ϕ_0, making the far-maxima approximation the more natural first choice. Beginning with Equation (4.15), increasing the value of z should push the solution closer towards ϕ_0. In this case, the positive option from Equation (4.15) is selected to give

$$\phi(z) = \phi_0 \left\{\frac{3}{2}\left(\frac{\pi}{2} + \sqrt{\frac{2\Lambda^5}{\phi_0^3}}\left(z - z_0\right)\right)\right\}^{2/3} \ , \tag{4.17}$$

with the field gradient given by

$$\phi'(z) = \sqrt{\frac{2\Lambda^5}{\phi_0}}\left(\frac{2}{3}\right)^{1/3}\left\{\frac{\pi}{2} + \sqrt{\frac{2\Lambda^5}{\phi_0^3}}\left(z - z_0\right)\right\}^{-1/3} \ . \tag{4.18}$$

Interestingly, for an error threshold of 1 percent, this approximate form remains valid up to $\phi(z)/\phi_0 \leq 0.35$, as seen in Figure 4.2. This follows from the ability to perform the above expansion to second order, due to the first order terms cancelling when expanding the implicit equation. Equating the fields and their derivatives across the boundary at $z = R_1$ leads to the equations

$$\phi_0 \left\{\frac{3}{2}\left(\frac{\pi}{2} + \sqrt{\frac{2\Lambda^5}{\phi_0^3}}\left(R_1 - z_0\right)\right)\right\}^{2/3} = \frac{\rho_L}{2M}\left(\delta_L^{(2)}\right)^2 + \phi_L \ , \tag{4.19a}$$

$$\sqrt{\frac{2\Lambda^5}{\phi_0}}\left\{\frac{3}{2}\left(\frac{\pi}{2} + \sqrt{\frac{2\Lambda^5}{\phi_0^3}}\left(R_1 - z_0\right)\right)\right\}^{-1/3} = \frac{\rho_L \delta_L^{(2)}}{M} \ . \tag{4.19b}$$

By utilising the gradient equation, the fractional power term in the coordinates can be written as

$$\phi_0 \left\{ \frac{3}{2} \left(\frac{\pi}{2} + \sqrt{\frac{2\Lambda^5}{\phi_0^3}} \left(R_1 - z_0 \right) \right) \right\}^{2/3} = \frac{2M^2\Lambda^5}{\rho_L^2 \delta_L^2 \phi_0} \, . \tag{4.20}$$

Incorporating this result into the field equation leads to a polynomial equation for δ_L of the form

$$\frac{\rho_L \delta_L^4}{2M} + \phi_L \delta_L^2 - \frac{2M^2\Lambda^5}{\rho_L^2} = 0 \, , \tag{4.21}$$

which can be realised as a quadratic in δ_L^2. The exact solution is quoted below in Equation (4.23) where the positive sign was taken to allow it to be consistent with Δ's definition as a squared real quantity:

$$\Delta = \left(\sqrt{5} - 1 \right) \frac{\phi_L M}{\rho_L} \, , \tag{4.22}$$

from which it follows that

$$\delta_L = \left\{ \frac{M\phi_L}{\rho_L} \left(\sqrt{5} - 1 \right) \right\}^{1/2} = \left\{ \frac{2}{m_L^2} \left(\sqrt{5} - 1 \right) \right\}^{1/2} = \lambda_L \left(2\sqrt{5} - 2 \right)^{1/2} \, , \tag{4.23}$$

having made use of the identities $\phi_{\min}^{(L)} = \left(M\Lambda^5/\rho_L \right)^{1/2}$ and $m_L = \sqrt{2} \left(\rho_L^3/\Lambda^5 M^3 \right)^{1/4}$. The inverse field mass has also been introduced as $\lambda_L = m_L^{-1}$. Equation (4.23) seems to suggest that the internal field structure of this plate is independent of the other. Returning to gradient Equation (4.19b), switching in the above relation to eliminate δ_L gives

$$\sqrt{\frac{2\Lambda^5}{\phi_0}} \left\{ \frac{3}{2} \left(\frac{\pi}{2} + \sqrt{\frac{2\Lambda^5}{\phi_0^3}} \left(R_1 - z_0 \right) \right) \right\}^{-1/3} = \left(2\sqrt{5} - 2 \right)^{1/2} \frac{\rho_L \lambda_L}{M} \, . \tag{4.24}$$

Upon cubing and inverting the above expression, one obtains

$$\sqrt{\frac{\phi_0^3}{\left(2\Lambda^5 \right)^3}} \left\{ \frac{3}{2} \left(\frac{\pi}{2} + \sqrt{\frac{2\Lambda^5}{\phi_0^3}} \left(R_1 - z_0 \right) \right) \right\} = \left(2\sqrt{5} - 2 \right)^{-3/2} \left(\frac{M}{\lambda_L \rho_L} \right)^3 \, , \tag{4.25}$$

then rearranging to make z_0 the subject gives

$$z_0 = R_1 + \frac{2}{3} \lambda_\phi^{(L)} \left\{ \frac{3\pi}{4} \left(\frac{\phi_0}{\phi_L} \right)^{3/2} - \left(\frac{2}{\sqrt{5} - 1} \right)^{3/2} \right\} \, . \tag{4.26}$$

The above has been written in a more convenient form by making use of the relation $m_L = \sqrt{2\Lambda^5/\phi_{\min}^{(L)3}}$.

After a little thought, it can be seen from Equation (2.18a) that the lower bound of ϕ_0 is given by ϕ_R. This stems from the fact that this analysis relies on the existence on a core region which allowed for the decoupling of the system. By utilising this in conjunction with the result that $\delta_L = \lambda_L \left(2\sqrt{5} - 1 \right)^{1/2}$, the error constraint $\phi(z)/\phi_0 \leq 0.35$ can be translated into a condition on the density ratio between the two plates. In particular, it can be

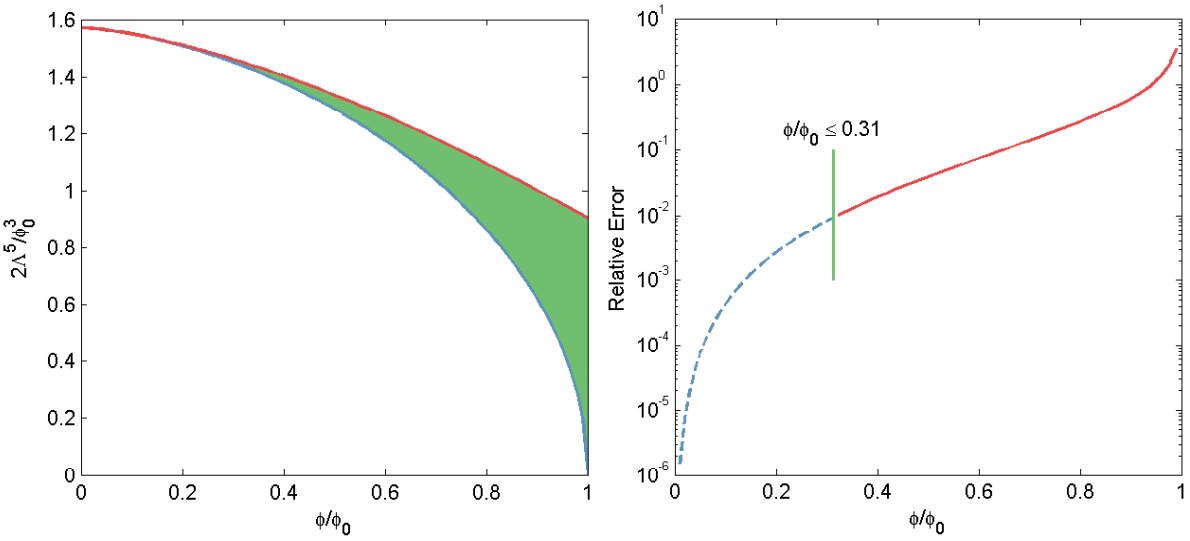

Figure 4.2: A figure comparing exact and approximate forms for the left-hand side of equation (4.11). Left: Variation of the quantity ϕ/ϕ_0 for the exact result (blue) and approximate result (red). Right: Relative error as a function of ϕ/ϕ_0, showing that limiting the error to be below 0.01 corresponds to an upper bound of $\phi/\phi_0 \sim 0.31$ for the approximation to remain valid. The shaded green region is to illustrate the difference between the approximate and exact solutions.

found that the far-maxima approximation accurately describes the chameleon field profile approaching the left-hand plate provided that the following density inequality is satisfied:

$$\sqrt{\frac{\rho_L}{\rho_R}} \gtrsim \frac{\sqrt{5}+1}{2} \,. \tag{4.27}$$

Importantly, as this statement follows from considering the limiting case when $\phi_0 = \phi_R$, satisfying the above guarantees validity across the entire chameleon parameter space. It turns out that the above translates to a minimum density ratio of $\rho_L/\rho_R \approx 2$ which falls well within a sensible range. Therefore, the description of the chameleon field across the left-hand plate-vacuum interface can be fully contained by the results derived under the far-maxima approximation.

In turning attention to the planar-surface between the vacuum region and the right-hand plate, there are a number of options. The simplest of these corresponds to a case of mild asymmetry in the chameleon field, where the surface value is sufficiently lower than the field maxima ϕ_0 such that the far-maxima approximation can again be called. The remaining two options demonstrate more severe asymmetry in the field profile. In the limiting case that the position of the central maxima falls exactly at the surface of the plate, from previous arguments the value of ϕ_0 is set at ϕ_R. Therefore, as the first option, consider as the position of the central maxima z_0 approaches the planar-surface from the left. The behaviour of the chameleon field nearing this point should be described by perturbing ϕ_0 around its lower bound, for which the near maxima solution of Equation (4.16) is the perfect candidate. The

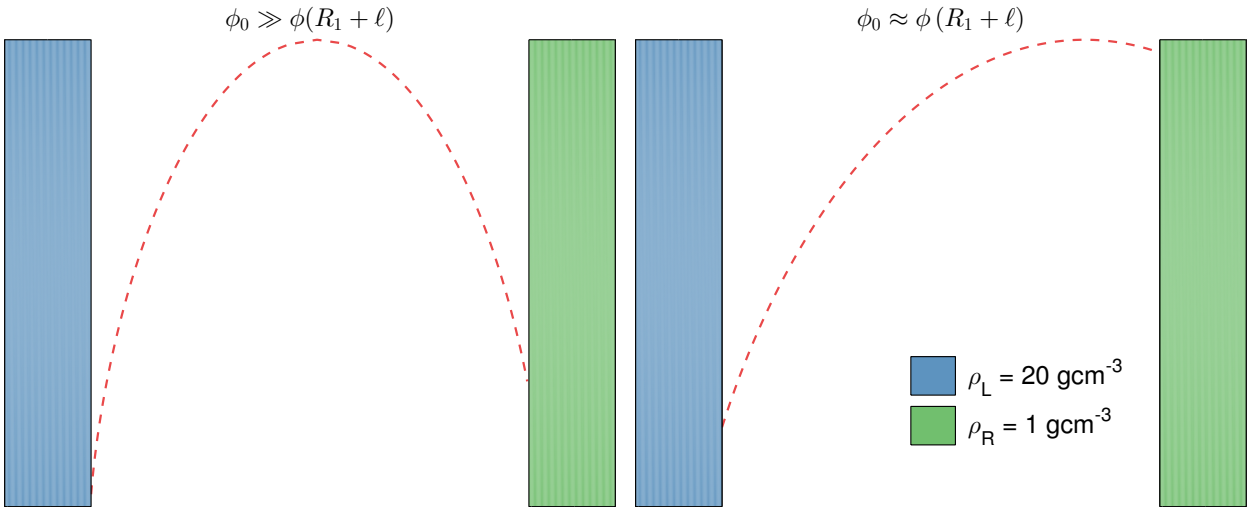

Figure 4.3: Illustration of the chameleon field profile for two limiting examples of asymmetry. To the left corresponds to a small degree of asymmetry in the chameleon field, whereas that to the right displays a strong degree of asymmetry.

remaining possibility is that the field maxima falls within the right-hand plate. This is the case when the field lacks adequate space to rise to the bounding value of ϕ_0 within the vacuum region. As a result, the field continues to slide down the self-interaction dominated term within the effective potential. Under these circumstances, the chameleon field is insensitive to the boundary approaching the lower-density plate, and as a result the boundary-value problem greatly simplifies. In this sections to follow, each of these cases will be considered in turn.

Mild Asymmetry of the Chameleon Field

Considering the presence of a mild asymmetry in the chameleon field profile, the assumption can be made that the field value across the right-hand boundary falls sufficiently below the central maxima, such that the far-field approximation of Equation (4.15) can be applied. In this case, it follows that now the negative sign in Equation (4.15) must be chosen to ensure the consistency of the associated gradient continuity equation. As a result, the boundary equations become

$$\begin{aligned} \phi_0 \left\{ \frac{3}{2} \left(\frac{\pi}{2} - \sqrt{\frac{2\Lambda^5}{\phi_0^3}} \left(R_1 + \ell - z_0 \right) \right) \right\}^{2/3} &= \frac{\rho_L}{2M} \left(\delta_L^{(2)} \right)^2 + \phi_L \,, \\ \sqrt{\frac{2\Lambda^5}{\phi_0}} \left\{ \frac{3}{2} \left(\frac{\pi}{2} - \sqrt{\frac{2\Lambda^5}{\phi_0^3}} \left(R_1 + \ell - z_0 \right) \right) \right\}^{-1/3} &= \frac{\rho_L \delta_L^{(2)}}{M} \,. \end{aligned} \tag{4.28}$$

The error scaling for the negative solution is slightly more restrictive, where now limiting the error at the 1 percent level translates to satisfying the condition $\phi(z)/\phi_0 \leq 0.1$ at the boundary. Following the calculation through in the same way as before unsurprisingly finds

δ_R to be

$$\delta_R = \lambda_R \left(2\sqrt{5} - 2\right)^{1/2} , \tag{4.29}$$

leading to an additional expression for z_0:

$$z_0 = R_1 + \ell - \frac{2}{3}\lambda_R \left\{ \frac{3\pi}{4} \left(\frac{\phi_0}{\phi_R}\right)^{3/2} - \left(\frac{2}{\sqrt{5}-1}\right)^{3/2} \right\} . \tag{4.30}$$

This, in conjuction with the former expression for z_0 can be combined to solve completely for the remaining unknowns ϕ_0 and z_0 which leads to

$$\phi_0 = \left(\frac{\Lambda^5}{2}\right)^{1/3} \left\{ \frac{2\ell}{\pi} + \frac{4}{3\pi} \left(\frac{2}{\sqrt{5}-1}\right)^{3/2} (\lambda_R + \lambda_L) \right\}^{2/3} , \tag{4.31a}$$

$$z_0 = R_1 + \frac{\ell}{2} + \left\{ \frac{\lambda_R - \lambda_L}{2} \left(\frac{2}{\sqrt{5}-1}\right)^{3/2} \right\} . \tag{4.31b}$$

The above form for z_0 makes it clear how the field asymmetry is sourced by a density contrast, as this results in different values for the Compton wavelengths pertaining to each plate. The primary consistency check for this result is to verify that the conditions $\phi(z)/\phi_0 \leq 0.35$ and $\phi(z)/\phi_0 \leq 0.1$ are met across the left and right hand boundaries respectively. Incorporating both of these restrictions for a given set of experimental parameters, is it possible to study the region of parameter space where this calculation holds.

Strong Asymmetry of the Chameleon Field

Moving on to consider examples of strong asymmetry in the chameleon field profile, it can be taken that the field value across the right-hand vacuum-plate interface lies within the proximity of the maxima, which translates to the statement that $\phi(z)/\phi_0 \sim 1$. The explicit field profile in this case is given by the result already presented in Equation (4.16), restated here for convenience:

$$\phi(z) = \phi_0 \left(1 - \frac{\Lambda^5}{2\phi_0^3} (z - z_0)^2\right) . \tag{4.32}$$

As for the previous example, the consistency of the above should be verified at the end of the calculation. Equating the field at its derivatives across the boundary at $z = R_1 + \ell$ gives

$$\begin{aligned} \phi_0 \left(1 - \frac{\Lambda^5}{2\phi_0^3} (R_1 + \ell - z_0)^2\right) &= \frac{\rho_R}{2M}\delta_R^2 + \phi_R , \\ \frac{\Lambda^5}{\phi_0^2} (R_1 + \ell - z_0) &= \frac{\rho_R}{M}\delta_R . \end{aligned} \tag{4.33}$$

The gradient equation can be used to eliminate δ_R from the field continuity equation:

$$\phi_0 = (R_1 + \ell - z_0)^2 \frac{\Lambda^5}{2\phi_0^2} \left\{ 1 + \left(\frac{\phi_R}{\phi_0}\right)^2 \right\} + \phi_R , \tag{4.34}$$

at which point the previous expression obtained for z_0 in Equation (4.26) can be called upon which leads to the relation

$$\phi_0 = \left[\left(\ell - \lambda_L \left\{ \frac{\pi}{2} \left(\frac{\phi_0}{\phi_L} \right)^{3/2} - \frac{2}{3} \left(\frac{2}{\sqrt{5}-1} \right)^{3/2} \right\} \right)^2 \left\{ 1 + \left(\frac{\phi_R}{\phi_0} \right)^2 \right\} \right] + \phi_R \, . \tag{4.35}$$

In choosing to proceed under the assumption that ϕ_0 lies close ϕ_R, a small parameter γ can be introduced such that $\phi_0 = (1+\gamma)\,\phi_R$. Accordingly, the above can be expanded to leading order corrections in γ:

$$\sqrt{2}\lambda_R \gamma^{1/2} \left(1 + \frac{3\gamma}{2} \right) = \left(\ell - \lambda_L \left\{ \frac{\pi}{2} \left(1 + \frac{3\gamma}{2} \right) \left(\frac{\phi_R}{\phi_L} \right)^{3/2} - \frac{2}{3} \left(\frac{2}{\sqrt{5}-1} \right)^{3/2} \right\} \right) \, , \tag{4.36}$$

which should be solvable for γ thus leading to a value for ϕ_0. Although reaching the above relies on taking a square root which would generally lead to the inclusion of a $\pm$ in the above expression, only the positive root is relevant to this problem. In fact, the negative root would require $\gamma < 0$ (making the above equation imaginary) unless the corresponding field maxima ϕ_0 were to form within the right hand plate, which is outside the validity of this solution. After some manipulation, the above can be written in a more tangible form:

$$\frac{3}{2} \left(\Delta + \frac{\pi}{2} \right) \gamma + \sqrt{2}\, \gamma^{1/2} - \Delta = 0 \, , \tag{4.37}$$

where the constant piece Δ is identified to be

$$\Delta = \left\{ \frac{\ell}{\lambda_R} + \frac{2\lambda_L}{3\lambda_R} \left(\frac{2}{\sqrt{5}-1} \right)^{3/2} - \frac{\pi}{2} \right\} \, . \tag{4.38}$$

Requiring $\gamma > 0$ the positive root to the quadratic is taken to give

$$\gamma^{1/2} = \frac{\sqrt{2}}{3\left(\Delta + \frac{\pi}{2}\right)} \left\{ \left(1 + 3 \left(\Delta + \frac{\pi}{2} \right) \Delta \right)^{1/2} - 1 \right\} \, . \tag{4.39}$$

In order for Equation (4.39) above to yield a consistent solution for γ and by extension the linked unknowns ϕ_0, z_0 and δ_R, it is required that $\gamma \ll 1$ and that it is real. The latter of these conditions may be imposed by examining the discriminant of the above form.[1] The verification of these above requirements is most easily performed numerically.

As previously mentioned, in the more severe examples of asymmetry, it is possible for the position of the field maxima to penetrate into the lower density (right-hand) plate. As this essentially removes the remaining boundary from the problem, this regime can be easily be solved by substituting the expressions obtained across the left-hand boundary (Equation (4.26)) and setting $\phi_0 = \phi_R$ to give

$$z_0 = R_1 + \frac{2}{3}\lambda_L \left\{ \frac{3\pi}{4} \left(\frac{\phi_R}{\phi_L} \right)^{3/2} - \left(\frac{2}{\sqrt{5}-1} \right)^{3/2} \right\} \, . \tag{4.40}$$

[1] The value γ becoming imaginary indicates the point at which the position of the field maxima crosses into the (right-hand) plate.

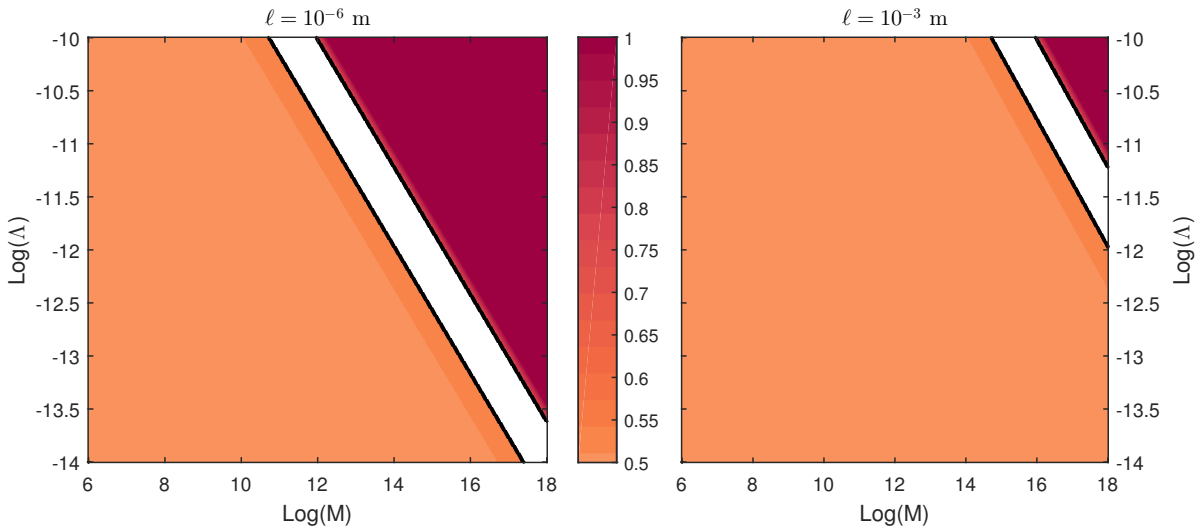

Figure 4.4: This figure shows the combined regimes of validity of the three limiting solutions for plate separations of $\ell = 10^{-6}$m and 10^{-3}m (from left to right). The relative position of the field maxima, spanning from 0.5 (on centre) to 1 (far right) of the intermediate region is indicated by the shading. The region of the parameter space that remains unmapped is represented by the white bands appearing in each plot.

For each parameter value, the approach followed was to numerically cycle through the various scenarios presented in this section until a consistent solution is found. Upon consolidating the results obtained for each possibility, a picture of the chameleon parameter space can be built up in a piecewise manner. The results obtained by considering the limiting forms of the central solution are presented in Figure 4.4 which displays the response of the field asymmetry to model parameters M and Λ. In moving diagonally upwards from the bottom-right region of the parameter, the field traverses states of mild asymmetry before the underlying approximations begin to break down. At this point, signified by the lower black contour, examples of intermediate asymmetry are realized which remain untouched by this analysis. Continuing upwards moves the field into a regime of strong asymmetry where the analytic results once again become applicable for the remainder of the parameter space. It is also made clear that smaller plate separations would generally be favourable in an experiment aiming to harness the effects of an asymmetric field profile. The key observation here, is that for any given value of the chameleon self interaction scale Λ the degree of asymmetry in the chameleon field profile (following from the value of z_0 being offset from the central position of $R_1 + \ell/2$ between the plates increases as the value of the chameleon energy scale M is increased. This indicates that asymmetry effects may allow us to probe the weak coupling regime, where the associated fifth force will be more difficult to detect.

4.2.2 A Semi-Analytic Approach

In considering the limiting forms of the central solution it became possible to systematically map out a large portion of the chameleon parameter space by stitching together the outcomes of making various assumptions about the field structure approaching each boundary. Unfortunately, the band of model parameters untouched by this approach was too substantial to comfortably rely on any form of interpolation between the mapped regions in any attempts to constrain the theory. This lead to the consideration of an alternative route which was to deal with the implicit equation of Equation (4.13) directly when imposing boundary conditions. The launch point into this calculation is the gradient equation (Equation (4.8)) which appeared as part of the derivation of the implicit solution. This specifies that the derivative of the field within the central region satisfies the relation

$$\left(\frac{\partial\phi}{\partial z}\right)^2 = \frac{2\Lambda^5}{\phi}\left(1-\frac{\phi(z)}{\phi_0}\right) \ . \tag{4.41}$$

As seen previously, expressions for the unknowns of integration ϕ_0, z_0, δ_L and δ_R follow from imposing continuity of the field and its first derivative at the surface of each plate. Beginning with the matching at $z = R$, the gradient equation leads to the formula

$$\frac{\phi(R)}{\phi_0} = \left\{1+\frac{\phi_0}{\phi_L}\left(\frac{m_L\delta_L}{2}\right)^2\right\}^{-1} \ , \tag{4.42}$$

where m_L corresponds to the mass of the chameleon field within the left-hand plate. The currently undetermined quantity $\phi(R)$ can be eliminated by calling the shell solution of Equation (4.12). In particular, the value of the field at the boundary is given by

$$\phi(R) = \phi_L\left(1+\left(\frac{m_L\delta_L}{2}\right)^2\right) \ . \tag{4.43}$$

After a little bit of algebra, it follows that consolidating these two results leads to the polynomial equation

$$\frac{\phi_L}{\phi_0} = \frac{1-\left(\frac{m_L\delta_L}{2}\right)^2-\left(\frac{m_L\delta_L}{2}\right)^4}{1+\left(\frac{m_L\delta_L}{2}\right)^2}. \tag{4.44}$$

As mentioned as part of the discussion on the limiting forms of the chameleon field, dealing with the right-hand boundary is an ambiguous problem. Ultimately, the two possible scenarios divide according to whether or not the field forms a central maximum in the region between the two plates. Essentially, this boils down to having to, or not having to account for the existence of the right-hand boundary when solving for the unknowns of the system. These two options will be tackled in turn in the sections to follow.

The Chameleon Reaches a Maximum Value in between the Plates

The first possibility is that the chameleon rises to a maximum value within the intermediate vacuum region. If so, performing the same analysis across the right-hand boundary amounts

to switching the variables in the above to their right-hand counterparts. That is $\phi_L \rightarrow \phi_R, m_L \rightarrow m_R$ and $\delta_L \rightarrow \delta_R$. Accordingly the two equations can be condensed into a single representation:

$$\frac{\phi_i}{\phi_0} = \frac{1 - \left(\frac{m_i\delta_i}{2}\right)^2 - \left(\frac{m_i\delta_i}{2}\right)^4}{1 + \left(\frac{m_i\delta_i}{2}\right)^2}. \tag{4.45}$$

Having dealt with the continuity of the gradient across each boundary, what is left is to impose the continuity of the field itself. This can be achieved by calling the implicit solution of Equation (4.46) in conjunction with the shell solutions at their respective boundaries. In this case, the shell solutions can be used to eliminate $\phi(z)$ from the implicit formula, granting two additional equations:

$$\arccos\sqrt{\frac{1}{1 + \frac{\phi_0}{\phi_i}\left(\frac{m_i\delta_i}{2}\right)^2}} + \frac{\sqrt{\frac{\phi_0}{\phi_i}}\frac{m_i\delta_i}{2}}{1 + \frac{\phi_0}{\phi_i}\left(\frac{m_i\delta_i}{2}\right)^2} = \left(\frac{\phi_i}{\phi_0}\right)^{3/2}\begin{cases} m_L(z_0 - R) & \text{if } i = L \\ m_R(R + l - z_0) & \text{if } i = R \end{cases}. \tag{4.46}$$

Thus Equations (4.45) and (4.46) present four equations for the four unknowns of the problem ϕ_0, z_0, δ_L and δ_R. As a consistency check of the method presented in Section 4.2.1, the system above can be solved by considering the series expansion for small ϕ_L/ϕ_0. Specifically, Equation (4.45) evaluated at surface of the left-hand plate leads to

$$\left(\frac{m_L\delta_L}{2}\right)^4 + \left(\frac{m_L\delta_L}{2}\right)^2\left(1 + \frac{\phi_L}{\phi_0}\right) - 1 + \frac{\phi_L}{\phi_0} = 0, \tag{4.47}$$

the above can be identified as quadratic in the quantity $(m_L\delta_L/2)^2$ which is readily solved to give

$$\left(\frac{m_L\delta_L}{2}\right)^2 = -\frac{1}{2}\left\{1 + \frac{\phi_L}{\phi_0} \mp \sqrt{5 - \frac{2\phi_L}{\phi_0} + \frac{\phi_L^2}{\phi_0^2}}\right\}, \tag{4.48}$$

from which it is straightforward to see that taking the limit $\phi_L/\phi_0 \ll 1$ gives a closed form solution for the shell thickness δ_L:

$$\left(\frac{m_L\delta_L}{2}\right)^2 = \frac{1}{2}(\sqrt{5} - 1), \tag{4.49}$$

which is in agreement with the result of Equation (4.23). Furthermore, in combining this with the expansion of Equation (4.46) for small arguments, an explicit expression for z_0 can be obtained:

$$z_0 = R_1 + \frac{2}{3m_L}\left\{\frac{3\pi}{4}\left(\frac{\phi_0}{\phi_L}\right)^{3/2} - \left(\frac{2}{\sqrt{5} - 1}\right)^{3/2}\right\}, \tag{4.50}$$

which matches that found following the previous method. In the the more general case, Equations (4.45) and (4.46) must be solved numerically. As the expressions contained within Equations (4.45) and (4.46) specify a completely deterministic system, this can be achieved

through the implementation of an interval bisection scheme. Broadly speaking, the idea here is to iteratively scan across a range for some input parameter and identify that which maximises the consistency between the underlying equations. To present this more formally, it is beneficial to work with the set of dimensionless variables defined by

$$x_i = \frac{m_i \delta_i}{2}, \qquad y_i = \frac{\phi_i}{\phi_0} \qquad i \in (L, R) \; , \tag{4.51}$$

where Equation (4.45) specifies these quantities to follow the relation

$$y_i = \frac{1 - x_i^2 - x_i^4}{1 + x_i^2}, \qquad i \in (L, R) \; . \tag{4.52}$$

It can be inferred from Equation (4.45) that the parameters y_L and y_R are confined to the range $[0, 1]$. This in turn places the following bound on the values of x_L and x_R:

$$0 \leq x_i \leq \frac{1}{2}\left(\sqrt{5} - 1\right) \qquad i \in (L, R) \; . \tag{4.53}$$

Furthermore, notice that the form of Equation (4.52) directly connects the values of x_L and x_R. That is, selecting a value for one of these terms uniquely determines the other. Suppose now that some trial value for x_L is specified within the allowed range, the implicit formulas of Equation (4.46) evaluated at each surface can be used to return two distinct values of z_0, which can be denoted $z_0^{(L)}$ and $z_0^{(R)}$ (pertaining to the left and right-hand boundaries respectively). In particular

$$\begin{aligned} z_0^{(L)} &= R_1 + \frac{\lambda_L}{y_L^{3/2}} \left\{ \arccos \sqrt{\frac{y_L}{y_L + x_L^2}} + \frac{y_L^{1/2} x_L}{y_L + x_L^2} \right\} \; , \\ z_0^{(R)} &= R_1 + l - \frac{\lambda_R}{y_R^{3/2}} \left\{ \arccos \sqrt{\frac{y_R}{y_R + x_R^2}} + \frac{y_R^{1/2} x_R}{y_R + x_R^2} \right\} \; , \end{aligned} \tag{4.54}$$

when these two outcomes identically match, a consistent solution to the problem has been found. Therefore, a numerical solution can be obtained by finding a value for some input parameter x_L, x_R, y_L or y_R such as to minimise the discrepancy between the returned values of z_0. The interval bisection method used to solve this system involved introducing a relative error term ϵ such that

$$\epsilon = \frac{z_0^{(L)} - z_0^{(R)}}{z_0^{(L)} + z_0^{(R)}} \; , \tag{4.55}$$

which is found to be a monotonically decreasing function of x_L. A test value of x_L can then be input at the half way point of the interval specified by Equation (4.53). If the associated value of ϵ is less than zero, this input defines a new upper bound for the range. Conversely, if the relative error is greater than zero, a new lower bound is introduced. Subsequent iterations would then continue to sample the input value as the halfway point of the updated interval until the error parameter ϵ fell below the 10^{-7} level. The outcome of this process is displayed in Figure 4.5 which demonstrates the scaling of the error parameter ϵ with input value x_L. Furthermore, the example taken fell into the mild asymmetry range which allowed for the numerical result to be verified against the analytic approximations presented earlier.

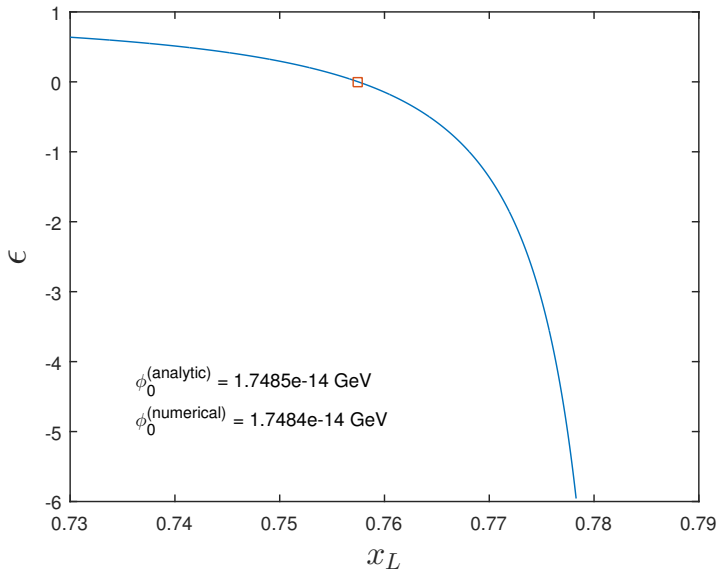

Figure 4.5: The response of the error parameter ϵ with input parameter x_L. The figure was generated for model parameter values $M = 10^{10}$ GeV and $\Lambda = 10^{-10}$ GeV and a plate separation of $\ell = 1\mu m$. The point for which the error passes through zero is identified with the square red marker. For reference, the associated value of ϕ_0 has been compared to the analytic result found via considering the limiting forms of the chameleon field.

There is No Central Maximum

If no central maximum exists, the field has insufficient space to reach a maxima within the vacuum region. In that case the field value continues to rise within the right hand plate, and its evolution is further described by Equation (4.46). This results in Equation (4.14) being omitted from the calculation (with the unknown δ_R being no longer relevant to the problem) and the upper bound of Equation (4.46) can be set to z_0, which now lies inside the plate. As the existence of a core region is assumed, this dictates the value of the field maxima is given by $\phi_0 = \phi_R$. The system then reduces to solving Equations (4.45) and (4.46) across the single boundary corresponding to the surface of the left-hand plate. In this case, an exact solution for z_0 exists and no numerical calculation is necessary. To see this, recall the dimensionless quantities x_L and y_L introduced in the preceding discussion. In fixing $\phi_0 = \phi_R$, these two now become known quantities following the relations

$$\begin{aligned} y_L &= \left(\frac{\rho_R}{\rho_L}\right)^{1/2}, \\ x_L &= \frac{1}{\sqrt{2}}\left\{\sqrt{\left(\frac{\rho_R^{1/2}}{\rho_L^{1/2}} - 1\right)^2 + 4} + \frac{\rho_R^{1/2}}{\rho_L^{1/2}}\right\}^{1/2}, \end{aligned} \tag{4.56}$$

which can be combined with the corresponding expression provided in Equation (4.54) to determine the remaining unknown z_0. The point of transition between the two possibilities occurs when z_0 falls on the surface of the right-hand plate. Under this unique circumstance, the value of z_0 is known which means the result of Equation (4.54) can instead be used to identify the crossover point between the two regimes in the parameter space:

$$\Lambda^5 M^3 = \left(4\ell^4\right)^{1/3} y_L^2 \rho_L \left\{ \arccos\sqrt{\frac{y_L}{y_L + x_L^2}} + \frac{y_L^{1/2} x_L}{y_L + x_L^2} \right\}^{-4/3} , \tag{4.57}$$

with the parameters x_L and y_L still given by Equation (4.56). In the above, satisfying the inequality corresponds to the loss of a central field maxima. Furthermore, the right-hand side is completely determined by the plate densities ρ_L, ρ_R and the plate separation ℓ. Therefore, the above inequality can be used to determine the correct regime for a given set of model parameters M and Λ.

In working directly with the implicit field equation of Equation (4.13), a set of four deterministic equations for the systems unknowns ϕ_0, z_0, δ_L and δ_R can be recovered without having to rely on any approximations. As a result, the method discussed here is self-contained meaning it is applicable across the entire chameleon parameter space. Although requiring an element of numerical analysis, the approach is considerably more versatile than the alternative. For this reason, the data presented in the next section which focuses on applying an asymmetric plate configuration to an atom interferometry experiment, was gathered exclusively using the semi-analytic method.

4.3 Atom Interferometry

The asymmetric chameleon field profile will produce a force on any particles travelling between the plates which could be detected in a sufficiently sensitive experiment. One option could be to perform a classical deflection experiment, firing a beam of particles between the plates, and measuring the deviation from straight line motion in order to constrain the chameleon. Recently it has been shown that experiments using atom interferometry are particularly sensitive probes of the chameleon field [40, 64, 83]. This is due to the fact that in a laboratory vacuum atoms are not screened from the chameleon field over a broad region of the chameleon parameter space, in addition the nature of the experiment means that it can be sensitive to extremely small forces acting on the individual atoms. This motivates combining our asymmetric plate scenario with an atom interferometry measurement.

Atom interferometry divides the wave function of an atom into a superposition of two states, which traverse spatially separated paths before later being recombined. The phase of each state becomes a function of the path that has been traversed, and when the two states are combined the differing phases of the two possible states of the wave-function result in an interference pattern. The probability of measuring the atom to be in one of the two states therefore becomes a function of the forces that have acted on the atom during the evolution. This section will focus on demonstrating the capability of an experiment adopting an asymmetric plate configuration. The results are based upon a set-up where one of the two paths

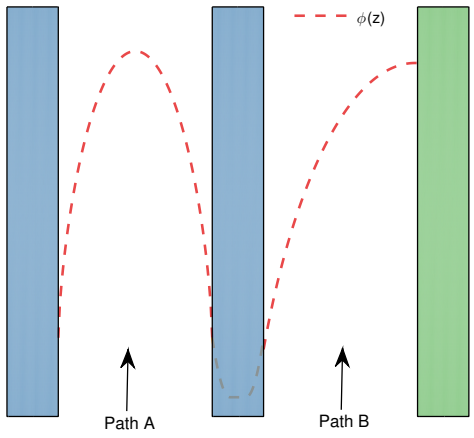

Figure 4.1: The three plate configuration proposed for use in an atom interferometry experiment. The right most (green) plate is less dense than the left and central (blue) plates, giving rise to the chameleon field profile indicated by the red dashed line.

explored by the wave-function traverses an asymmetric chameleon profile whilst the other path passes between a symmetric plate configuration, as shown in Figure 4.1. To simplify the calculation it is assumed that incident atomic beams are taken to enter exactly halfway between neighbouring plates. This allows for the symmetric path to be used as a reference, as particles avoid both gravitational and chameleon forces.

The experiment measures the phase difference accumulated along the two paths which has two parts. The first is proportional to the difference in the classical action evaluated along each path [81, 121], and the second is imprinted by the interactions with the laser beams used to manipulate the atoms. In essence, the atoms pick up a phase proportional to $k_{\rm eff}$ for each interaction where $k_{\rm eff}$ is the effective wave-number associated with the hyperfine splitting transition of the atom.

Collecting the Contributions towards the Phase Difference

The first contribution towards the phase difference measured within an atom interferometry experiment to consider is that sourced by an atomic path difference between the two trajectories. In working in natural units, this is given exactly by the difference in the classical action of test particles traversing these two paths. Writing the Lagrangian for particles traversing the left and right hand routes as $\mathcal{L}_A$ and $\mathcal{L}_B$ respectively, the phase difference at the level of the action, denoted $\Delta^{(A)}$, is therefore given by

$$\Delta^{(A)} = \int_0^T \mathrm{d}t\, \mathcal{L}_A - \int_0^T \mathrm{d}t\, \mathcal{L}_B \,, \tag{4.58}$$

where without loss of generality, the interval of the time coordinate t has been specified to span between 0 and T, where T is the net exposure time of the experiment. Particles can

be taken to approach the plates in the y-direction, having the z coordinate reserved for the position between the two plates. With such, the classical Lagrangian for a particle moving through a potential sourced by the chameleon field is given by

$$\mathcal{L}_i = \frac{1}{2}\left(\dot{z}_i^2 + \dot{y}_i^2\right) + \frac{\phi\left(z_i\right)}{M}\,, \qquad i \in (A, B)\,, \tag{4.59}$$

the potential term here following from the force law $F_\phi = -\nabla\phi/M$ and co-ordinate indices A and B specifying the associated path. As there is no source of acceleration perpendicular to the planar-surfaces, action contributions from motion along the y direction exactly cancel between the two paths. For the symmetric case, entering exactly in between the two plates also ensures that the z contribution can be omitted. Taking path A as the symmetric and B the antisymmetric to match with the configuration presented in Figure 4.1 leads to the result

$$\Delta^{(A)} = \int_0^T \mathrm{d}t \quad \left[\frac{1}{2}\dot{z}_B^2 + \frac{\phi_R(z_B)}{M} - \frac{\phi_L(z_A)}{M}\right]\,. \tag{4.60}$$

Due to the implicit form of Equation (4.13) describing the chameleon field between the plates, generally numerical methods are required to evaluate this integral. This can be achieved with the implementation of a finite difference scheme, where each particle trajectory can be identified by iteratively evolving in small increments of time. For each time interval δt corresponding to a given iteration n, the associated contribution toward the action $\delta_n^{(A)}$ is given by

$$\delta_n^{(A)} = \delta t \left\{\frac{1}{2}\dot{z_B}^2 + \frac{\phi_R(z_B)}{M} - \frac{\phi_L(z_A)}{M}\right\}_{t=n\delta t}\,, \tag{4.61}$$

from which it follows that the net difference emerging between the two paths is

$$\Delta^{(A)} = \sum_n \delta_n^{(A)}\,. \tag{4.62}$$

Outside of numerical integration, it is possible to obtain an analytic estimate for the integral of Equation (4.60) if the deviation of the particle path from a straight line is sufficiently small. In this case it is useful to consider the expansion of the scalar field to linear order around its central value. As detailed in the appendix, expanding the chameleon potential to first order around the central position between the two anti-symmetric plates gives an expression for a constant force per unit mass in the proximate region. This is found to be

$$F_\phi = \frac{1}{M}\sqrt{\frac{2\Lambda^5}{\phi_0}}\sqrt{\frac{\phi_0}{\phi_C} - 1}\,, \tag{4.63}$$

with ϕ_C corresponding to the central value of the field. To follow, the central values pertaining to paths A and B will be denoted ϕ_A and ϕ_B respectively. This allows for the scalar field term appearing in the action to be written as a perturbative expansion around the central value:

$$\frac{\phi(z_i)}{M} = \frac{\phi_i}{M} + \left\{(z_i - z_C^{(i)})\right\} F_\phi^{(i)}\,, \qquad i \in (A, B)\,, \tag{4.64}$$

with $z_C^{(A)}$ and $z_C^{(B)}$ corresponding to the z value falling exactly between the plates corresponding to paths A and B respectively. Remembering that the force term vanishes in the symmetric case, the phase component can be written as

$$\Delta^{(A)} = \int_0^T \mathrm{d}t \;\; \frac{1}{2}\dot{z}_B^2 + F_\phi^{(B)} z_B + \frac{1}{M}(\phi_B - \phi_A) \; . \tag{4.65}$$

The above can be simplified by solving the Euler-Lagrange equations for the two paths, the result of which is easily integrated to find that

$$\Delta^{(A)} = \frac{1}{3} a_\phi^2 T^3 + \frac{1}{M} \left\{\phi_B - \phi_A\right\} T \; , \tag{4.66}$$

where $a_\phi \coloneqq F_\phi^{(R)}$ is the constant chameleon acceleration experienced throughout the asymmetric path.

In addition to the phase difference sourced at the level of the classical action, the photons used to manipulate the atomic clouds within the experiment are also found to carry phase information. Assuming that the atoms are kicked by the lasers just before they enter the plates, to put them on the correct path, and just after exiting the plates, in order to recombine them, the net contribution from these interactions $\Delta^{(P)}$ is given by

$$\Delta^{(P)} = k_{\mathrm{eff}} a_\phi T^2 \; . \tag{4.67}$$

Combining Equations (4.66) and (4.67), the net phase difference can be seen to consist of two competing factors: one that depends on the acceleration (proportional to the gradient of the chameleon field) and one that depends on the scalar potential. As illustrated in Figure 4.1, the central acceleration can be increased by increasing the density asymmetry but this is at the expense of decreasing the central field value. Conversely, the phase difference due to the scalar potential terms can be increased by allowing the separation between the two sets of plates to vary. In moving to a larger plate separation for path B, the field is able to reach a higher central value. As a side note, current atom interferometry constraints on the chameleon field come from considering a spherical source object where the two atomic beams are subject to a uniform chameleon field. This in turn drives the action contribution to zero which is not the case for the experiment described in this chapter.

Phase Differences across the Model Parameter Space

Having collected the various contributions towards the measured phase difference, it's now possible to study the constraining potential of the proposed asymmetric plate configuration when introduced to an atom interferometry experiment targeting the chameleon field. Figures 4.2 and 4.3 demonstrate the power of this experiment for two choices of plate separation, and time of flight T of the atoms between the plates. Experimental parameters for the vacuum chamber are chosen to correspond to those used in Reference [64]. Further, it is assumed that the atomic beams are composed of Caesium atoms and density values have been set to be $1\,\mathrm{gcm}^{-3}$ and $20\,\mathrm{gcm}^{-3}$ for the low and high density plates respectively. Moving from left to right in both of these figures indicates an increase in exposure time from $T = 30\,\mathrm{ms}$, to

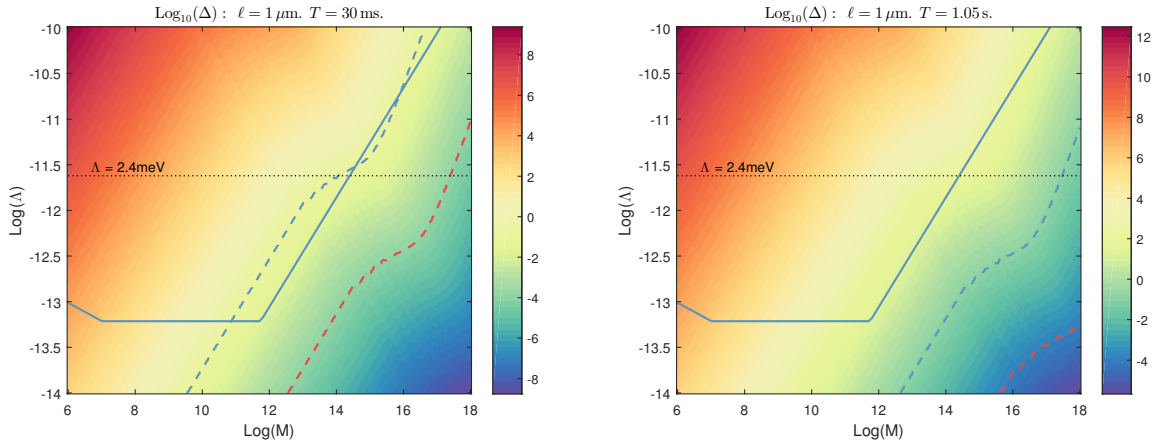

Figure 4.2: The phase difference $\Delta = \Delta^{(A)} + \Delta^{(P)}$ of the wave-function accumulated along the two paths indicated in Figure 4.1, for plates separated by $\ell = 10^{-6}\,\mathrm{m}$. Values for the interferometry experiment are chosen to be those of the configuration described in Reference [64]. It is assumed that the experiment is placed centrally in a 10 cm-radius vacuum chamber containing 10^{-10} Torr of hydrogen. Moving left to right corresponds to an increase in the exposure time T from 30 ms to 1.05 s. Regions above the blue dashed line could be excluded by an experiment sensitive to accelerations down to $10^{-6}\,g$, at which level systematic errors can be neglected. Moving to an experiment sensitive to $10^{-9}\,g$ would push the exclusion limits down to the red dashed line. The region above the solid line has been excluded in Reference [83].

the more optimistic $T = 1.05\,\mathrm{s}$ proposed in [122]. As a side note, current constraints from astrophysical and cosmological experiments [119, 120] fall entirely outside this window of parameter space, thus are not competitive with an atom interferometry experiment. A first experiment is anticipated to be able to measure accelerations down to $10^{-6}\,g$, where g is the acceleration due to free-fall at the surface of the Earth. If systematics can be controlled it is possible that a sensitivity of $10^{-9}\,g$ could be achieved.

Systematics

It is worth addressing how sensitive the proposed experiment would be to small departures from a parallel configuration. This work has considered perfectly parallel plates for ease of calculation, but there are no special cancellations that rely on this precise geometry. Small departures from parallel will lead to small corrections to the chameleon field profiles presented here. These corrections will have the largest effect when the asymmetry in the field configuration is weak, and the position of the field maxima lies close to the point of injection of the incident beam. In this case, the calculated phase difference relies closely on maximum value of the chameleon field, which can be shown to scale as $\phi_0 \propto L^{2/3}$. Thus, as long as variations in the plate separation along the particle trajectory satisfy $\delta L/L \ll 1$, corrections due to the imperfect alignment of the plates remain small. In the converse scenario, where

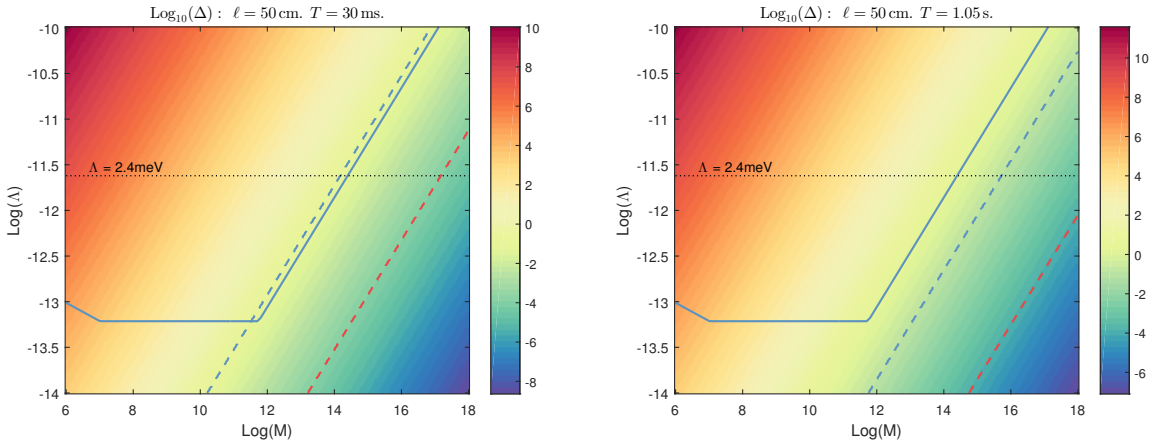

Figure 4.3: As in Figure 4.2 except for the more optimistic plate separation of $\ell = 0.5\,\mathrm{m}$. This would require a beam coherence length of approximately 25 cm which falls within the upper bound proposed in Reference [122]. Current atom interferometry constraints fall on the solid blue line, which would extend to cover the region above the dashed blue line by utilising an asymmetric parallel plate configuration. These limits would shift further to the dashed red line for detectors reaching a precision of $10^{-9}\,g$.

there is a high degree of asymmetry in the field profile, the phase difference as shown in Equation (4.66) is dominated by the acceleration contribution rather than the scalar term. It can be shown that the acceleration remains approximately constant in this limit, thus we argue that small departures from a perfectly parallel configuration would not influence the outcome. One final aspect to consider are the edge effects likely to arise due to the finite length of the plates. As the response to the chameleon to changes in the density field is closely linked to its mass, an heuristic argument could be made that this factor alone largely dictates the outcome. Following this trail of thought, edge effects should be kept to a minimum if the length of the plates is much less than the Compton wavelength of the field. In defining the incident particle velocity as V, this constraint can be more formally contained within the following expression:

$$\max(\lambda_L, \lambda_R) \ll VT\ , \tag{4.68}$$

where the function max(..) returns the maximum value of the arguments supplied. Using this value guarantees that this criteria is satisfied for both plates. The right hand side of the inequality follows from writing the plate length as the product of the two terms.

4.4 Summary

The chapter has introduced a twist on the usual parallel plate configuration used in fifth-force experiments by allowing the densities of the two plates to differ and then considering the trajectories of test particles fired in between them. Applied to the chameleon model, it follows that this density asymmetry leads directly to an asymmetry in the respective

field profile. Having proposed alternate ways to overcome the mathematical complexities of the problem, the take home message was that the asymmetry of the chameleon field profile increases when moving into the part of the chameleon parameter space where it is most weakly coupled. For an experiment conducted for the series of three parallel plates presented in this work, this helps overcome the difficulties in detecting the force mediated by such weakly coupled fields. In the context of atom interferometry, it can be seen from Figure 4.2 that the idea could be implemented to cover most of the remaining chameleon parameter space, and in particular that the the presence of field asymmetry helps push further into the weakly coupled (high M) region of the parameter space. Additionally, such an experiment would improve constraints at small M and Λ which are also hard to reach with current searches. Combining this with the precision of atom interferometry, which uses unscreened atoms as the test particles moving in the chameleon field, it has been shown that such a configuration allows us to reach previously unobtainable parts of the chameleon parameter space.

4.A Parallel Plates and the Parabolic Approximation

The search for the chameleon solution around both spherical and ellipsoidal sources involved utilising a parabolic approximation to describe the effective potential of the lab vacuum region. For this reason, the same approach was followed as an initial attempt to deal with the intermediate region in-between the two parallel plates. As it transpires, the separations between the two planar surfaces relevant to lab based parallel plate experiments challenge the validity of the approximation. Nonetheless, the calculation has been included here as it may still prove useful in the study of large scale structures such as galaxy filaments. The parabolic approximation operates under the assumption that the field does not deviate too far from its potential minima in the region of interest. In this case, the focus is on the space between the two parallel plates, meaning that the assumption is that the field remains proximate to $\phi_B = \phi_{\rm min}\left(\rho_{\rm lab}\right)$ in this region. This approximation allows for a reduction of the effective potential such that

$$\nabla^2\phi = \frac{\partial V_{\rm EFF}}{\partial\phi} \simeq \left(\frac{V_{\rm EFF}}{\partial\phi}\right)_{\phi=\phi_B} + \left(\frac{\partial^2 V_{\rm EFF}}{\partial\phi^2}\right)_{\phi=\phi_B}(\phi-\phi_B) = m_B^2\left(\phi-\phi_B\right) \ . \tag{4.69}$$

The equation above is readily integrated in one dimension to give the composite exponentially suppressed solution:

$$\phi(z) = Ae^{m_B z} + Be^{-m_B z} + \phi_B \ , \tag{4.70}$$

where m_B is defined as the mass of the background field which follows from evaluating $m_\phi\left(\rho_{lab}\right)$. Collecting the equations describing the three remaining regions of interest, the problem reduces to imposing Dirichlet-Neumann boundary conditions onto the following set

of equations:

$$\phi(z) = \frac{\rho_L}{2M}\left(x - (R_1 - \delta_L)\right)^2 + \phi_L \ , \qquad R_1 - \delta_L < z < R_1 \ ,$$

$$\phi(z) = Ae^{m_B z} + Be^{-m_B z} + \phi_B \ , \qquad R_1 < z < R_1 + \ell \ , \tag{4.71}$$

$$\phi(z) = \frac{\rho_R}{2M}\left(x - (R_1 + l + \delta_R)\right)^2 + \phi_R \ , \qquad R_1 + \ell < z < R_1 + \ell + \delta_R \ .$$

Beginning first with the boundary at the surface of the left hand plate at $z = R_1$, enforcing the continuity of the field and its first derivative across the interface leads to

$$\frac{\rho_L}{2M}\delta_L^2 + \phi_L = Ae^{m_B R_1} + Be^{-m_B R_1} + \phi_B \ , \tag{4.72a}$$

$$\frac{\rho_L \delta_L}{M} = m_\phi \left(Ae^{m_B R_1} - Be^{-m_B R_1}\right) \ . \tag{4.72b}$$

Dividing Equation (4.72b) through by m_B and then adding the result to Equation (4.72a) leads to an expression for A:

$$A = \frac{1}{2}\left[\frac{\rho_L}{2M}\left\{\delta_L\left(\delta_L + \frac{2}{m_B}\right)\right\} + (\phi_L - \phi_B)\right] e^{-m_B R_1} \ , \tag{4.73}$$

from which it follows that

$$B = \frac{1}{2}\left[\frac{\rho_L}{2M}\left\{\delta_L\left(\delta_L - \frac{2}{m_B}\right)\right\} + (\phi_L - \phi_B)\right] e^{m_B R_1} \ . \tag{4.74}$$

Moving to the vacuum-plate interface at the right-hand plate, following the same prescription as above leads to additional expressions for the unknowns A and B:

$$\begin{aligned} A &= \frac{1}{2}\left[\frac{\rho_R}{2M}\left\{\delta_R^{(1)}\left(\delta_R^{(1)} + \frac{2}{m_B}\right)\right\} + (\phi_R - \phi_B)\right] e^{-m_B(R_1 + l)} \ , \\ B &= \frac{1}{2}\left[\frac{\rho_R}{2M}\left\{\delta_R^{(2)}\left(\delta_R^{(2)} - \frac{2}{m_B}\right)\right\} + (\phi_R - \phi_B)\right] e^{m_B(R_1 + l)} \ . \end{aligned} \tag{4.75}$$

Equating the two expressions for A and B spanning Equations (4.73), (4.74), and (4.75), leaves two equations to solve for the remaining unknowns δ_L and δ_R:

$$\begin{aligned} &\left[\frac{\rho_L}{2M}\left\{\delta_L\left(\delta_L + \frac{2}{m_B}\right)\right\} + (\phi_L - \phi_B)\right] \\ &\qquad = \left[\frac{\rho_R}{2M}\left\{\delta_R\left(\delta_R + \frac{2}{m_B}\right)\right\} + (\phi_R - \phi_B)\right] e^{-m_B l} \ , \end{aligned} \tag{4.76a}$$

$$\left[\frac{\rho_L}{2M}\left\{\delta_L\left(\delta_L-\frac{2}{m_B}\right)\right\}+(\phi_L-\phi_B)\right] = \left[\frac{\rho_R}{2M}\left\{\delta_R\left(\delta_R-\frac{2}{m_B}\right)\right\}+(\phi_R-\phi_B)\right]e^{m_B l}\ . \tag{4.76b}$$

Adding together Equations (4.76a) and (4.76b) leads to the result

$$\frac{\rho_L\delta_L^2}{M}+2(\phi_L-\phi_B)=2\cosh(m_B)\left\{\frac{\rho_R}{2M}\delta_R^2+(\phi_R-\phi_B)\right\}-2\sinh(m_B l)\frac{\rho_R}{M}\frac{\delta_R}{m_B}\ . \tag{4.77}$$

At this point it becomes necessary to account for the (very) small value of the mass m_B by Taylor expanding the hyperbolic functions and dropping any sub-leading order terms in m_B. Taking $\cosh(m_B l)\simeq 1$ and $\sinh(m_B l)\simeq m_\phi l$ the above reduces to

$$\frac{\rho_L\delta_L^2}{M}+2(\phi_L-\phi_B)=\frac{\rho_R}{M}\delta_R\left(\delta_R-2l\right)\ . \tag{4.78}$$

Further, subtracting Equation (4.76a) from Equation (4.76b) is found to lead to a shell-density relation:

$$\begin{aligned}\frac{\rho_L}{M}\frac{2\delta_L}{m_B}&=\cosh(m_B l)\frac{\rho_R}{M}\frac{2\delta_R}{m_B}-2\sinh(m_B l)\left[\frac{\rho_R}{2M}\left(\delta_R\right)^2+(\phi_R-\phi_B)\right]\\ &\simeq\frac{\rho_R}{M}\frac{2\delta_R}{m_B}\ ,\end{aligned} \tag{4.79}$$

where the constant coefficients cancel to give

$$\rho_L\delta_L=\rho_R\delta_R\ . \tag{4.80}$$

The result stated above (Equation (4.80)) may be incorporated into Equation (4.78) to produce a quadratic equation for δ_R (or δ_L) by eliminating the other. After a little manipulation, this reads

$$(\rho_L\rho_R-\rho_R^2)\delta_R^2-2\rho_L\rho_R l\delta_R+2M\rho_L\left(\phi_L-\phi_R\right)\ , \tag{4.81}$$

for which the solutions take the form

$$\delta_R=\frac{\rho_L\rho_R\, l\pm\sqrt{\rho_L^2\rho_R^2 l^2-2M\rho_L\rho_R\left(\rho_L-\rho_R\right)\left(\phi_L-\phi_R\right)}}{\rho_R\left(\rho_L-\rho_R\right)}\ . \tag{4.82}$$

Making use of the identity for the field minima $\phi_{\min}(\rho)=\left(\Lambda^5 M/\rho\right)^{1/2}$ the above can be written entirely in terms of the plate densities in conjunction with the two model parameters M and Λ:

$$\delta_R=\rho_L\left\{\frac{l\pm\sqrt{l^2-2M^{3/2}\Lambda^{5/2}\left(\rho_L\rho_R\right)^{-3/2}\left(\rho_L-\rho_R\right)\left(\rho_R^{1/2}-\rho_L^{1/2}\right)}}{\left(\rho_L-\rho_R\right)}\right\}\ . \tag{4.83}$$

this is ensured to generate real solutions as the discriminant of the above is always positive given that $\left(\rho_L-\rho_R\right)\left(\rho_R^{1/2}-\rho_L^{1/2}\right)\leq 0$ for all ρ_L,ρ_R. Further, to ensure regularity upon approaching $\rho_R=\rho_L$, the negative root must be taken in the above.

4.B The Constant Force Approximation

An argument presented in the main body of the text was that for sufficiently small deviations from the particle's incident position, the chameleon field profile can be treated as approximately linear resulting in a constant value for the exerted force. Arriving at the results used involved expanding the implicit field equation for $\phi(z)$ around some central value, denoted ϕ_C. Making small perturbations around this field value, and the corresponding central position z_C, it becomes useful to write

$$\phi = \phi_C\,(1+\psi)\,, \quad z = z_C\,(1+\zeta)\ , \qquad \psi,\zeta \ll 1\ . \tag{4.84}$$

Expanding the implicit field equation to leading order in $\delta\phi$ leads to the result

$$\mp\left(\sqrt{\frac{2\Lambda^5}{\phi_0^3}}z_C\right)\zeta = -\left(\frac{\phi_C^2}{\phi_0\left(\phi_C\phi_0-\phi_C^2\right)^{1/2}}\right)\psi\ , \tag{4.85}$$

which can be shown to remain valid as long as

$$\psi \ll 4\left(1-\frac{\phi_C}{\phi_0}\right)\ . \tag{4.86}$$

Invoking the chain rule it is then possible to recover an expression for the gradient of the field through the relation

$$\frac{\partial\phi}{\partial z} = \left(\frac{\partial\phi}{\partial\psi}\right)\left(\frac{\partial\psi}{\partial\zeta}\right)\left(\frac{\partial\zeta}{\partial z}\right)\ , \tag{4.87}$$

from which it follows that

$$\frac{\partial\phi}{\partial z} = \sqrt{\frac{2\Lambda^5}{\phi_0}}\left(\frac{\phi_0}{\phi_C}-1\right)^{1/2}\ . \tag{4.88}$$

The scalar acceleration is then simply calculated by recalling the identity $a_\phi = -\nabla\phi/M$. To make use of the above result, it is required that the linear approximation remains valid throughout the duration of the atom interferometry experiment. Taking an incident particle with motion initially confined to the y direction, the displacement along the z axis after exposure time T is given by

$$\delta z = \frac{T^2}{2M}\sqrt{\frac{2\Lambda^5}{\phi_0}}\left(\frac{\phi_0}{\phi_C}-1\right)^{1/2}\ . \tag{4.89}$$

Further, the consistency condition of Equation (4.86) can be rephrased in terms of the perturbation around the central position $\delta z = z_C\zeta$ as follows:

$$\delta z \ll 2\left[\frac{2\phi_C^3}{\Lambda^5}\left(1-\frac{\phi_C}{\phi_0}\right)\right]^{1/2}\ . \tag{4.90}$$

Combining the preceding two results, it can be found that the particle remains within the regime of constant acceleration provided that the following condition is satisfied:

$$T \ll 2\frac{M}{\Lambda^5}\phi_C\ . \tag{4.91}$$

Performing a scan across the entire chameleon parameter space revealed that this inequality is easier satisfied when moving to higher values of M and Λ, as to be naively expected by examining the above. Importantly, it was found to remain completely consistent in the region of the parameter space of most interest: that yet to be explored and constrained by fifth-force searches.

Chapter 5

Closing Remarks

Dynamically screened scalar fields first appeared in the literature in search for alternatives to the Λ-CDM paradigm. The most extensively studied example is the chameleon model, which inherits an environmentally dependent field mass as a result of the interplay between non-linear self interaction terms and a density component within the scalar effective potential. A direct consequence of this, is a screening mechanism which becomes active in regions of sufficiently high density, acting to inhibit both the interaction strength and range of the chameleon fifth force. As a result, the chameleon field, and indeed the other models of dynamically screened scalar fields, are able to hide from the tight constraints placed on the allowed departures from General Relativity within the regime that gravity has been exhaustively tested.

On the other hand, the behaviour of density dependent screening implies that the propagation of the scalar mediated fifth force favours environments of lower density. Ultimately, this suggests that any signatures of the chameleon force should begin to resurface under the conditions offered by the current generation of vacuum based experiments. The most powerful experimental technique to date for measuring absolute forces is atom interferometry, which has enabled us to push far deeper into previously uncharted regions of the chameleon parameter space. However, what remains to be explored corresponds to a regime of weak coupling governed by the non-linear effects of the screening process. Because of this, one has to battle both the inherent weakening of the force due to a weak matter coupling, and the reduction of the force due to screening. The target of the research presented here was to understand whether or not the effects of screening could be mitigated, with the hope of making the challenge of probing the currently unconstrained segment of the model parameter space a little easier.

At the heart of this work, has been the unique field structure of the chameleon field, which essentially confines force contributions to a thin-shell at the surface of the matter source. In moving away from the conventional spherical source object, it was demonstrated in Chapter 2 that the extent of the shell region responds favourably to the deformation of a sphere into an ellipsoid. In this case, the analyses indicated that the extra structural degree of freedom associated with the existence of a shell region allows the internal chameleon field to readjust in such a way to preserve the amount of force contributing matter sources. This is in con-

trast to the gravitational force which is found to weaken with the deformation. The practical applications of this conclusion were fairly limited however, as the results presented were primarily concerned with the ratio between the gravitational and chameleon forces, providing no tangible measure of the change in absolute acceleration relevant to an interferometry experiment. Nonetheless, it was clear that the consideration of alternative source geometries was a step in the right direction when it comes to controlling the efficiency of the screening process.

The positive results of the fully analytic study of the chameleon field around an ellipsoidal source object inspired further research into the connection between chameleon screening behaviour and the source geometry. In Chapter 3, a more systematic means of comparing source geometries was presented which involved the implementation of the chameleon model into a numerical finite element platform. This numerical treatment of the problem was applicable across a wide range of source geometries. Making reference to the precious analytic study of the ellipsoid, the results were in support of the conclusion that ellipticity weakens chameleon screening. The implications had more practical relevance here however, as the numerical approach was used to extract values of absolute acceleration, where a notable advantage over the spherical acceleration was observed when moving into the screened regime. In addition to this, it was possible to introduce procedurally generated source objects which were then compared across a large sample space in order to identify an optimised geometry. At the weak coupling limit of $M = M_{\rm PL}$, this optimal source was able to realise a considerable gain over the chameleon force surrounding a spherical object. Broadly speaking, the work in Chapter 3 reinforced the notion that departures from a spherically symmetric source can be used to increase prospects of detection. However, a side effect of this research was to demonstrate the efficiency and versatility of the finite element method in the study of dynamically screened scalar field theories. Following this method, the application of these models to a host of different experiments is very easily accessible, where constraints in principle could be generated with a considerably reduced simulation time when compared to the conventional finite difference approach.

Chapter 4 studied the non-linearities of the chameleon theory in a slightly different light, where the idea was to change the format of the experiment to exploit the density dependence of the chameleon screening mechanism. By introducing a twist on the conventional parallel plate setup by allowing the densities of the individual plates to vary, it was shown that the resulting asymmetries in the chameleon field profile give rise to additional contributions to the atomic phase difference sourced by differences in the classical action. The nature of this setup also manages to bypass the screening effects arising due to the finite size of the vacuum chamber, which is known to limit the constraining potential of an atom interferometry experiment focussing on a single source object at the centre of the chamber. Collectively, it was demonstrated that an atom interferometry experiment utilising asymmetric parallel plates could be used to close in on what remains of the chameleon parameter space.

To close, the cosmology of the chameleon has come under increased scrutiny in recently years, leaving its viability as an alternative to Λ-CDM in question. Nonetheless, the dynamical properties of the chameleon offer an interesting mechanism for screening long range interactions of light scalar fields, providing an interesting avenue of study independent of ties to

the late time accelerated expansion of the universe. Thus, if nothing else, the chameleon can be used as a playground to develop a deeper understanding of the phenomenological effects tied to a dynamically screened scalar emerging more naturally from high energies theories. Hopefully, this work has demonstrated to the reader that with a little extra thought going into the ingredients of an experimental setup, the detrimental effects of screening can in some sense be harnessed to generate tighter constraints on a model parameter space.

[1] A. G. Riess *et al.*, "Observational Evidence from Supernovae for an Accelerating Universe and a Cosmological Constant", Astron. J. 116 (1998) 1009-1038.

[2] S. Perlmutter *et al.*, "Measurements of Omega and Lambda from 42 High Redshift Supernovae", Astrophys. J. 517 (1999) 565-586.

[3] S. J. Maddox *et al.*, "Galaxy Correlations on Large Scales", Mon. Not. Roy. Astron. Soc. 242 (1990) 43-49.

[4] G. Efstathiou *et al.*, "The Cosmological Constant and Dark Matter", Nature 348 (1990) 705-707.

[5] G. F. Smoot *et al.*, "Structure in the COBE differential microwave radiometer first year maps", Astrophys. J. 396 (1992) L1-L5.

[6] M. J. Pierce *et al.*, "The Hubble Constant and Virgo Cluster Distance from Observations of Cepheid Variables", Nature 371 (1994) 385-389.

[7] W. L. Freedman *et al.*, "Distance to the Virgo Cluster Galaxy M100 from Hubble Space Telescope Observations of Cepheids", Nature 371 (1994) 757-762.

[8] M. Tegmark *et al.*, "Cosmological Parameters from SDSS and WMAP", Phys. Rev. D 69 (2004) 103501.

[9] K. S. Dawson *et al.*, "The Baryon Oscillation Spectroscopic Surver of SDSS-III", Astron.J. 145 (2013).

[10] A. Balbi, P. Ade, J. Bock, J. Borrill, A.Boscalari, *et al.*, "Constraints on Cosmological Parameters from MAXIMA-1", Astrophy. J. 545 (2000) L1-L4.

[11] A. E. Lange *et al.*, "Cosmological Parameters from the First Results of BOOMERANG", Phys. Rev. D 63 (2001) 042901.

[12] G. Hinshaw *et al.*, "Nine-Year Wilkinson Microwave Anisotropy Probe (WMAP) Observations: Cosmological Parameter Results", Astrophys. J. Suppl. 208 (2013) 19.

[13] P. Ade *et al.*, "Planck 2013 Results. XVI. Cosmological Parameters", Astron. Astrophys. 571 (2014) A16.

[14] J. Khoury, "Chameleon Field Theories", Class. Quant. Grav. 30 (2013) 214004.

[15] D.H. Weinberg *et al.*, "Observational Probes of Cosmic Acceleration", Phys. Rept. 530 (2013) 87-255.

[16] A. Einstein, "Cosmological Considerations in the General Theory of Relativity", Sitzungsber. Preuss. Akad. Wiss. Berling (Math.Phys.) 1917 142-152.

[17] E. Hubble, "A relation between distance and radial velocity among extra-galactic nebulae", Proc. Nat. Acad. Scid. 15 (1929) 168-173.

[18] Ya. B. Zel'dovich, "The Cosmological Constant and the Theory of Elementary Particles", Sov. Phys. Usp. 11 (1968) 381-393.

[19] Planck Collaboration, "Planck 2015 Results. I. Overview of Products and Scientific Results", Astron. Astrophys. 594 (2016) A1.

[20] H. E. S. Velten *et al.*, "Aspects of the Cosmological Coincidence Problem", Eur. Phys. J. C74 (2014) 3160.

[21] T. Clifton, P. G. Ferriera, A. Padilla and C. Skordis, "Modified Gravity and Cosmology", Phys. Rept. 513 (2012) 1-189.

[22] E. J. Copeland, M. Semi and S. Tsujikawa, "Dynamics of Dark Energy", Int. J. Mod. Phys D15 (2006) 1753-1936.

[23] T. P. Sotiriou, "Gravity and Scalar Fields", Lect. Notes Phys. 892 (2015) 3-24.

[24] A. Coc *et al.*, "Variation of Fundamental constant and the role of $A = 5$ and $A = 8$ nuclei on primordial nucleasynthesis", Phys. Rev. D 86 (2012) 043529.

[25] J. C. Berengut *et al.*, "Varying the light quark mass: Impact on the nuclear force and big bang nucleosynthesis", Phys. Rev. D 87 (2013) 085018.

[26] A. L. Erickcek, N. Barnaby, C. Burrage, and Z. Huang, "Chameleons in the Early Universe: Kicks, Rebounds and Particle Production", Phys. Rev. D 89 (2014) 084074.)

[27] A. Padilla *et al.*, "How to avoid a swift kick in the chameleons", JCAP 1603 (2016) 058.

[28] C. Burrage, J. Sakstein, "A Compendium of Chameleon Constraints", JCAP 1611 (2016) 045.

[29] J. A. Frieman *et al.*, "Dark Energy and the Accelerating Universe", Ann. Rev. Astron. Astrophys. 46 (2008) 385-432.

[30] S. M. Carroll, "The Cosmological Constant", Living Rev. Rel. 4 (2001) 1.

[31] P. Brax, C. van de Bruck, A.-C David, and D. J. Shaw, "$f(R)$ Gravity and Chameleon Theories", Phys. Rev. D 78 (2008) 104021.

[32] A. Joyce *et al.*, "Dark Energy vs. Modified Gravity", Ann. Rev. Nucl. Part. Sci. 66 (2016) 95-122.

[33] P. Brax, "Lectures on Screened Modified Gravity", Acta Phys. Polon B43 (2012) 2307-2329.

[34] B. Ratra and P.J.E. Peebles, "Cosmological Consequences of a Rolling Scalar Field", Phys. Rev. D 37 (1988) 3406.

[35] A. Joyce *et al.*, "Beyond the Standard Cosmological Model", Phys. Rept. 568 (2015) 1-98.

[36] P. Steinhardt, L. Wang, I. Zlatev, "Cosmological Tracking Solutions", Phys. Rev. D 59 (1999) 123504.

[37] I. Zlatev, L. Wang, P. J. Steinhardt, "Quintessence, Cosmic Coincidence, and the Cosmological Constant", Phys. Rev. Lett. 82 (1999) 896-899.

[38] E. Babichev end Cdric Deffayet, "An Introduction to the Vainshtein Mechanism", Class. Quant. Grav. 30 (2013) 184001.

[39] J. Khoury and A. Weltman, "Chameleon Fields: Awaiting Surprises for Tests of Gravity in Space", Phys. Rev. Lett. 93, 171104 (2004) 171104.

[40] C. Burrage and E. J. Copeland, "Using Atom Interferometry to Detect Dark Energy", Contemp. Phys. 57 (2016) 164-176.

[41] P. Brax *et al.*, "A Unified Description of Screened Modified Gravity", Phys. Rev. D 86 (2012) 044015.

[42] K. Hinterbichler *et al.*, "Symmetron Cosmology", Phys. Rev. D 84 (2011) 103521.

[43] R. Bean *et al.*, "Adiabatic Instability in Coupled Dark Energy - Dark Matter Models",

Phys. Rev. D 78 (2008) 023009.

[44] T. Damour and A. M. Polyakov, "The String Dilaton and a Least Coupling Principle", Nucl. Phys. B423 (1994) 532-558.

[45] P. Brax, C. van de Bruck, A. C. Davis and D. Shaw, "The Dilaton and Modified Gravity", Phys. Rev. D 82 (2010) 063519.

[46] D. Langlois and K. Noui, "Degenerate High Derivative Theories Beyond Horndeski: Evading the Ostrogradki Instability", JCAP 1602 (2016) 034.

[47] Jérôme Gleyzes *et al.*, "Healthy Theories beyond Horndeski", Phys. Rev. Lett. 114 (2015) 211101.

[48] C. Deffayet *et al.*, "From k-essence to generalised Galileons", Phys. Rev. D 84 (2011) 064039.

[49] G. Horndeski, "Second-Order Scalar-tensor Field Equations in a Four Dimensional Space", Int. J. Theor. Phys. 10 363 (1974) 363-384.

[50] C. Deffayet and D. A. Steer, "A Formal Introduction to Horndeski and Galileon Theories and their Generalisations", Class. Quant. Grav. 30 (2013) 214006.

[51] A. Barreira *et al.*, "Nonlinear Structure Formation in the Cubic Galileon Gravity Model", JCAP 1310 (2013) 027.

[52] M. Fierz and W. Pauli, "On Relativistic Wave Equations for Particles of Arbitrary Spin in an Electromagnetic Field", Proc. Roy. Soc. Lond. A173 (1939) 211-232.

[53] H. van Dam and M. J. G. Veltman, "Massive and Massless Yang-Mills and Gravitational Fields", Nucl. Phys. B22 (1970) 397-411.

[54] A. I. Vainshtein, "To the Problem of Non-vanishing Gravitation Mass", Phys. Lett. B39 (1972) 393-394.

[55] C. de Rham and G. Gabadadze, "Generalisation of the Fierz-Pauli Action", Phys. Rev. D 82 (2010) 044020.

[56] S.F. Hassan and R. A. Rosen, "Resolving the Ghost Problem in Nonlinear Massive Gravity", Phys. Rev. Lett. 108 (2012) 041101.

[57] G. R. Dvali *et al.*, "4D Gravity on a Brane in 5D Minkowski Space", Phys. Lett. B485 (2000) 208-214.

[58] R. Maartens and K. Koyama, "Brane-World Gravity", Living Rev. Rel. 7 (2004) 7.

[59] A.C. Davis *et al.*, "Astrophysical Black Holes in Screened Modified Gravity", JCAP 1408 (2014) 033.

[60] J. Khoury and A. Weltman, "Chameleon Cosmology", Phys. Rev. D 69 (2004) 044026.

[61] T.P. Waterhouse, "An Introduction to Chameleon Gravity", arXiv:astro-ph/0611816v1 (2006).

[62] P. Brax, C. van de Bruck, A.-C Davis, J. Khoury, and Amanda Weltman, "Detecting Dark Energy in Orbit - the Cosmological Chameleon", Phys. Rev. D 70 (2004) 123518.

[63] A. N. Ivanov and M. Wellenzohn, "Can Chameleon Field be identified with Quintessence?", arXiv:1607.00884v1 (2016).

[64] C. Burrage, E. J. Copeland, E. A. Hinds, "Probing Dark Energy with Atom Interferometry", JCAP 1503 042 (2015) 042.

[65] EUCLID Theory Working Group Collaboration, "Cosmology and Fundamental Physics with the Euclid Satellite", Living Rev. Rel. 16 (2013) 6.

[66] Dark Energy Survey Collaboration, "The Dark Energy Survey: more than dark energy - an overview", Mon. Not. Roy. Astron. Soc. 460 (2016) 1270-1299.

[67] J. Redondo and A. Ringwald, "Light Shining Through Walls", Contemp. Phys. 52 (2011) 211-236.

[68] M. Ahlers *et al.*, "Alphenglow - A Signature for Chameleons in Axion-Like Particle Search Experiments", Phys. Rev. D 77 (2008) 015018.

[69] H. Gies *et al.*, "Hidden in the Light: Magnetically Induced Afterglow from Trapped Chameleon Fields", Phys. Rev. D 77 (2008) 025016.

[70] P. G. Roll, R. Krotkov and R.K. Dicke, "The Equivalence of Inertial and Passive Gravitational Mass", Annals Phys. 26 (1964) 442-517.

[71] T. Wagner *et al.*, "Torsion-balance tests of the weak equivalence principle", Class. Quant. Grav. 29 (2012) 184002.

[72] E. Fischbach *et al.*, "Reanalysis of the Eötvös experiment", Phys. Rev. Lett. 56 (1986) 3.

[73] E. G. Adelberger *et al.*, "Particle Physics Implications of a Recent Test of the Gravitational Inverse-Square law", Phys. Rev. Lee. 98 (2007) 131104.

[74] A. Beyer *et al.*, "Precision Spectroscopy of Atomic Hydrogen", J. Phys. Conf. Ser. 467 (2013) 012003.

[75] P. Brax and C. Burrage, "Atomic Precision Tests and Light Scalar Couplings", Phys. Rev. D 83 (2011) 035020.

[76] V. P. Chebotayev *et al.*, "Interference of Atoms in Separated Optical Fields", J. Opt. Soc. Am. B 2 (1985) 1791-1798.

[77] M. Kasevisch and S. Chu, "Atomic Interferometry Using Stimulated Raman Transitions", Phys. Rev. Lett. 67 (1991) 181-184.

[78] O. Carnal, "Young's Double-Slit Experiment with Atoms", Phys. Rev. Lett. 66 (1991) 2689-2692.

[79] D. W. Keith, "An Interferometer for Atoms", Phys. Rev. lett. 66 (1991) 2693-2696.

[80] F. Riehle, "Optical Ramsey Spectroscopy in a Rotating Frame: Sagnac Effect in a Matter-wave Interferometer", Phys. Rev. Lett. 67 (1991) 177-180.

[81] R. P. Feynman and A. R. Hibbs, "Quantum Mechanics and Path Integrals", New York: McGraw-Hill 1965.

[82] A. Peters *et al.*, "Precision Atom Interferometry", Phil. Trans. R. Soc. A 355 (1997) 2223-2233.

[83] P. Hamilton *et al.*, "Atom-Interferometry Constraints on Dark Energy", Science 349 (2015) 849-851.

[84] A. Peters *et al.*, "High-precision Gravity Measurements using Atom Interferometry", Metrologia 38 01 (2001).

[85] P. Brax, G. Pignol, and D. Roulier, "Probing Strongly Coupled Chameleons with Slow Neutrons", Phys. Rev. D 88 (2013) 083004.

[86] H. Lemmel *et al.*, "Neutron Interferometry Constrains Dark Energy Chameleon Fields", Phys. Lett. B743 (2015) 310-314.

[87] E. Adelberger, B. R. Heckel and A. Nelson, "Tests of The Gravitational Inverse Square Law", Ann. Rev. Nucl. Part. Sci 53 (2003) 77-121.

[88] J. Khoury, "Les Houches Lectures on Physics Beyond the Standard Model of Cosmology", arXiv:1312.2006 [astro-ph.CO] (2013).

[89] K. Hinterbichler and J. Khoury, "Symmetron Fields: Screening Long-Range Forces Through Local Symmetry Restoration", Phys. Rev. Lett. 104 (2010) 231-301.

[90] T. Jenke *et al.*, "Gravity Resonance Spectroscopy Constrains Dark Energy and Dark Matter Scenarios", Phys. Rev. Lett. 112 (2014) 151105.

[91] P. Brax, C. van de Bruck, A. C. Davis, D. J. Shaw and D. Iannuzzi, "Tuning the Mass of Chameleon Fields in Casimir Force Experiments", Phys. Rev. Lett. 104 (2010) 241101.

[92] P. Brax, C. van de Bruck, A. C. Davis, D. F. Mota and D. J. Shaw, "Detecting chameleons through Casimir force measurements", Phys. Rev. D76 (2007) 124034.

[93] J. K. Bloomfield, C. Burrage and A. C. Davis, "The Shape Dependence of Vainshtein Screening", Phys. Rev. D 91 (2015) 083510.

[94] K. Jones-Smith and F. Ferrer, "Detecting Chameleon Dark Energy via Electrostatic Analogy", Phys. Rev. Lett. 108 (2012) 221101.

[95] Y. Fujii and K. Maeda, "The scalar-tensor theory of gravitation", Class. Quantum Grav. 20 (2003).

[96] P. Brax, A. C. Davis and B. Li, "Modified Gravity Tomography", Phys. Lett. B 715 (2012) 38-43.

[97] J. Wang, L. Hui and J. Khoury, "No-Go Theorems for Generalized Chameleon Field Theories", Phys. Rev. Lett. 109 (2012) 241301.

[98] A. Upadhye, W. Hu and J. Khoury, "Quantum Stability of Chameleon Field Theories", Phys. Rev. Lett. 109 (2012) 041301.

[99] A. L. Erickcek, N. Barnaby, C. Burrage and Z. Huang, "Catastrophic Consequences of Kicking the Chameleon", Phys. Rev. Lett. 110 (2013) 171101.

[100] P.M. Morse & H. Feshbach, "Methods of Theoretical Physics Volume I", McGraw-Hill Book Company (1953).

[101] P.M. Morse & H. Feshbach, "Methods of Theoretical Physics Volume II", McGraw-Hill Book Company (1953).

[102] M. Willatzen & L.C.Y. Voon, 'Seperable Boundary-Value Problems in Physics", Wiley-VCH (2011).

[103] C.J. Bouwkamp, "Theoretical and Numerical Treatment of Diffraction Through a Circular Aperture", IEEE Transactions on Antennas and Propagation, Vol AP-18, No.2 (1970).

[104] A. Upadhye, "Dark energy fifth forces in torsion pendulum experiments", Phys. Rev. D 86 (2012) 102003.

[105] D. F. Mota and D. J. Shaw, "Evading Equivalence Principle Violations, Cosmological and other Experimental Constraints in Scalar Field Theories with a Strong Coupling to Matter", Phys. Rev. D 75 (2007) 063501.

[106] R. Gannouji, B. Moraes, D. F. Mota, D. Polarski, S. Tsujikawa and H. A. Winther, "Chameleon dark energy models with characteristic signatures", Phys. Rev. D 82 (2010) 124006.

[107] A.L. Van Buren & J.E. Boisvert, "Accurate Calculation of Prolate Spheriodal Radial Functions of the First Kind and their Derivatives", Quarterly of Applied Mathematics, Volume LX, Number 3 (2002).

[108] A. Rider *et al.*, "Search for Screened interactions Assosciated with Dark Energy Below the 100μm Length Scale", Phys. Rev. Lett. 117 (2016) 101101.

[109] K. Li *et al.*, "Neutron Limit on the Strongly-Coupled Chameleon Field", Phys. Rev. D 93 (2016) 062001.

[110] B. Elder *et al.*, "Chameleon Dark Energy and Atom Interferometry", Phys. Rev. D 94 (2016) 044051.

[111] A. Logg, K.-A. Mardal, and G. Wells, "Automated Solution of Differential Equations by the Finite Element Method", Springer 9783642230998 (2012).

[112] G. Strang, "Piecewise Polynomials and the Finite Element Method", Bulletin. Amer. Math. Soc. 79 (1973) 1128-1137.

[113] J. Peiro and S. Sherwin, "Finite Difference, Finite Element and Finite Volume Methods for Partial Differential Equations", Handbook of Materials Modelling, Springer (2005).

[114] J. W. Barrett, "The Asymmetric Monopole and Non-Newtonian Forces", Nature 341 (1989) 131-132.

[115] F.-J Sayas, "A Gentle Introduction to the Finite Element Method", (2008).

[116] A. N. Ivanov, R. Hollwieser, T. Jenke, M. Wellenzohen and H. Abele, "Influence of the Chameleon Field Potential on Transition Frequencies of Gravitationally Bound Quantum States of Ultracold Neutrons", Phys. Rev. D 87 (2013) 105013.

[117] A. Almasi, P. Brax, D. Iannuzzi and R. I. Sedmik, "Force Sensor for Chameleon and Casimir Force Experiments with Parallel-plate Configuration", Phys. Rev. D 91 (2015) 102002.

[118] P. Brax and A.-C Davis, Casimir, "Gravitational and Neutron Tests of Dark Energy", Phys. Rev. D. 91 (2015) 063503.

[119] B. Jain, V. Vikram and J. Sakstein, "Astrophysical Tests of Modified Gravity: Constraints from Distance Indicators in the Nearby Universe", Astrophys. J. 779 (2013) 39.

[120] V. Vikram, J. Sakstein, C. Davis, and A. Neil, "Astrophysics Tests of Modified Gravity: Stellar and Gaseous Rotation Curves in Dwarf Galaxies", arXiv:1407.6044 [astro-ph.CO] (2014).

[121] P. Storey and C. Cohen-Tannoudji, "The Feynman Path Integral Approach to Atomic Interferometry", J. Phys. II 4 (1994) 1999-2027.

[122] T. Kovachy *et al.*, "Quantum Superposition at the Half-metre scale", Nature 528 (2015) 530-533.